SYLVESTER SEDEM DJOKOTO

# RESEARCH ON THE APPLICATIONS OF SMART FLUIDS IN MECHATRONIC SYSTEMS

DOCTORAL DISSERTATION

Kaunas
2021

KAUNAS UNIVERSITY OF TECHNOLOGY

SYLVESTER SEDEM DJOKOTO

# RESEARCH ON THE APPLICATIONS OF SMART FLUIDS IN MECHATRONIC SYSTEMS

Doctoral Dissertation
Technological Sciences, Mechanical Engineering (T 009)

2021, Kaunas

This doctoral dissertation was prepared at Kaunas University of Technology, Faculty of Mechanical Engineering and Design, Department of Production Engineering, during the period of 2016–2021.

**Scientific Supervisor**
Prof. Dr. Egidijus DRAGAŠIUS (Technological Sciences, Mechanical Engineering, T 009).

Edited by Brigita Brasienė (Publishing House "Technologija").

**Dissertation Defence Board of Mechanical Engineering Science Field:**
Prof. Dr. Giedrius JANUŠAS (Kaunas University of Technology, Technological Sciences, Mechanical Engineering, T 009) – **chairman**;
Assoc. Prof. Dr. Saulius BASKUTIS (Kaunas University of Technology, Technological Sciences, Mechanical Engineering, T 009);
Prof. Dr. Krzysztof JAMROZIAK (Wroclaw University of Sciences and Technology, Technological Sciences, Mechanical Engineering, T 009);
Prof. Dr. Artūras KILIKEVIČIUS (Vilnius Gediminas Technical University, Technological Sciences, Mechanical Engineering, T 009);
Prof. Dr. Renaldas RAIŠUTIS (Kaunas University of Technology, Technological Sciences, Measurements Engineering, T 010).

The official defence of the dissertation will be held at 2 p.m. on 29 September, 2021 at the Public meeting of Dissertation Defence Board of Mechanical Engineering Science Field in Dissertation Defence Hall at Kaunas University of Technology.

Address: K. Donelaičio St. 73-403, 44249 Kaunas, Lithuania.
Tel. no. (+370) 37 300 042; fax. (+370) 37 324 144; e-mail doktorantura@ktu.lt.

Doctoral dissertation was sent on 29 August, 2021.
The doctoral dissertation is available on the internet http://ktu.edu and at the library of Kaunas University of Technology (K. Donelaičio St. 20, 44239 Kaunas, Lithuania)

KAUNO TECHNOLOGIJOS UNIVERSITETAS

SYLVESTER SEDEM DJOKOTO

# AKTYVIŲ SKYSČIŲ TAIKYMO MECHATRONIKOS SISTEMOSE TYRIMAI

Daktaro disertacija
Technologijos mokslai, mechanikos inžinerija (T 009)

2021, Kaunas

Disertacija rengta 2016–2021 metais Kauno technologijos universiteto Mechanikos inžinerijos ir dizaino fakultete Gamybos inžinerijos katedroje.

**Mokslinis vadovas**
Prof. dr. Egidijus DRAGAŠIUS (Kauno technologijos universitetas, Gamybos inžinerijos katedra – T 009).

Redagavo Brigita Brasienė (leidykla „Technologija“).



Disertacija bus ginama viešame mechanikos inžinerijos mokslo krypties disertacijos gynimo tarybos posėdyje 2021 m. rugsėjo 29 d. 14. val. Kauno technologijos universiteto disertacijų gynimo salėje.

Adresas: K. Donelaičio g. 73-403, 44249 Kaunas, Lietuva.
Tel. (370) 37 300 042; faks. (370) 37 324 144; el. paštas doktorantura@ktu.lt.
Disertacija išsiųsta 2021 m. rugpjūčio 29 d.

Su disertacija galima susipažinti interneto svetainėje http://ktu.edu ir Kauno technologijos universiteto bibliotekoje (K. Donelaičio g. 20, 44239 Kaunas

*''Learning without thought is labour lost; thought without learning is perilous''.*
*Confucius*

**TABLE OF CONTENTS**

## LIST OF TABLES

## LIST OF FIGURES

## LIST OF ANNEXES

## INTRODUCTION

The recent interest in researching various types of high precision actuators and sensors designs used in mechanical and mechatronic systems is overwhelming. The introduction of smart fluids has provided some form of improvement for the functionality of these high precision actuators and sensors. This research is focused on the improvement of the functionalities of three different devices. These improvements are as follows: 1) damper for Cantilever Beam (CB), using the change in the rheological properties of the electrorheological fluid (ERF) as a damping medium; 2) frequency enhancement for Piezoelectric Energy Generator (PEG), using the change in the rheological properties of the magnetorheological fluid (MRF) as a soft impacting medium; 3) spherical braking of a 3D Rotational Piezoelectric Deflector (RPD), using smart fluids as braking media.

In this dissertation, the first application gave an improved way of using ERF as a damping medium for structures. The growing application of medium-sized mechanical and mechatronic structures has ignited a lot of interest among the researchers [1]. Frequently, these structures are subjected to the vibrations; thus, a more robust design is necessary for them to perform under different conditions, such as dynamic loadings. It is well known that vibrations are better controlled through the damping of the system. By applying a low-power control signal, smart fluids can be used to vary the force continuously in order to develop suitable damping [2].

The second application of MRF as a soft impacting medium that was introduced in this dissertation was enhancing the output power of piezoelectric energy generators through a Vibro-impacting method. Piezoelectric energy harvesting is a process where available mechanical energy from the environment is converted into the electrical energy. Piezoelectric materials convert the mechanical vibrational displacement to the electrical voltage and the other way around. Their application is found in a lot of modern wireless telecommunication devices, such as cell phones. Other piezoelectric devices include filters, transducers and oscillators, used in billions of devices for wireless communications, global positioning, navigations and space applications [3]. It has been a challenge to design a system that can harvest the energy and have the ability to perform a task and, at the same time, convert the available ambient energy to power them. Now, autonomous or standalone systems are being used in the areas like medical equipment, mechatronic devices in automobiles, aviation, modern buildings, home entertainment devices and many more. The reduction of pollution from most traditional hydrocarbon powered systems has been a worry for a long time; thus, the introduction and development of autonomous energy harvesters' devices have proven that the issue of pollution can be reduced, and they are cost-effective and robust.

In the third application, smart fluid was introduced as braking for a 3D RPD. The rotational type deflectors, like optical beam deflectors, have many application areas. The examples of the applications of optical beams deflectors are microscopy, optical communication, laser radar systems, target-tracking systems, land survey systems, laser printers, space technologies, medicine, laser machining, metrology, laser scanning and many others [4–8]. The important operation of a rotational optical beam deflector is the directional control of the rotor or actuator for the laser beam communication system to control the swarm of the Pico satellites in the space [9]. A rotational laser optical beam communication device that is used in Pico satellite, for example, has features like flexibility, high positioning accuracy, high resolution and quick response. The growing demand for the miniaturization of satellite systems requires design of small size micro-optical components, which are compact, have low energy consumption, are agile and robust [10]. The 3D RPDs devices transform the multi-directional resonant oscillations of piezoelectric transducers in an accurate continuous or step motion of a micro-mirror or deflector with high accuracy (up to 0.1 μm). One of these miniature types of 3D RPDs was designed at Kaunas University of Technology.

**Aim and objectives of the dissertation**

***The aim*** is to conduct theoretical and experimental studies by applying smart fluids (MRF and ERF) to improve the functionality of Mechatronic systems.

***The objectives to achieve this aim are as follows:***

1. To evaluate the effects of the change of smart fluids and how their application will improve the functionality of devices that are used in mechatronic systems.
2. To perform theoretical and experimental studies using an activated ERF as a damping medium for a vibrating cantilever beam, which are used in resonant sensors and other devices.
3. To design and experimentally investigate the use of MRF as a soft impacting medium for increasing the output power of a bimorph piezoelectric energy generator.
4. To perform theoretical and experimental studies applying the change in the rheological characteristics of ERF and MRF to improve the braking, which affects the precision of angular positioning of 3D Rotational Piezoelectric Deflector.

***Methods and equipment***

This dissertation was based on the theoretical, analytical and experimental research. The theoretical calculations were carried out in MATLAB mathematical analysis software. The FEM analysis was done in COMSOL Multiphysics software.

For the experimental and simulation results of ERF CB damper and the MRF piezoelectric energy generator, the parameters of bimorph piezoelectric cantilever beam were selected.

The experiments were based on a prototype of a 3D Rotational Piezoelectric Deflector that was designed at the Institute of Mechatronics. All experiments presented in this dissertation were conducted at the Institute of Mechatronics, Kaunas University of Technology.

***Scientific novelty***

- **The** control of a vibrating cantilever beam was improved by introducing an activated ERF as a damping medium, localised at the end of the beam.
- A new concept using activated MRF as a soft impacting medium for frequency tuning and power enhancement for a vibrating PEG was researched, and the results show that an increased and stable output power was achieved.
- A new concept of using ERF and MRF as a braking medium in 3D RPD was created, and the results showed a significant improvement in the braking, which affects the precision of the angular positioning.

***Practical value***

The control of a vibrating cantilever beam was investigated by applying activated ERF as a damping medium, localised at the end of the beam.

A new method of using an activated MRF as a soft impacting medium for vibrational frequency tuning and power enhancement of a vibrating Piezoelectric Energy Generator was developed and analysed.

The application of the effects of ERF and MRF as a braking medium on the 3D RPD was developed and analysed. The analytical and experimental study of the braking phenomenon was performed as well.

***Research results provided for the defence***

1. A new method of damping CB with ERF and vibration damping of CB by applying ERF and localising it at the end of the CB was created.
2. A new method of using rheological change in MRF as a soft impacting medium for frequency tuner for PEG was created.
3. A new method for controlling the angular positioning of 3D RPD by applying ERF and MRF as a braking medium was created.

**Outline of the Dissertation**

This dissertation is composed of four chapters. This dissertation contains an introductory chapter that gives a brief introduction on smart fluids (MRF, ERF), piezoelectric material and their behaviour under the influence of various field applications. The research as well presented the application of these smart fluids to improve the functionalities of three novel Mechatronic devices. The introductory chapter as well talked about the previous research findings, leading to the objectives of this study. Each chapter in this dissertation ends with a brief conclusions outlining the achievements and findings that were established in the chapter. The remainder of this dissertation is organized as follows:

***Chapter 2. Vibration Control in Cantilever Beam Structures Using an ERF as Damping Media***. This chapter presents topics related to controlling vibrations in CB, using ERF as a damping medium. It provides a mathematical and experimental evaluation of the system. The results, discussion, conclusions and summary were given at the end of the chapter.

***Chapter 3. Frequency Tuning of a Piezoelectric Energy Generator via the Application of MRF Impacting.*** This chapter introduces a mathematical and an experimental study of the MRF soft impacting form of frequency enhancer for piezoelectric energy generator. The mathematical analysis of the mechanical and electrical characteristics of the bimorph piezoelectric device was presented. This analysis was based on the material properties, geometry and boundary conditions (mechanical and electrical). The results, discussion, conclusions and summary were provided at the end of the chapter.

***Chapter 4. Spherical Brake with Smart Fluid for 3D Rotational Piezoelectric Deflector.*** This chapter introduces a comprehensive experimental study on the effect of smart fluids (MRF and ERF) on the 3-dimensional rotational piezoelectric deflector (3D RPD) as a braking media and an overview of the operational principle of the 3D RPD and discusses how the model describing the operation of the 3D RPD has derived. This theoretical work is a damping medium by the corresponding experimental results. The results, discussion, conclusions and summary were provided at the end of the chapter.

***Chapter 5. Conclusions.*** This chapter summarizes the covered topics and gives conclusions that can be used for the future works related to the application of SF devices.

**ABBREVIATIONS**

**A –** Ampere
**ABS –** Anti-Lock Braking System
**CB –** Cantilever Beam
**DOF –** Degree of Freedom
**DVA –** Dynamic Vibration Absorber
**Dc –** Direct Current
**ERF –** Electrorheological Fluid
**FEM –** Finite Element Method
**FF –** Ferrofluid
**Hz –** Hertz
**3D –** Three Dimensional
**IoT –** Internet of Things
**kPa –** Kilo Pascal
**kV –** Kilovolts
**MRE –** Magnetorheological Elastomers
**MRF –** Magnetorheological Fluid
**Mm –** Millimetres
**MSMA –** Magnetic Shape Memory Alloys
**nm –** Nanometres
**PEG –** Piezoelectric Energy Generator
**PZT–** Lead Zirconate Titanate
**PVDF –** Polyvinylidene Fluoride
**PVEH –** Piezoelectric Vibrating Energy Harvester
**RFID –** Radio Frequency Identification
**RPD –** Rotational Piezoelectric Deflector
**SF –** Smart Fluid
**SM –** Smart Material
**T –** Tesla
**W –** Watt
**µW –** Microwatt
**µm –** Micrometer

## 1. LITERATURE REVIEW

### 1.1. Damping devices

The mechanical structures or devices, such as the resonant sensors, the DVA are used in vehicle engine seats, landing gears and many more [11, 12]. The approach adopted to damping the vibrations in these structures are so-called smart sandwich damping. In the smart structure, the natural frequency and damping property are controlled by the application of external fields such as voltage, current, magnets and electromagnets. The electrorheological fluid (ERF) and magnetorheological fluid (MRF) based sandwich structures have been investigated by [13–17]. Figure 1.1. (a) and (b) shows schematic configurations of two different sandwich structures with ERF and MRF cores [13–17]. Figure 1.2. (a) and (b) shows a schematic of an experimental setup for measuring the dynamic characteristics of the sandwich beam with ERF and MRF, respectively. In the results presented in their research, it was shown that the dynamic characteristics of ERF and MRF based sandwich structures could be tuned. The results show that as the applied field to the ERF and MRF increases, the damping ratio and natural frequencies increase respectively. In another research study, the researchers, using a controlled voltage applied to ERF, localized at different core zones of a sandwiched, which shows that the transient vibration of the system is controlled [18]. The experiments were as well performed using various ERF cores, including corn starch, corn oil and zeolitesilicone oil. In a recent experiment conducted by [19], the results of vibration analysis of ERF composite sandwich beam concluded that the first three modes of natural frequencies and damping factors were increased.

(a) (b)

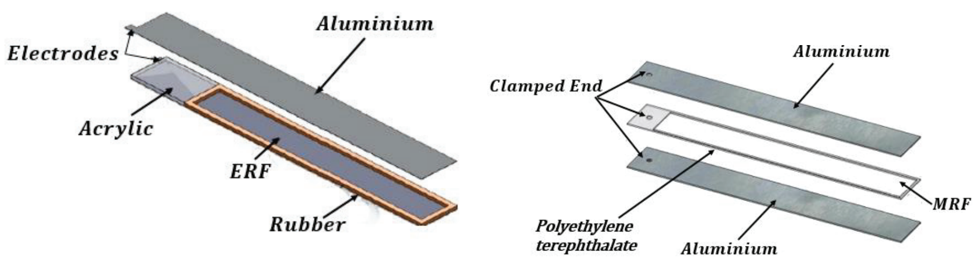


**Figure 1.1.** Diagram and dimension of the sandwich beam with (a) ERF and (b) MRF [13–17]

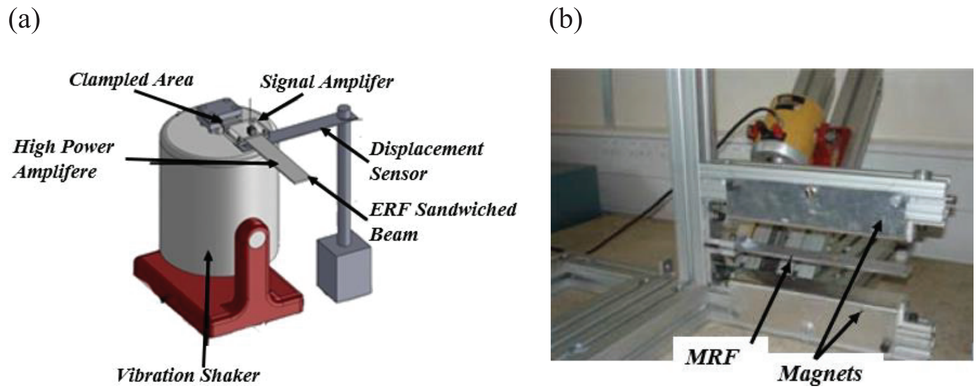


**Figure 1.2.** Schematic diagrams of the experimental setup for measuring the characteristics of (a) ERF and (b) MRF sandwich beam [13–17]

In the study conducted by the researchers, a resonant type sensor employs an element vibrating at resonance. This element changes the output frequency, which is the mechanical resonance frequency. The research further showed that the conversion from the measured to the resonance frequency of the vibrating element is achievable by the change in stress, mass or shape of the resonator. The results show that the resonant type sensor is highly stable, has a high resolution and a quasi-digital output [20]. There are many ways of exciting and detecting techniques that can be used in smart materials, for example, in piezoelectric materials used as sensors, and actuators have a cantilever beam-like structure. These devices are very effective when they are used as measurement and instrumentation devices to measure physical, chemical and biological quantities. They are as well used in structures as structural vibration measurement and control [21–23]. Figure 1.3. and 1.4. show the experimental setup MRF cantilever measurement system in the squeezed and shear mode.

The advantages of using the piezoelectric excitation are strong force, low actuation voltage, high energy efficiency and linear behaviour, high acoustic quality, high speed and high frequency. In the research study, a field-dependent yield stress measuring device where MRF has been subjected to squeeze mode operation was proposed [24]. Their proposed experimental results showed the relationship between the exciting frequency of the resonant structure and the magnetic. Subsequently, the yield stress of MRFs under squeeze mode operation is evaluated as a function of the magnetic flux density using the analytical model. In another approach by [25], the MRF with a resonance concept was proposed to measure the direct current (dc). The system is made of a piezolaminated cantilever beam coupled with an electromagnetic coil-based MRF shear mode set-up. The set-up placed the cantilever beam in resonance at a closed-loop control system. The viscosity, which is part of the rheological property of the MRF, is altered by the current-induced magnetic field produced by the coil. The changes in the MRF produce an additional stiffness to the resonating cantilever beam. Their results showed that the change in resonant frequency as a result of the change in viscosity of the MRF and the frequency shift is related to the input electrical current to the coil. The resonance-based current measurement system is evaluated for the input current range from 0 to 1 A.

(a) (b)

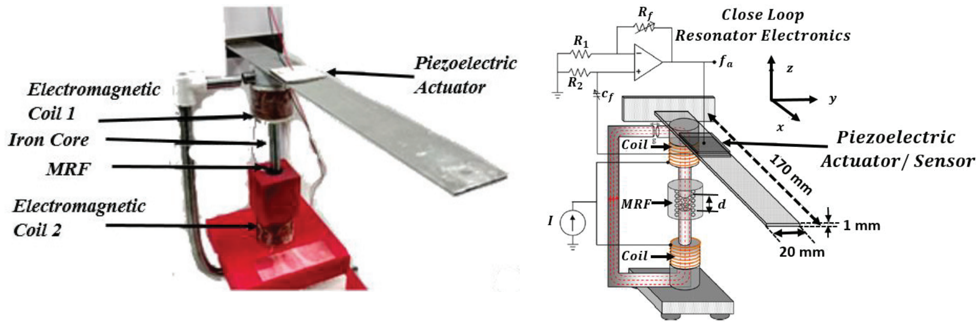


**Figure 1.3.** (a) Photograph and (b) schematic diagram of an experimental setup for squeeze mode yield stress measurement system [23]

(a) (b)

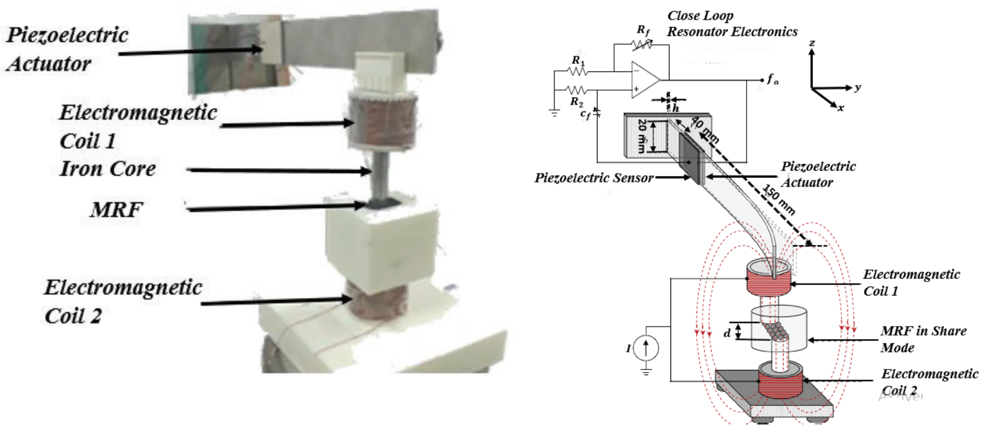


**Figure 1.4.** (a) Photograph and (b) schematic diagram of an experimental setup for share mode yield stress measurement system [23]

In another work conducted by [26], an effective way of changing the vibration characteristics of a cantilever beam using ERF layer was investigated. In their work, the ERF was used as a localized spring damping medium, rather than as a damper. By doing so, the stiffness matrix of the cantilever beam system is changed, and consequently, the resonant frequencies could be significantly changed. Their experimental approach had a layer of ERF of 1 (mm) in thickness that was applied only to a small part of a cantilever beam of about 150 mm long. The ERF serves as a complex spring used to link the beam to the ground. An electric field strength ranging from 0 to 5 (kV/mm) was applied to the ERF layer. The results achieved in the experiment demonstrated a non-linear frequency response function curve, and the resonant frequencies of the cantilever beam changed significantly under different electric field configurations.

This non-linear vibration characteristic is closely associated with the presence of the yield stress, which imposes damping of both frictional and viscous nature, as well as an additional stiffness onto the beam. This experiment was conducted based on the findings by [27].

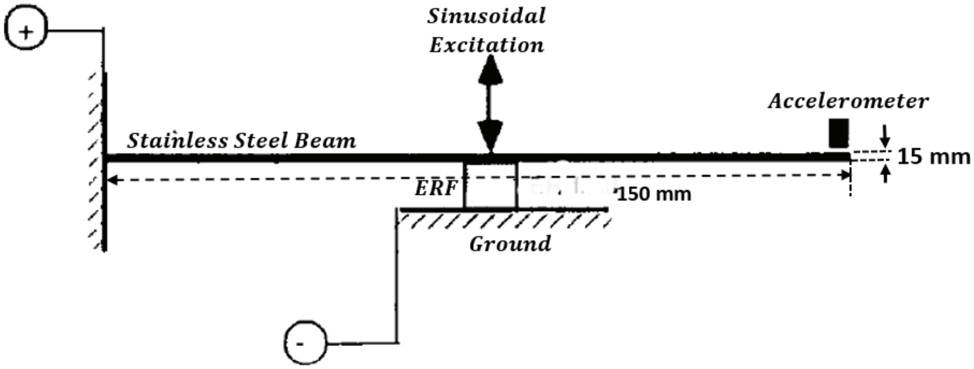


**Figure 1.5.** Test rig configuration of a cantilever beam with a layer of ERF applied at the mid-section of the beam [27]

Figure 1.5. shows a sinusoidal excitation force generated by a vibrator applied to a cantilever beam where the output signal was detected by the accelerometer at the free end of the beam. The findings from their experiment established that the effect of constrained ERF viscoelastic layer treatment on the loss factor and the resonant frequency is very limited. One of the deficiencies of the sandwiched cantilever beam is that the external and shear moduli of the activated ERF under electric field application is not high enough to dissipate energy. As a result, the amplitudes of vibrating sandwich cantilever beam are very small. Nevertheless, when a good and workable approach is adopted, rather than the ERF serving as a damper, it is rather used to change the structural configuration of the original vibration system or change the stiffness matrix of the beam system. By doing so, a more significant effect in changing the vibration characteristics could be obtained.

### 1.2. Vibro impact base power enhancement system for PEG

The increase in low power, wireless devices and sensors call for a sustainable green energy generating system to replace the traditional battery energy source. It is for that reason that piezoelectric transducers with the low power generation capability are used for these devices that require low amounts of power output [28, 29]. The low power generation capability of the piezoelectric transducers can be attributed to many factors, like including material properties, cantilever beam shapes, structural parameters and many more. Another important problem with the piezoelectric energy harvesters is usability in the produced output power, because the vibration in the built environment is randomly distributed with varying frequencies. One of the methods, which researchers are using to address these limitations, is to come with a way to widen the operating bandwidth of the piezoelectric energy harvesters. The examples of this method include, among others, using an array of linear generators, each with a different resonant frequency [30], broadband or multimodal energy harvesters [31–33].

The researchers are designing and experimenting with frequency-up-conversion techniques that convert the low-frequency vibrations to high-frequency vibrations as one of the ways to deal with the problem associated with piezoelectric energy harvesters. The results from these experiments have demonstrated that the efficiency of the harvester and broadens of its operational bandwidth has increased. One of the well-known earlier methods of Vibro-impacting techniques was a proposed piezoelectric generator that converts the impact of a steel ball bouncing on a piezoelectric membrane into the electrical energy [34]. Other impact-based frequency up-conversion techniques have been reported in [35, 36]; it is an energy harvesting floor tile based on the frequency up-conversion principle for converting low-frequency vibration, especially pedestrian's step, into usable electrical energy. The concept is shown in Figure 1.6. In this concept, twenty-four unimorph piezoelectric cantilever beams were fixed on a stand with their free ends. A stainless-steel mass was attached to the free ends of the cantilever beam. The attached mass increases the strain in the piezoelectric material, thus increasing the electrical output power. The permanent magnets are glued on to the surface of the attached mass. The magnets attract an iron bar under the cover plate when the floor tiles are stepped on. In order to prevent the piezoelectric layer of the cantilever beam from damaging during the displacement, a soft plastic bar was used as a stopper to absorb the impact force.

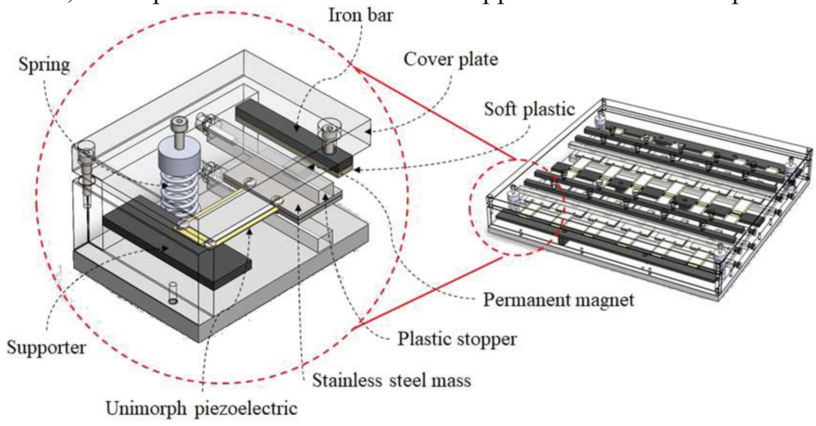


**Figure 1.6.** Schematic drawing of a Vibro-impact energy harvester using floor-tiles [37]

Another solution to the low frequency was proposed by [38], as shown in Figure 1.7., where the system was made up of a cantilever beam with a mass with two permanent magnets placed above and below the free end of the cantilever beam. The mass provided an additional stiffness to the cantilever beam. The magnets on the top provided an attractive force, whilst the magnets on the bottom provided a repulsive force. The upward movement of the cantilever beam creates an attractive force between the magnets. The attractive force created a change in the stiffness of the cantilever beam, thereby changing the resonance frequency. The device was able to achieve 10 Hz bandwidth from 22–32 Hz. The range of the harvested power was between 240–280 μW

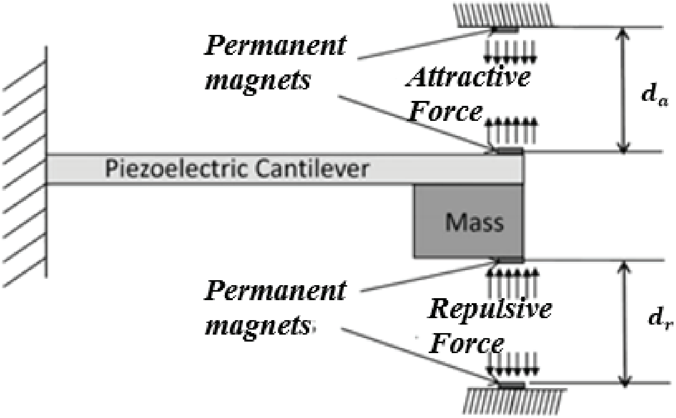


**Figure 1.7.** Magnet tuning harvester [38]

There was a proposal to increase the dynamical efficiency of a cantilever beam vibrating in the third mode as shown in Figure 1.8. [39]. This is one of the methods for producing this mode of stimulation, i.e., Vibro-impact or forced excitation. In their research, the peculiarities of the cantilever beam vibrating in the third mode are related to the significant increase of the level of deformations. This deformation was able to extract significant amounts of energy, compared to the conventional harvester vibrating in the first mode, which has been widely researched. Two types of PVEH were analysed, i.e., the first one without electrode segmentation and the other segmented, using electrode segmentation at the strain nodes of the third vibration mode to achieve effective operation at the third resonant frequency. By exciting the segmented PVEH in the third mode resonant frequency, the voltage generated by any segment gives 3.4–4.8 fold increase compared to the non-segmented PVEH. The efficiency of the energy harvester that has been presented gave an increase at lower resonant frequencies from 16 % to 90 %.

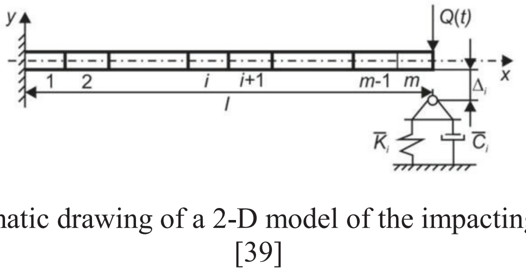


**Figure 1.8.** Schematic drawing of a 2-D model of the impacting cantilever beam [39]

Figure 1.8. is a schematic drawing 2-D model of impacting cantilever beam, where Q(t) is the load that acts in the system. $K_i$ and $C_i$ are stiffness and viscous damping coefficients of the damping medium; $\Delta_i$ is the size of the gap between the i-th nodal point of the structure and the surface of the damping medium that is located at the ith nodal point.

### 1.3. Rotational type piezoelectric deflector

The main driving element of machines, such as motors and actuators, are producing one degree-of-freedom (DOF) rotary or linear motion. The modern rotary machines possess more complex structures and sophisticated motions to achieve tasks that have never been automated before they had been developed, for example, humanoid robots, surgical robots, electric vehicles and many more. Therefore, it is necessary that the compact design of the machinery, actuators that can produce multiple degrees of freedom motion in one integrated package without the intermediate transmission mechanisms would become crucial. The spherical motion system has a compact multi-DOF rigid body motion along a spherical surface with a permanent centre of rotation. Therefore, it is not surprising that spherical motion is becoming the most important motion type next to the compact rotary motion. The examples of the spherical motions found in the humans and other mammals are the eyeball movements, human wrist, shoulder and hip joint motions. Surveillance devices, automation tools, automobiles and home appliances are other areas where spherical motion is present. The existing spherical motion generation devices are frequently designed by combining two to three rotary actuators with serially or parallel connected mechanisms. Such devices are inevitably bulky and difficult to deploy as a critical component in complex machinery. Therefore, the need to develop a multiple DOF actuator capable of generating spherical motion arises [40].

The accuracy of steering the laser beam depends on the characteristics of the rotation of the rotor of the 3D RPD. These characteristics are as follows: the rotational speed, spatial resolution, maximum rotation angle, stabilization and number of degrees of freedom [41–45]. When designing the 3D RPD, the two operational principles were considered, i.e., electro-mechanical and piezoelectric. The unique feature of the design of the 3D RPD is the use of piezoelectric transducers. The industrial laser optical systems use electrical motors to rotate or move the mirrors; the accuracy of positioning the laser beam is limited to several micrometres [46].

Another area where the rotational type actuator is applied is haptic devices. Robotic surgery is notable among the haptic applications. The modern surgery devices, which are robot-assisted, provides minimally invasive surgery by the introduction of a haptic master device, which function is not to generate the motion for a slave robot as well as to reflect the surgeon's physical constraints [47, 48]. A telerobotic surgical system, where the surgeon sits at a workstation and controls the robot, has been introduced. The haptic devices normally require an actuating component for tactile feedback. Currently, they are designed with a motor-driven actuator. Like 3D RPD, most haptic feedback is carried in the form of vibration based on the eccentric motors, which have some disadvantages, such as complex mechanisms. The bottleneck in such systems is another area that has been addressed in this research work. The introduction of smart fluids (ERF and MRF) has been discussed by many researchers. The phenomenological behaviour of these smart fluids, such as resistance to external forces or pressures, high stability (smooth motion) and reliable control performance, helped in the development of MRF and ERF spherical rotor braking system [49, 50]. In the SF spherical braking system, the transmission elements add to the overall spherical rotor size, and the unwanted effects, such as backlash, deflection or slippage, are taken care of. The use of SF in spherical rotors has compact yet high torque spherical SF brakes. SF brakes are already used in many devices, such as exercise equipment or automobile clutches brakes and drives by wire systems, Orthopaedic Knee Brace and many more [51–54].

(a) (b)

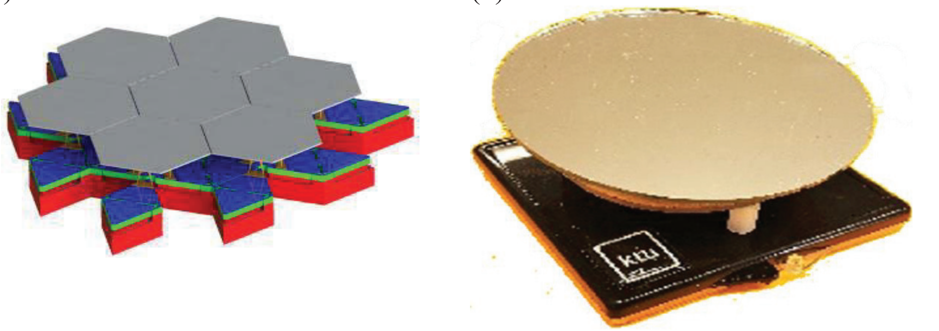

**Figure 1.9.** (a) Tip-tilt-piston micro-mirror design with single fabricated mirror [55] and (b) the view of experimental deflector [56]

(a) (b)

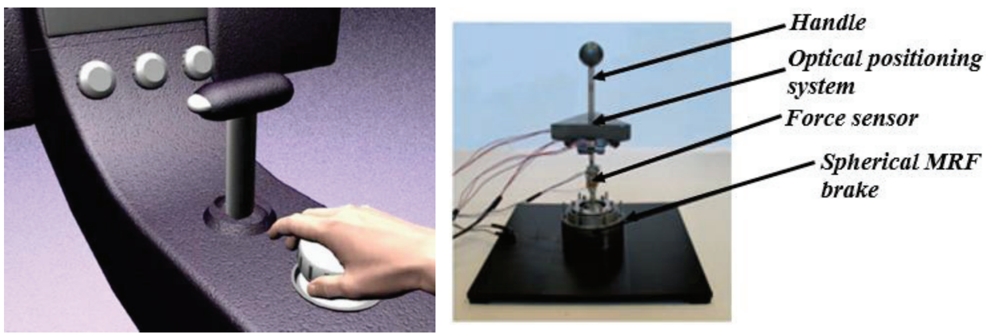


**Figure 1.10.** (a) Photograph and (b) experimental representation of the prototype multi-function haptic knob for vehicular [57]

A typical example [55] is shown in Figure 1.9. (a), where Tip-tilt-piston mirror design with a single fabricated mirror and (b) a prototype of the 3D RPD were developed at the Institute of Mechatronics, Kaunas University of Technology. Figure 1.10. (a) is an illustration of a multi-function haptic knob for vehicles, and (b) is the experimental representation of the prototype of a multi-function haptic knob for vehicles

## 1.4. Smart materials

The use of materials in engineering applications, for example, the mechanical and civil engineering applications, dates back to the stone, bronze and iron ages. The development of structures in modern engineering applications, such as mechatronics engineering, telecommunication engineering, automation engineering, computer engineering etc., call for the development of more improved and specialised materials for these sophisticated devices.

**Table 1.1.** Classification of some smart materials and their responses

| **Stimulus** | **Material Classification** | **Response** |
|---|---|---|
| Magnetic field | Magnetorheological fluids [60, 61] | Change in Rheological Properties |
| | Magnetorheological elastomers [62, 63] | Change in Rheological Properties |
| | Ferrofluids [64] | Change in Rheological Properties |
| | Magnetostrictive materials [65] | Change in Mechanical Strain |
| | Magnetic shape memory alloys [66] | Change in Mechanical Strain |
| Electric field | Electrorheological fluids [67, 68] | Change in Rheological Properties |
| | Electroluminescent materials [69] | Light Emission |
| | Electrochromic materials [70] | Colour Change |
| | Electrostrictors [71] | Change in Mechanical Strain |
| Electric field/pH | Electroactive polymers [72] | Change in Mechanical Strain |
| Electric current | Piezoelectrics [73, 74] | Change in Mechanical Strain |
| Temperature | Shape memory Alloys [75, 76] | Change in Mechanical Strain |
| | Pyroelectrics [77] | Electric Polarization |

The materials that have been discovered and developed in the past decades are smart or intelligent materials. SMs are materials that have multiple properties, such as electrical, magnetic, chemical, mechanical and thermal. They convert energy, such as photovoltaic, thermoelectric, piezoelectric, photoluminescent and electrostrictive, and some are energised by altering or tuning external fields [58]. In general, smart materials can be divided into many categories based on their stimulus and response as shown in Table 1.1. Classification of some smart materials and their response. [59]

### 1.4.1. Smart fluids

Smart fluids are defined as field responsive fluids, either magnetic or electric fields, which are a part of a group of relatives known as smart, rheological or actively controllable fluids. These fluids were first experimented with and applied by Jacob Rabinow at the US National Bureau of Standard in 1948 [78]. Smart Fluids consist of permeable micron-sized polarizable particles dispersed throughout the carrier medium, which is non-conducting fluid-like silicon oil. The composition of SFs is made up of a broader diversity concerning solvent, solute and additives [78, 79].

Magnetorheological fluids are SFs that can attain a yield stresses of over 80 kPa; hence, they have remarkable range of fluid dynamical capabilities and controllability. MRFs are characterized by the magnetorheological effect. They have stable fluid behaviour, and they are durable as well. Therefore, they were the first SFs that have commercial implementation. Much research has been done to improve the performance of this fluid. There has been written well-documented literature works that are related to the behaviour and performance of MRF in some specific MR fluid devices [80].

### 1.4.2. Properties of smart fluids

In general, the reactions of SFs are similar. The only difference is that, for example, MRFs have magnetic saturation, while ERF is limited by dielectric strength [81]. The application of the electric field makes the particles inside the ERF polarized and have higher dielectric constant than its surrounding carrier fluids. The number of polarised particles by the movement of charges in fluid when the field concentration is increased [67]. These particle chains restrict the movement of the fluid. However, MRFs are far more stable, have low power consumption and higher yield stress. [82]. MRFs have less active fluid requirement to execute their mechanical performance compared to the ERFs. An additional advantage of MRF over ERF is that ERF is very sensitive to the influence of contaminants or impurities, while MRFs are not [83]. ERFs need high voltage for it to operate; hence, they are not able to cope with contaminations. One thing that makes ERFs to stand out is their distinctive feature that they show higher response characteristics as compared to MRFs [84].

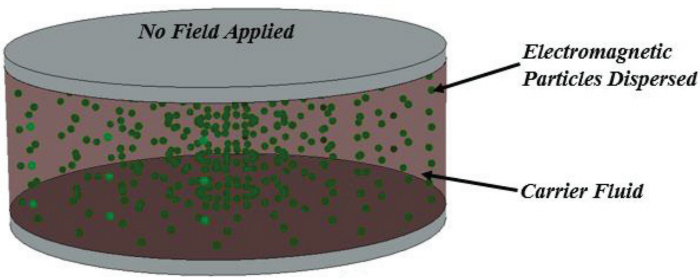


**Figure 1.11.** Characterising SF without applying external field

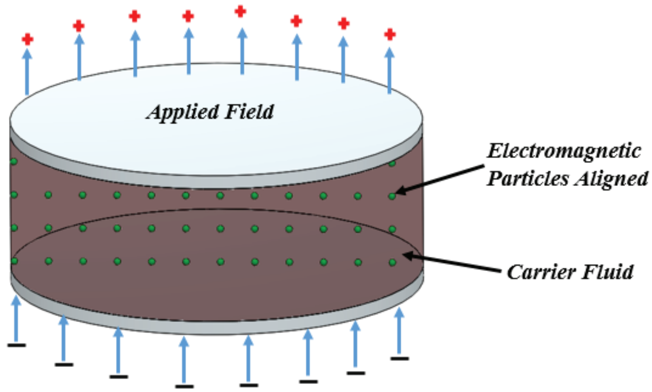


**Figure 1.12.** Characterising SF by applying external field

Figure 1.11. shows the Bingham plastic fluid flow behaviour of SF where the particles are spread within the SF without an electric/magnetic field. When the appropriate field is applied, the particles are aligned into chains as shown in Figure 1.12.

**Table 1.2.** Properties of some smart fluids (MRF, ERF and FF)

| **Properties** | **ERF [88, 89]** | **MRF [80, 90]** | **FF [85, 91]** |
|---|---|---|---|
| Response time | Few Milliseconds (ms) | Few Milliseconds (ms) | Few Milliseconds (ms) |
| Viscosity ($\text{Ps.a}^{-1}$ at 25 °C) | 0.1–0.3 | 0.1–0.3 | 0.002–0.05 |
| Particulate material | Polymers, Zeolites, etc. | Ferromagnetic, ferrimagnetic, etc. | Magnetite, hematite, etc. |
| Particle size | 0.1–10 $\mu m$ | 0.1–10 $\mu m$ | < 10 $nm$ |
| Carrier fluid | Oils, dielectric gel and many other | Water, synthetic oils, non-polar and polar liquids | Aqueous paramagnetic salt solution |
| Density | 1–2 $g/cm^3$ | 3–4 $g/cm^3$ | 1–2 $g/cm^3$ |
| Required field | $\sim 4\, kV/mm$ | $\sim 250\, kA/m$ | $\sim 20\, kA/m$ |
| Power supply | $\sim 2-5\, kV$ | $\sim 2-25\, V$ | $\sim 2-5\, kV$ |
| Yield strength | $\sim 2-10 kPa$ | $\sim 50-100 kPa$ | 0 |
| Temperature | $10\ to\ 90$ °C (ionic DC)<br>$-25\ to 125$ °C (non-ionic DC) | $-10\ to\ 150$ °C | $10\ to\ 60$ °C |
| Field excitation | Electric Field | Electromagnetic/ Magnetic Field | Magnetic Field |

The field responsiveness of FFs is different from ERF but similar to MRF. Like ERF and MRF, FF is made up of a colloidal suspension of mono-domain ultrafine magnetic particles, which is normally less than 10 nm, dispersed in either aqueous or non-aqueous liquids. The application of the external magnetic field causes the dipolar interactions within the particles to be induced; thus, these particles become aligned in the field direction. Even though there is a similarity in the field response to MRF, FFs do not show yield stress; they have field dependent viscosity. In contrast, MRF has larger particles and react differently as compared to Ferrofluids under the same influence of the magnetic field. MRFs can change their viscosity with the formation of a chain structure and solidify when a magnetic field is applied. However, Ferrofluids commonly keep their viscosity with high magnetic fields [85−87]. Table 1.2. shows typical properties of ERF, MRF and FF.

### 1.4.3. Phenomenological modelling of smart fluids

The application of SFs in mechatronic devices demands an appropriate control system. Therefore, the modelling to predict the non-linear behaviour of the fluid will form an integral part of designing the SF devices. Numerous phenomenological models have been introduced to characterise the behaviour of SFs devices.

MRFs are applied in devices for torque transfer, such as brakes and clutches. The Lord Corporation has commercialized MRF exercise and gym equipment [92–96]. Another main application area for controllable fluids is in dampers and mounts for use in semi-active or adaptive vibration control and snubbing. Some automotive companies are applying this technology in automobiles, such as the primary suspension [97, 98], secondary suspensions [99–101], engine mounts [102] and vehicle seat vibration control. Figure 1.13. shows a schematic diagram of a typical MRF fluid damper. In the field of Civil Engineering, MRF dampers are used for seismic damping as vibration control [103, 104]. In aviation, it is used as helicopter rotor damping augmentation and landing gears [105].

The MRF and ERF dampers, clutch and braking systems for automobile, aviation and civil engineering works have been improved and commercialised [106-108]. The yield stress that is generated under the external electrical field strengths application to ERF and its ability to have a reversible continuous control and fast response makes it a good media for vibration control, tactile display, sensor and other applications for different modes. Other application areas of ERFs include torsional vibration clutch, brake, damper, optical material polishing, tactile devices and many more. In the research conducted by [109], using the controllable characteristics of ERF as power transfer medium for functions in a special object in an automobile clutch was examined. Another research conducted by [110] investigated how to control braking force distribution in the vehicle's ABS. ERFs have low yield stress; hence, they are enable to be used in hydraulic actuators. The development of the so-called giant ERF, however, has improved fluid's yield stress up to 130 $kPa$ that has made it possible to use in hydraulic actuators [111]. Optical lenses have been fabricated in ERF solutions as well as polishing the tactile material for the optical devices [112]. Other recent applications of ERF are a force display device using 1-DOF ERF brakes and 4-DOF haptic devices using ERF for minimally invasive surgery [113–115].

However, Ferro Fluids have their applications sealing devices, energy transportation, dampers, sensors etc. Even though SFs have exhibited a promising controllable capability, there has not been enough research on the varying field strengths application, which is needed for a good control strategy. Most researches and applications are focused on only one field application.

Ferro Fluids are being widely applied in devices based on the significant progress in both theoretical and technical. One area where these FFs are being applied is the energy and mechanical engineering sector [116, 117]. The researchers are using FF in combination of polymerised materials to develop multiple kinds of composite materials, such as polymer-like architectures, magnetically responsive photonic crystals and microrobots [118, 119]. It has been discovered that FFs has been used in biomedical engineering to facilitate the diagnosis and therapy of diseases, such as cancer, angiocardiopathy and rheumatoid arthritis [120–123].

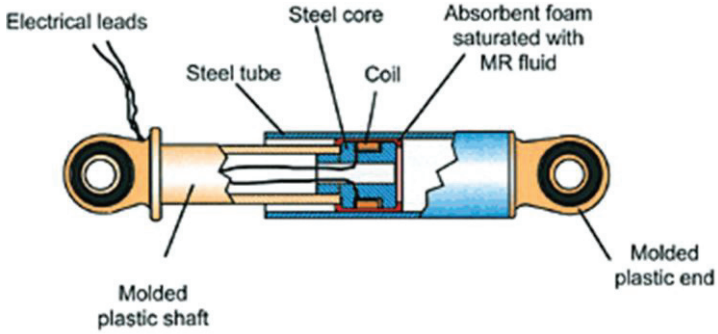


**Figure 1.13.** MRF Damper [103, 104]

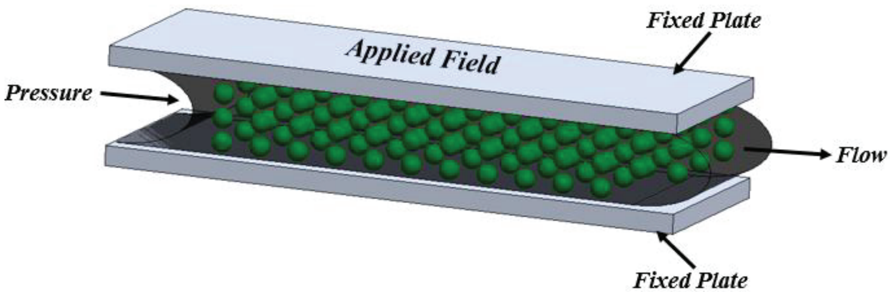


**Figure 1.14.** Basic operating mode of SF in flow mode

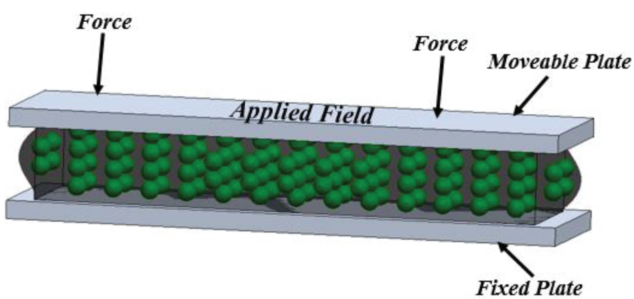


**Figure 1.15.** Basic operating mode of SF in squeeze mode

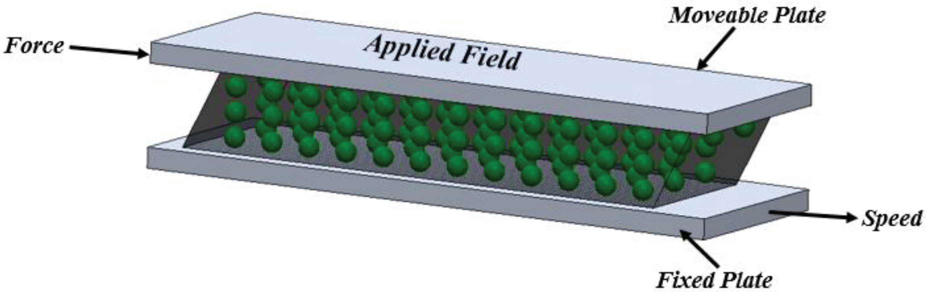


**Figure 1.16.** Basic operating mode of SF in shear mode

The modes of operations of SFs applied in engineering and other devices are the valve (flow) mode, the direct shear mode or a combination of the two modes and the squeezed mode [124]. In the valve mode shown in Figure 1.14., the SF is constrained between two stationary objects, which could be electrode plates or discs in the case of ERF. When a subsequent field is applied to the SF in this mode, the particles within the fluid (magnetic or electromagnetic) are aligned parallel to the field lines up towards the charges of the applied field. In the direct shear mode, the fluid is subjected to direct shear between two plates, translating or rotating, thus 'shearing' the fluid between perpendiculars to the applied field as shown in Figure 1.15. When the field is increases, the shearing resistance of the fluid increases as well. The squeeze operating mode involves one plate moving in the direction of the applied field as in Figure 1.16. The field strength in the squeeze mode changes according to the distance between the plates, as the field is applied, thus the upward and downward movements of the plates [125].

### 1.4.4. Bingham model

The Bingham plastic model is the most commonly used model to describe the behaviour of SFs. SFs behave like a Newtonian fluid, where the relationship between the shear stress and shear strain rate of the fluid is linear. The ideal Bingham theory defines the behaviour of the SFs as a solid, until the yield stress $\tau_y$ is exceeded and then exhibits a linear relationship between the stress and the rate of shear or deformation. However, the yield stress is a function of an applied field. As the applied field increases, the yield stress increases as well. Figure 1.16. (a) shows the characteristic behaviour of SF without applied field, and (b) shows the change in shear stress and apparent viscosity by changing the applied field. Therefore, the shear stress in SFs is as follows:

$$\tau = \tau_y \, sgn(\dot{\gamma}) + \eta\dot{\gamma}; \tag{1.1}$$

where $\dot{\gamma}$ is the yielding shear stress controlled by the applied field, $\eta$ is the plastic viscosity of the fluid, thus the Newtonian state without an applied field [85].

(a) (b)

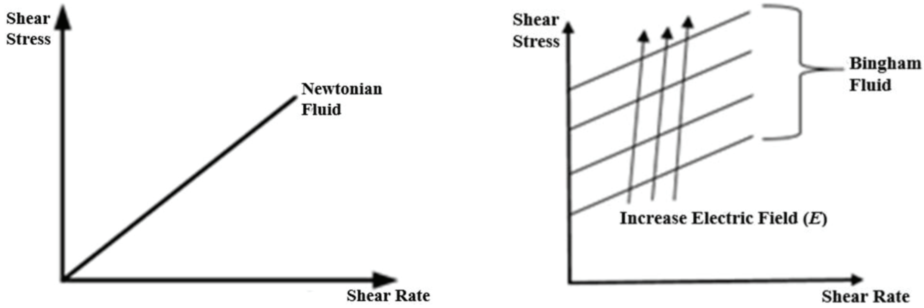


**Figure 1.17.** (a) Characteristic behaviour of SF without applied electric field, (b) the change in shear stress and shear strain of MRF under different magnetic field strengths [85]

The Bingham damping model mechanism of SFs systems consists of a Coulomb friction element placed in parallel with a viscous damper as shown in Figure 1.18. The model shown in the diagram has a force $F$, which is generated by the SF device, and is calculated as:

$$F = f_c\, sgn(\dot{x}) + C_0\dot{x}; \tag{1.2}$$

where $\dot{x}$ is the velocity due to the external excitation, $C_0$ is the damping coefficient, and $f_c$ is the frictional force. These are all related to the viscosity of the SF and the field-dependent yield stress [126].

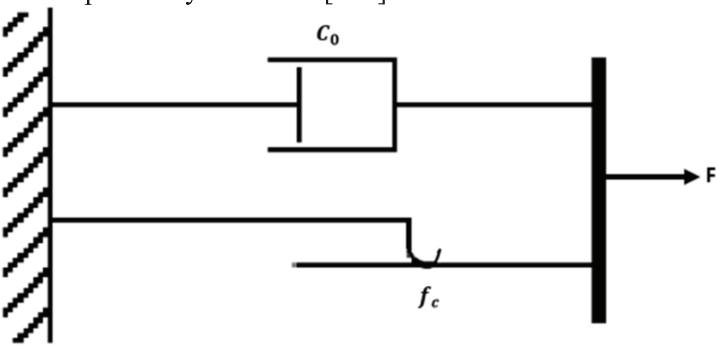


**Figure 1.18.** Bingham model [126]

As stated earlier, the Bingham model accounts for the behaviour of the fluid beyond the yield point. Nevertheless, there is the assumption that the Bingham model does describe fluid's elastic properties at small deformations and low share rates. However, this is necessary for dynamic applications [127]. Figure 1.19. shows a comparison between the predicted force-velocity characteristics and the result of the experiments conducted by [128].

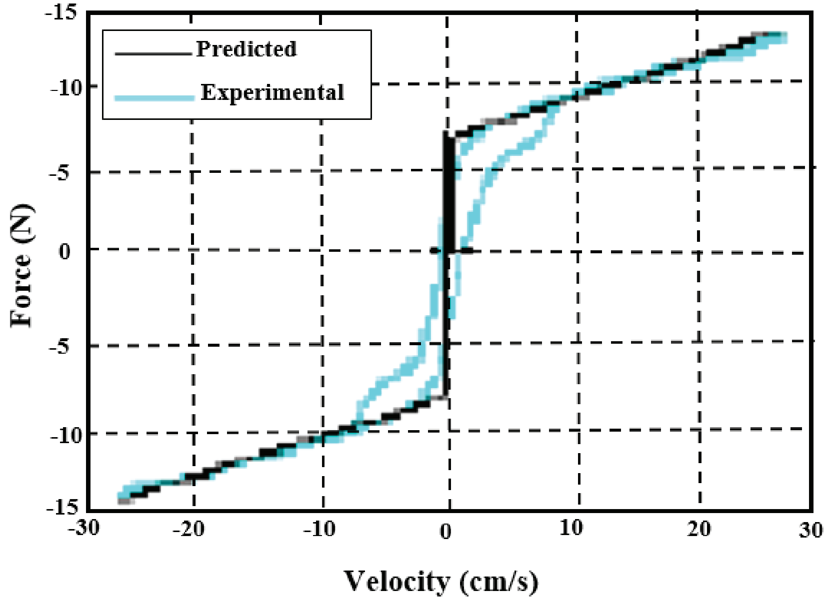


**Figure 1.19.** Comparison of predicted and experimental force-velocity characteristics of Bingham Model [129]

### 1.4.5. Extended Bingham model

The research presenting the extended Bingham model that shows the behaviour of the SF in the pre-yield, post-yield region and the post-yield point was conducted by [130]. Figure 1.20. shows the viscoelastic-plastic model, which is made up of the Bingham model in series with the three-parameter element of a linear solid (Zener element). Therefore, the force in this system is calculated as follows:

$$F = \begin{cases} C_0\dot{x}_1 + f_c\, sgn\,(\dot{x}_1) \\ k_1(x_2 - x_1) + C_1(\dot{x}_2 - \dot{x}_1) & |F| > f_c, \\ k_2(x_3 - x_2) & |F| \leq f_c, \\ k_1(x_2 - x_1) + C_1\dot{x}_2 \\ k_2(x_3 - x_2) \end{cases} \tag{1.3}$$

where $C_0$ is the damping coefficient and the frictional force; $f_c$ accounts for the plastic viscosity and the yield stress. The field-dependent parameters $C_1$ , $k_1$ and $k_2$ are the fluid's elastic properties in the pre-yield region as shown in Figure 1.19. [131].

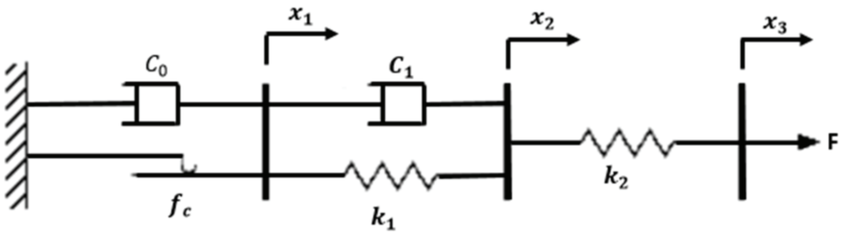


**Figure 1.20.** Extended Bingham model [132]

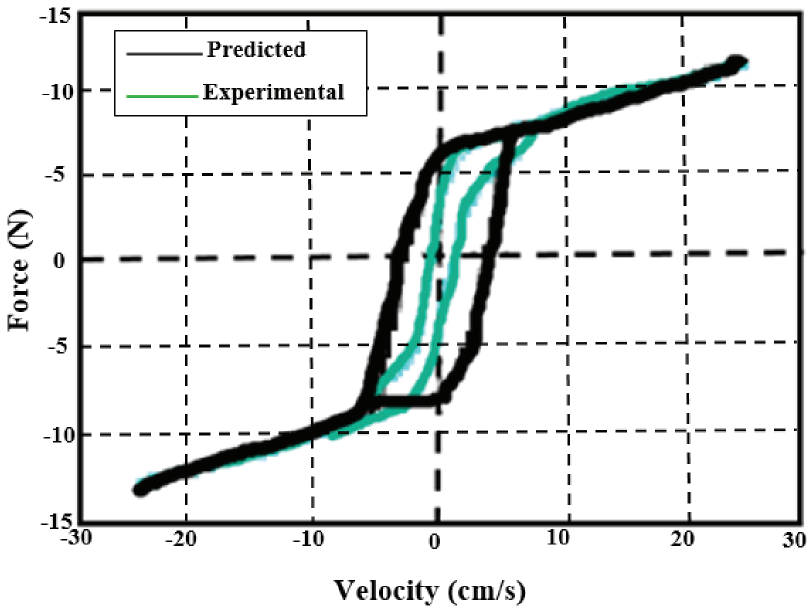


**Figure 1.21.** Comparison of predicted and experimental force-velocity characteristics of Bingham Model [129]

Figure 1.20. shows the hysteretic response of the MRF device using the extended Bingham model. In the research, developing the system, it has been found that deriving a mathematical model using an ordinary differential equation was almost impossible due to the non-linear Coulomb frictional element.

### 1.4.6. BingMax model

In the BingMax model, a discrete element model of similar components is proposed by [133]. This model is made of a Maxwell element in parallel with a Coulomb friction element as depicted in Figure 1.22.

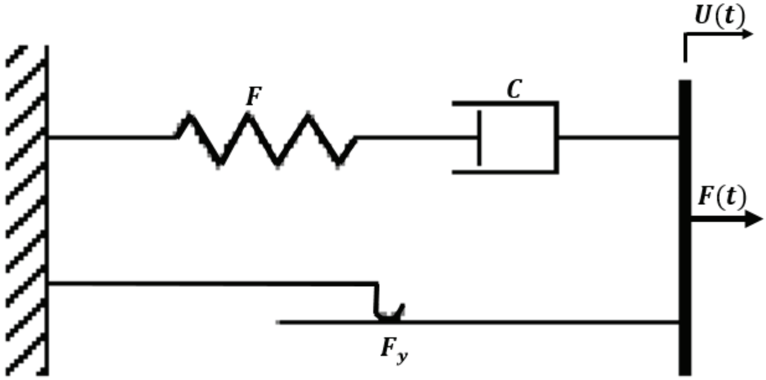


**Figure 1.22.** BingMax model [134]

The force $F(t)$ in the model is given as follows:

$$F(t) = K\int_0^t exp\left(-\frac{t-\tau}{\lambda}\right)\dot{u}(\tau)d\tau + Fy \cdot sgn[\dot{u}(t)]; \quad (1.4)$$

where $\lambda$ is the damping constant $C$ and the spring stiffness $K$, $\lambda = C/K$. $Fy$ is the permanent friction force. The equation (1.4) can be written as follows:

$$F(t) = \lambda\frac{dF(t)}{dt} = C\dot{u}(t) + Fy \cdot sgn[\dot{u}(t)]. \quad (1.5)$$

### 1.4.7. Bouc-Wen model

The phenomenological Bouc-Wen model is normally modelled to characterise the behaviour of SFs dampers; most representation of these SFs dampers is the MRF damper shown in Figure 1.23. The system is made up of a spring element, a linear damping element and a normalized Bouc-Wen element as seen in Figure 1.23. [135]. The phenomenological Bouc-Wen model equation for MRF damper as is provided below:

$$F = C_0\dot{x} + k_0(x - x_0) + \alpha z; \quad (1.6)$$

where $\omega$ is the hysteretical component, thus:

$$\dot{z} = -\gamma|\dot{x}|z|z^{n-1} - \beta\dot{x}|z|^n + \delta\dot{z}. \quad (1.7)$$

In order to control the shape of the force-velocity characteristics of the system, the parameters $\alpha$, $\beta$, $\gamma$, $\delta$ and $n$ could be tuned accordingly. $x_0$ is the initial displacement of the spring that is incorporated into the model to make room for the accumulator for the damping system.

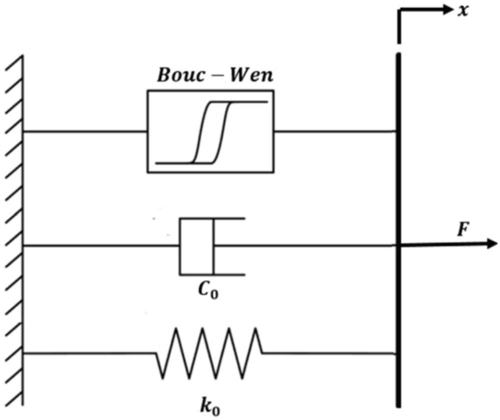


**Figure 1.23.** Simple Bouc-Wen model [136]

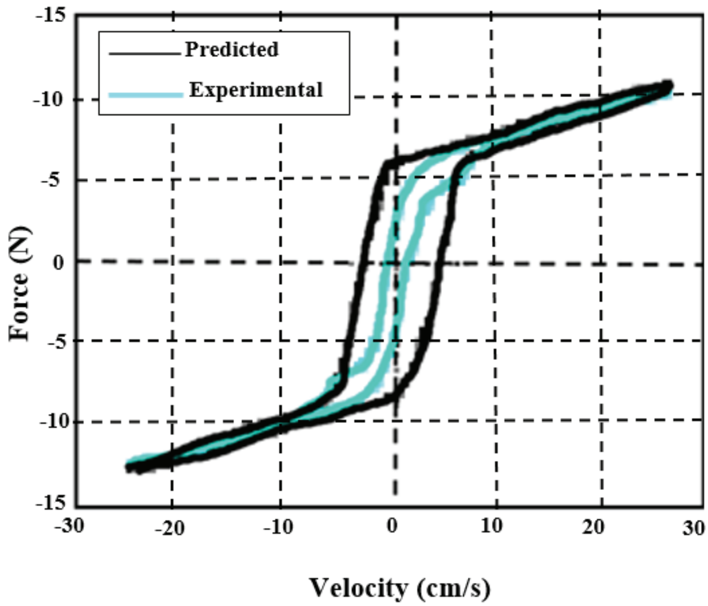


**Figure 1.24.** Comparison of predicted and experimental force-velocity characteristics of Bouc-Wen model [136]

Unlike the extended Bingham model, the Bouc-Wen model is more suitable for numerical simulations, because it is less stiff. Figure 1.24. shows the comparison between the predicted and the experimental force-velocity characteristics of the Bouc-Wen model [137]. However, the velocities with a small absolute value and an operational sign opposite to the sign of the acceleration can be observed from Fig.1.24.

### 1.4.8. Modified Bouc-Wen model

The response of the MRF damper in the region of the yield point [138] proposed an extension of the Bouc-Wen model, which is depicted in Figure 1.25. The equations for the force in this system are given below:

$$F = \alpha z + C_0(\dot{x} - \dot{y}) + k_0(x - y) + k_1(x - x_0) \qquad (1.8)$$
$$= C_1\dot{y} + k_1(x - x_0);$$

where

$$\dot{z} = -\gamma|\dot{x} - \dot{y}|z|z^{n-1} - \beta(\dot{x} - \dot{y})|z|^n + \delta(\dot{x} - \dot{y}) \qquad (1.9)$$

and

$$\dot{y} = \frac{1}{C_0 - C_1}[\alpha z + C_0\dot{x} + k_0(x - y)], \qquad (1.10)$$

$$\alpha = \alpha(u) = \alpha_a + \alpha_b u. \qquad (1.11)$$

$z$ is the hysteretic component; $k_1$ and $x_0$ are the spring constant and the initial displacement.

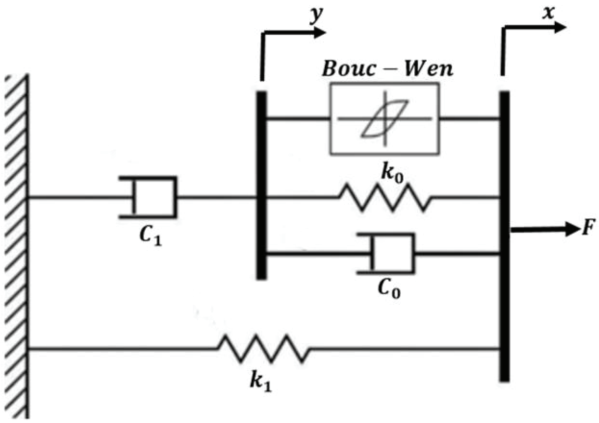


**Figure 1.25.** Modified Bouc-Wen Model [140]

$C_0$and $C_1$ is the function of the damper input current given in equations (1.12) and (1.13).

$$C_1 = C_1(u) = C_{1_a} + C_{1_b}u, \qquad (1.12)$$

$$C_0 = C_0(u) = C_{0_a} + C_{0_b}u, \qquad (1.13)$$

$$\dot{u} = -\eta(u - v), \qquad (1.14)$$

where $v$ is the input voltage.

The modified Bouc-Wen model and experimental results are given by [141] and are shown in Figure 1.26. The figure shows the comparison between the force-velocity characteristics that were predicted by the modified Bouc-Wen model and the experimental results conducted by [141].

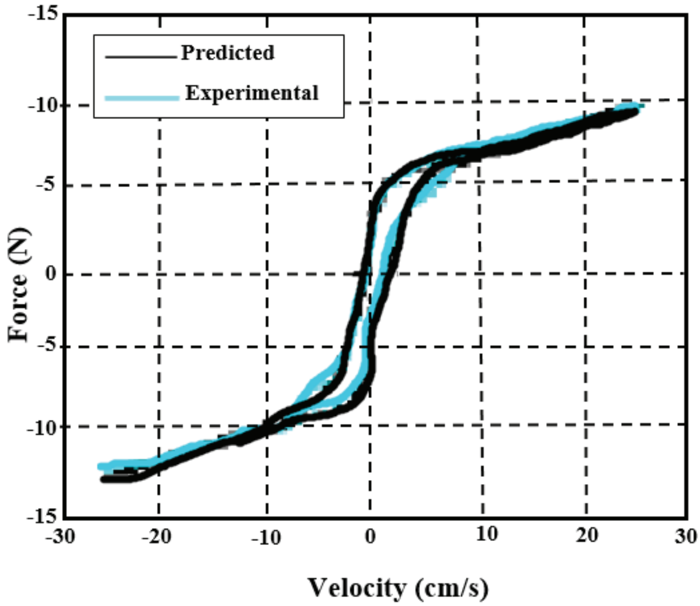


**Figure 1.26.** Comparison of predicted and experimental force-velocity characteristics of Modified Bouc-Wen model [142]

The model was able to reproduce the MRF behaviour accurately, even over a broad range of operating conditions [141]. It has been discovered that the independent parameter values of the applied voltage should not be calculated again when the applied field strength changes. The model that was proposed there is dependent on the design and the components of the specific MRF device. Particularly, the additional spring was introduced to account for the accumulator that is present in the considered damper.

### 1.4.9. Non-linear viscoelastic-plastic model

Another type of a phenomenological model for the SFs in the viscoelastic-plastic model [143] is a combination of two linear shear flow mechanisms with non-linear weighting functions to characterise the response of the SFs device.

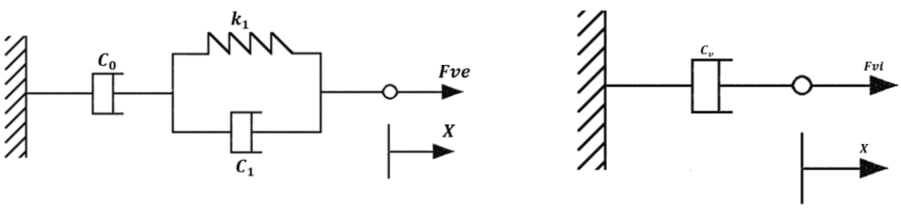


**Figure 1.27.** Inertial mechanism of the augmented viscoelastic-plastic model [144]

As it can be seen from Figure 1.287., the pre-yield region of the fluid's behaviour is simulated by the three-parameter element of a linear fluid (Jereys model). The viscoelastic force $Fve$ is generated by this system that is governed by:

$$Fve + \frac{C_0+C_1}{k_1} \cdot \frac{dFve}{dt} = C_1\dot{X} + \frac{C_0C_1}{k_1}\ddot{X}; \tag{1.15}$$

where $C_0$, $C_1$ and $k_1$ are the parametric damping and spring stiffness constants, respectively. $X$ is the displacement transmitted to the device. In the post-yield region, the SFs response is given by the vicious relationship as in [145]:

$$Fvi = C_v\dot{X}; \tag{1.16}$$

where $C_v$ is the damping coefficient, which is related to the viscosity of the fluid as shown in Figure 1.27. The change from the pre-yield to the post-yield phase is performed by nonlinearly combining the viscoelastic and viscous components $Fve$ and $Fvi$ to the net force as provided below:

$$F = FveSve + FviSvi. \tag{1.17}$$

The shape functions are as follows:

$$Sve = \frac{1}{2}\left[1 - \tanh\left(\frac{\alpha-\alpha_y}{4\varepsilon_y}\right)\right], \tag{1.18}$$

$$Svi = \frac{1}{2}\left[1 - \tanh\left(\frac{\alpha-\alpha_y}{4\varepsilon_y}\right)\right]. \tag{1.19}$$

This force depends on the velocity $\alpha$ non-dimensionalised concerning its amplitude; the yield parameter $\alpha_y$ is correlated with the fluid's yield point and a smoothing parameter $\varepsilon_y$ [145]. A scheme of the force-displacement relationship is shown in Figure 1.28.; $Lve$ and $Lvi$ are the linear operators, representing the equations 1.18 and 1.19.

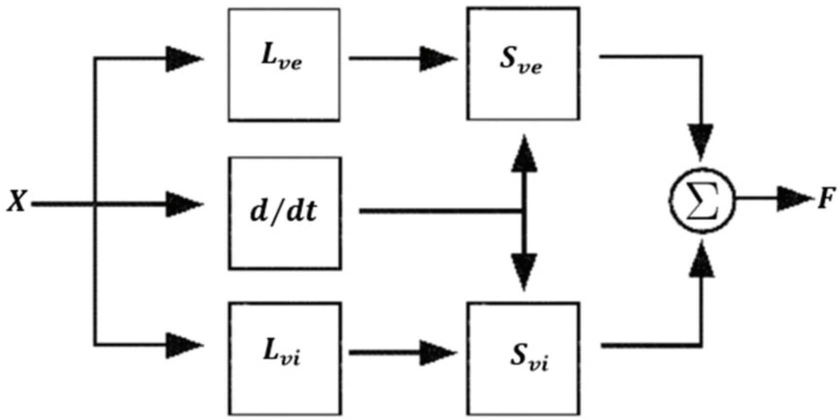


**Figure 1.28.** Scheme of the viscoelastic-plastic model [145]

The parametric constant has derived to be strong functions of the applied field. The coefficients associated with the viscoelastic and plastic properties were approximated as a polynomial function of the field strength. The predicted data compared to the experimental data showed that the model could reproduce the nonlinear effects of the SF behaviour qualitatively. The model is numerically robust due to the linearity of the parallel shear flow mechanisms [145].

### 1.4.10. Augmented non-linear viscoelastic-plastic model

The extended non-linear model was proposed by [146] to reproduce the force-velocity characteristics of the considered SF device by [147]. In the model proposed, the pre-yield region has a friction force $Fc$ that weights due to the addition of the shape function $Sc$ to allow for Coulomb-like stiction effects that were observed at low velocities. The force $F_{by}$ that is generated in the pre-yield region is provided below:

$$F_{by} = F_{ve} + S_c F_c, \tag{1.20}$$

where

$$S_c = \frac{1}{2}\tanh\left(\frac{\dot{X}}{4\varepsilon_c}\right) \tag{1.21}$$

and $\varepsilon_c$ is a smoothing factor. $Fve$ is the viscoelastic component given in equation 1.15.

The viscous and initial mechanism shown in Figure 1.29. is used to take care of the effect of the fluid inertia effect beyond the yield point [148]. The $F_{ay}$ in the post-yield region given as follows:

$$F_{ay} = C_v\dot{X} + R\ddot{X}. \tag{1.22}$$

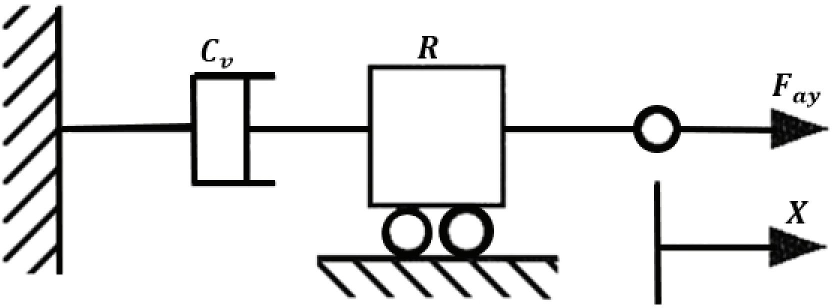


**Figure 1.29.** Inertial mechanism of the augmented viscoelastic-plastic model [149]

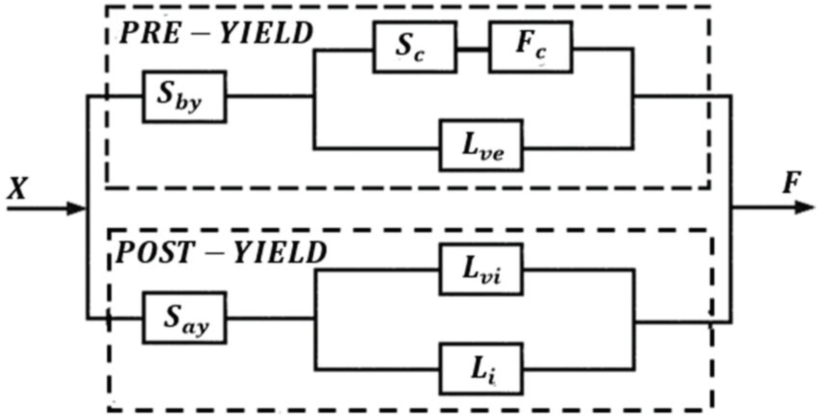


**Figure 1.30.** Scheme of the augmented viscoelastic-plastic model [149]

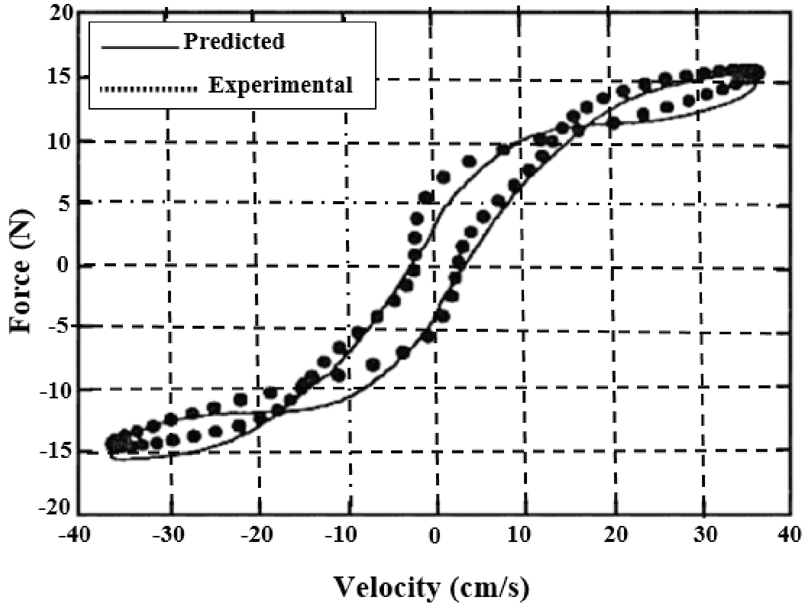


**Figure 1.31.** Comparison of predicted and experimentally obtained force-velocity characteristics of the augmented viscoelastic-plastic model [151]

The combining the shear flow mechanisms of the two non-linear weighting functions $Sby = Sve$ in (Eq. 1.18) and $Say = Svi$ (Eq. 1.19) yielded a nonlinear network, which is shown in Figure 1.30. The total force $F$ generated by this augmented viscoelastic-plastic model is given as follows:

$$F = S_{by}F_{by} + S_{ay}F_{ay}. \tag{1.23}$$

Figure 1.31. shows a comparison between the force-velocity characteristics predicted by the proposed model and obtained from the experimental results. The model precisely showed the behaviour of the considered SF device at different field

strengths and displacement amplitudes [150]. $F_c$ is an added friction component to the system, which largely depends on the design of the considered damper, but they can be adjusted by choosing suitable parameter values. Moreover, the non-linear combination of linear flow mechanisms is numerically tractable.

### 1.4.11. Other models

The analytical model for SFs devices that operate in the squeeze-flow mode is governed by the shear stress in the Bingham plastic model and can be generalised to the bi-viscous relationship as given below:

$$\tau = \begin{cases} \eta_r \dot{\gamma} & |\tau| < \tau_1 \\ \tau_0 + \eta \dot{\gamma} & |\tau| > \tau_1 \end{cases}; \tag{1.24}$$

where $\dot{\gamma}$ is the strain rate, and $\eta_r$ and $\eta$ is related to the elastic and the viscous fluid properties [152]. The yield parameters $\tau_0$ and $\tau_1$ satisfy the equation:

$$\tau_0 = \tau_1 \left(1 - \frac{\eta}{\eta_r}\right). \tag{1.25}$$

The yield parameter is shown in Figure 1.32. In order to obtain the Bingham plastic model, $\eta_r \rightarrow \infty$.

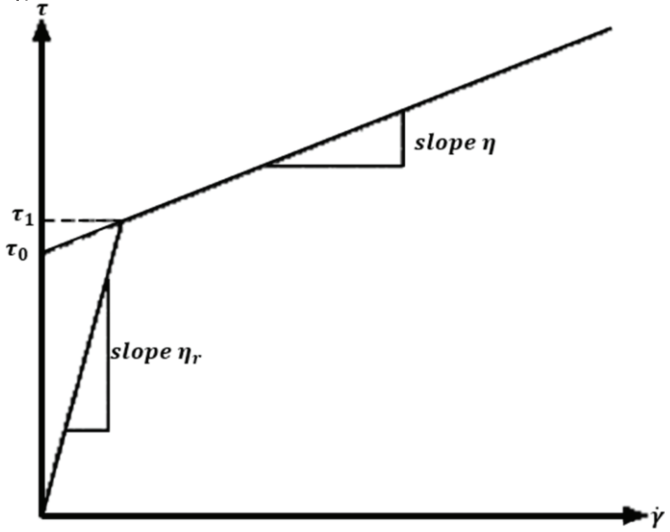


**Figure 1.32.** Bi-viscous model [153]

The study of continuum mechanics constitutive model to characterise the behaviour of an ERF prototype damper, where the fluid's motion in the valve of the damper has been approximated by Hagen-Poiseuille flow theory, has been investigated by [153]. In this theory, the flow is assumed to laminar a one-dimensional flow through a stationary annular duct. The first-order differential equation with variable coefficient to account for the elastic-viscoplastic properties of the fluid is given as follows:

$$\frac{d\tau}{dt} + \frac{G\dot{\gamma}}{\eta_0\dot{\gamma}+\tau_y sgn(\dot{\gamma})} \cdot \tau = G\dot{\gamma}; \tag{1.26}$$

where $\eta_0$, $\tau_y$ and $G$ are the plastic viscosity, the yield stress and the elastic shear modulus of the fluid, respectively.

### 1.4.12. Piezoelectric devices

Piezoelectric devices can be defined as devices that apply piezoelectric materials to convert mechanical deformation into electrical charge or vice versa. These devices are classified into three main categories: sensors, actuators and harvesters [154]. The piezoelectric material undergoes deformation where mechanical energy is transformed into the electrical energy, which is known as the direct piezoelectric effect as demonstrated in Figure 1.33.

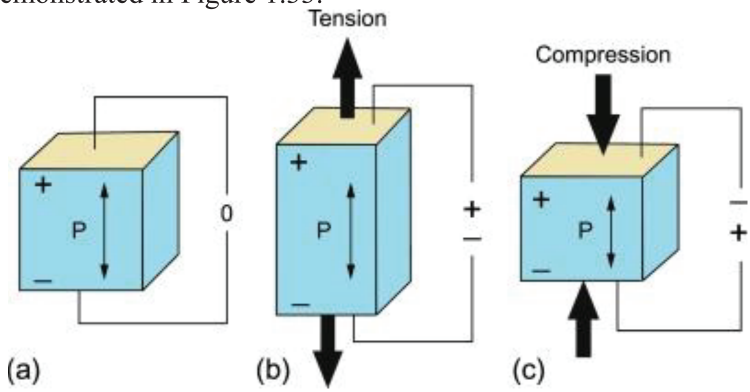


**Figure 1.33.** Schematic of direct piezoelectric effect: (a) piezoelectric material, electrical charge generation under (b) tension and (c) compression [155]

Piezoelectric materials either can be natural materials or manufactured materials that display the piezoelectric effect. Some examples of natural materials are tourmaline and quartz crystals. The manufactured material are ceramics or polymers, for example, PZT or PVDF. The linear constitutive equations of piezoelectric materials are expressed as [157].

### 1.4.13. Applications of direct piezoelectric effect

One of the applications of direct piezoelectric effect is the sensor. Piezoelectric sensors can detect changes in pressure, acceleration, force, etc. The piezoelectric sensor works by the application of the strain to the sensing component. When there are any changes in the stress, it results in a polarization change from the rearrangement of the dipole moment. This causes a measurable difference in the electrical potential across the device, thus making piezoelectric sensitive to very small changes. While the following examples are not comprehensive of all possible sensor applications, they highlight several common uses as well as some interesting technologies of the future.

Piezoelectric sensors are used in automobiles to improve the drivability and safety of the vehicle. Most of the piezoelectric sensors are made of PZT. The examples of piezoelectric sensors are knock sensors, tire pressure monitors, airbag and seatbelt sensors, gyroscopes, accelerometers and engine fluid detection [158].

The medical industry is another area where piezoelectric materials have been applied to the modern medical devices. The ultrasound device is one of the examples of medical devices that is made of piezoelectric material. The ultrasound device uses the direct piezoelectric effect to detect a reflected sound that is displayed as an image for the analysis. Other medical devices that apply piezoelectric materials are sensors in electronic stethoscopes, hearing aids, flow meters to monitor vascular health and both external and internal sensors for health status monitoring.

As the world is moving gradually away from the integrated digital and physical technology and then turning towards the Internet of Things (IoT), the demands for piezoelectric materials and devices are becoming increasingly important. An IoT "smart" device uses a sensor to collect data, stored, processed, and shared intelligently, usually through a wireless communication network, useful information about the state of the environment of interest [159]. In addition, for all sensor applications in the IoT, the work must be done to reduce the cost of sensors, lower their power consumption and discover new materials that can handle exposure to the harsh environments [160, 161].

Another area where the piezoelectric material application is popular is piezoelectric motors. Piezoelectric motors can generate unlimited rotary or linear movements of up to 100 μm and can offer high precision positioning on the nanometre scale. Piezoelectric motors are divided into three categories based on the different drive and functional properties for producing unlimited rotatory or linear movement: [162] resonance drive or ultrasonic motors, [163] inertia-drives and stepping piezo actuators [164]. This technology plays an important role in the world of robotics, such as motors on micro scale using MEMs (micro electrical–mechanical systems) that can generate power from the flying or walking motion of bug-like robots [165–169]. Another important application area is piezo-damping. Piezo-damping effect is a process where the external energy from the noise is transformed into the electrical energy through the heat dissipation. The actuator, a piezoceramic, is used for the active vibration dampening, while the sensor, a piezopolymer, is used to measure the vibrations of the structure. Then, the resultant vibration measurement controls the voltage applied to the actuator to minimize the unwanted vibrations [170, 171].

The direct piezoelectric effect is used in energy harvesting technology via repetitive mechanical vibrational movements. The mechanical vibrations, which are normally wasted energy, are converted to the electrical energy through a piezoelectric device. One area from where that wasted energy can be harvested is the repetitive motions of the body; thus, the energy is available from different motions of the human body throughout the day. An interesting area of human motion where energy is harnessed is human footsteps. Piezoelectric tiles are placed on the dance floors [172] and train station floors [173], where the output energy is stored in a battery and used to power some of the lightings at each facility. Though the power produced by a step is ~0.1 W; nevertheless, when used in high traffic areas, they can make a significant impact. Piezoelectric energy harvesting is now playing a critical role in the Internet of

Things, as every sensor will need a power source. The unlimited supply of power from piezoelectric energy harvesters could allow the sensor to function continuously for duration of its life.

In most energy harvesting technologies, a cantilever beam is used. These cantilever beams are usually made up of one or two layers of piezoelectric material and another layer of another material used only to reinforce the cantilever beam structure. A cantilever beam with a single piezoelectric layer is called a unimorph; with two piezoelectric layers, it is called a bimorph, see Annexe 1. In a normal setup for the energy harvester, the cantilever beam is mounted on a vibrating body where the dynamic strain is induced into the piezoelectric layer (layers) due to the cantilever beam deflection. Thus, by doing so, an alternating voltage is generated across the electrodes that are attached to the surface of the piezoelectric layer (layers).

### 1.4.14. Limitations of piezoelectric energy harvester

There are some limiting factors of using piezoelectric harvesters to generate the amount of power needed for powering electronic and other devices. The major challenge that is associated with piezoelectric energy harvesters is that they operate effectively at only single excitation frequency. This means that the excitation frequency matches the optimal frequency of the piezoelectric harvester, which defines the frequency at which the harvester generates the maximum voltage. In most cases, the vibrating body has a range of acceleration amplitudes and frequencies. An example is, for a desirable design of a harvester, to generate power from human movement; the characteristics of change in movement from time to time, according to the current activity (walking, running, sleeping, etc.), should be considered. Therefore, it is desirable to design a piezoelectric harvester with a tuneable optimal frequency or one that can operate effectively across a certain range of excitation frequencies.

### 1.4.15. Modelling of the piezoelectric device

The demand of piezoelectric elements for powering electronic circuits in different applications has increased. Due to this, there is a need for models that can predict the generated voltage across any circuit connected via the piezoelectric device electrodes. Piezoelectric device design and modelling require several steps of the design process. Firstly, the concept of modelling and system design should not be complex. Secondly, the parameters for design should be considered. During the design phase, equivalent circuit models are usually implemented in the early design phases of the piezoelectric system. At the design phase, the parameters, which enter into the models, are obtained by various methods. Among these methods, the ‘experimental’ parameter identification is based on the systems’ transfer functions. It can be applied whenever a physical prototype is available [174–178].

In Figure 1.34., the standard piezoelectric material is represented by the axes system. The axes system is represented by axes 1, 2 and 3 that correspond to Cartesian Coordinates X, Y and Z axes. The axes 4, 5 and 6 represent the rotational axes (U, V, W) or shear of each one of these axes, respectively. The direction of positive polarization is usually made to coincide with the 3-axis, and the electrodes are usually attached perpendicularly to this axis, as shown in Figure 1.34.

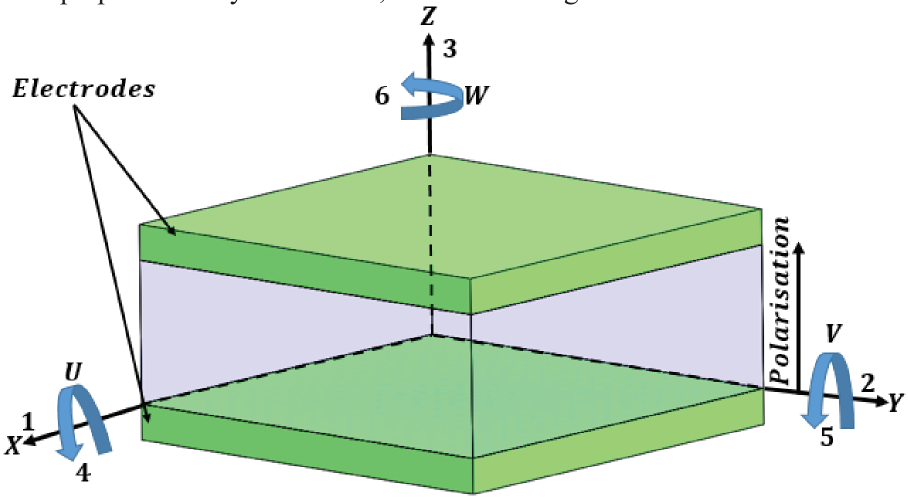


**Figure 1.34.** Piezoelectric materials axes system

According to [179], the linear constitutive equations for piezoelectric materials are given as follows:

$$\binom{S}{D} = \begin{pmatrix} s^E & d \\ d_t & \varepsilon^T \end{pmatrix} \binom{T}{E}; \tag{1.27}$$

where $S$ is the mechanical strain, $T$ is the mechanical stress, $D$ is the dielectric charge displacement, and $E$ is the electrical field strength. $s^E$ is the compliance tensor under the condition of a constant electric field, which is defined as strain generated per unit stress; $d$ tensor contains a piezoelectric charge constant, giving the relationship between electric charge and mechanical stress. $T$ is the absolute permittivity, which is defined as the dielectric displacement per unit electric field for constant stress. For most applications, there exists a dominant deformation mode, and these equations can be reduced to scalar form. For example, if the piezoelectric material is polarized in 3-direction; then, the electrical field is applied in the same direction, while the predominant mechanical stress and strain are in the 1-direction. Piezoelectric energy harvesters are usually designed to operate in 33-mode or 31-mode [180].

$$S_1 = S_{11}^E T_1 + d_{31} E_3, \tag{1.28}$$

$$D_3 = d_{31} T_1 + \varepsilon_{33}^T E_3. \tag{1.29}$$

The equation 1.28 can be transformed into a form where the mechanical strain and the dielectric charge displacement are considered as independent variables. Then, this becomes:

$$\binom{T}{E} = \begin{pmatrix} c^D & h \\ h_t & \beta^s \end{pmatrix} \binom{S}{D}. \tag{1.30}$$

The equations 1.28 and 1.29 can be rewritten as:

$$T_1 = \frac{1}{S_{11}^E(1-k_{31}^2)} S_1 - \frac{1}{d_{31}} \left(\frac{k_{31}^2}{1-k_{31}^2}\right) D_3, \tag{1.31}$$

$$E_3 = -\frac{1}{d_{31}} \left(\frac{k_{31}^2}{1-k_{31}^2}\right) S_1 + \frac{1}{\varepsilon_{33}^T(1-k_{31}^2)} D_3. \tag{1.32}$$

The piezoelectric coupling factor is given as:

$$k_{31}^2 = \frac{d_{31}^2}{\varepsilon_{33}^T S_{11}^E}. \tag{1.33}$$

The discretization of a model with distributed parameters leads to a lumped-parameter model. In many research works, the lumped-parameters model is mostly used for the piezoelectric harvesters [181–186]. Piezoelectric models are as well described by using circuit theory, applying electromechanical analogies for a better electric technological understanding [187]. The equivalent lumped model of the system is made up of the equivalent mass, mechanical damping, mechanical stiffness, capacitance and the conversion factor between the mechanical and electrical domains [188–192]. However, the damping and stiffness are assumed linear in most systems. These assumptions can cause inaccuracy in the obtained results, for example, if the amplitude of the excitation acceleration is large.

The equivalent electrical system of the piezoelectric device is normally represented in the circuit diagram shown in Figure 1.35. This system is based on direct analogies between the mechanical and electrical variables: the generated or applied voltage is analogous to the applied force in the equivalent mechanical system, and the electric charge is analogous to the mechanical displacement in the mechanical system. Similarly, the applied force in mechanical systems is analogous to the voltage source in the equivalent electrical system, and the displacement of the mass is analogous to the electrical charge in the electrical equivalent system [193, 194].

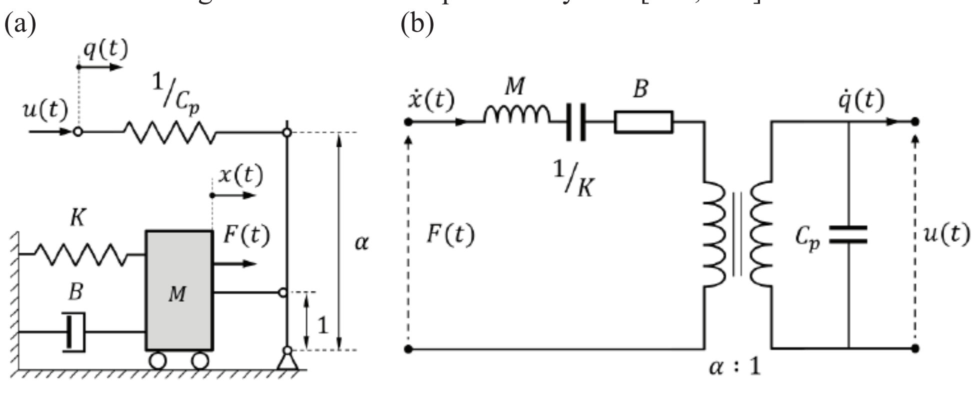


**Figure 1.35.** Equivalent systems of piezoelectric devices in (a) mechanical and (b) electrical representations [195]

The system shown in figure above is based on the direct analogies between the mechanical and electrical variables. There, $u(t)$ is the applied voltage, which is analogous to the applied force in the equivalent mechanical system; $q(t)$ is the electric charge, which is analogous to the mechanical displacement in the equivalent mechanical system. $F(t)$ is the applied force in mechanical systems that is analogous to the voltage source in the equivalent electrical system, and $x(t)$ is the displacement of the mass that is analogous to the electrical charge in the electrical equivalent system.

### 1.5. Conclusions

This chapter gave a literature review of devices that used smart fluids to improve their functionalities. The devices presented in the literature review are similar to the devices presented in this dissertation.

The damping devices are using smart fluids as damping media. In most of this research work, the SF is usually embedded into a cantilever beam. Some structures have the fluid localised at the end of the vibrating cantilever beam. The disadvantage of these SF sandwich beams is activating the fluids; hence, the full damping effects are not achieved.

Frequency up-conversion is another technique that has gained wide recognition in the energy harvesting research community. This is a process of using an impacting base and magnetic coupling method to transfer a Low-Frequency Resonator to a high-frequency Piezoelectric Vibration Energy Harvester. The results from this technique have proven that stable power output is achievable with the impact-based frequency enhancer method.

Spherical motion is a compact multi-DOF rigid body motion along a spherical surface with a permanent centre of rotation. Other systems with spherical motions, which are not mechanical, are found in humans and mammals, such as the eyeball movements, human wrist, shoulder and hip joint motions. The known spherical motion devices are frequently designed by combining two to three rotary actuators with serially or parallel connected mechanisms. Due to the weight of these spherical actuators, the precise positioning is difficult to achieve. Smart materials and their working process and application have been reviewed as well. These fluids are MRF, ERF and FF. The modes of operations of SFs that are applied in engineering and other devices are the valve (flow) mode, the direct shear mode or a combination of the two modes and the squeezed mode.

A mathematical model that describes the properties of SF and devices needed to be understood and researched to predict their behaviour for numerical simulation is a part of the phenomenological modelling of SFs. In order to achieve optimal control of the SF devices, the dynamic behaviour of the mechanical system when SF is applied should be taken into account as well. The examples of such systems are active suspension dampers that use the change in rheological properties to control the dynamic behaviours such as damping road disturbances of vehicles to provide maximum comfort for the driver and the passengers.

# 2. VIBRATION CONTROL IN CANTILEVER BEAM STRUCTURES USING AN ERF AS DAMPING MEDIUM

## 2.1. Introduction

The novel actuator using ERF as a damping medium was proposed in this research work. The key enabling concept of the proposed actuator is to enhance the force due to the electric field produced by the applied voltage using the ERF. The direction and amount of voltage input to the bottom electrode, deciding on the characteristics, such as contraction, extension and the force generated by the actuator, respectively. The cantilever beam vibrates at its resonant frequency using the piezoelectric actuation technique. In order to obtain the required displacement and actuation force, the viscosity of the ERF between the bottom electrode and the vibrating cantilever beam is precisely varied by the input voltage. In this work, the ERF is operated in one of the most powerful modes, called squeeze mode; hence, the designed ERF damping medium actuator is more powerful and precise.

The theoretical frequency response functions have derived for a flexible piezoelectric cantilever beam that is excited with external forcing. A finite element model of the structure is developed in COMSOl multiphysics software, where a direct integration algorithm is used to simulate the frequency response of the proposed cantilever beam with localized ERF. The experiments investigate the transient response of a piezoelectric cantilever beam with an ERF. The results demonstrated that the ERF layer can be used for suppressing the vibrations and reducing the settling time of the beam. The experimental results were used to validate the used theoretical approach over these four field conditions[5].

## 2.2. Design and modelling of ERF-CB

The proposed structure of the Cantilever Beam (CB) with an ERF active damping medium is shown in Figure 2.1. The system is made of a vibrating CB with its tip influencing ERF. The layer of ERF ($F_t$) 0.7 mm was placed on a rectangular fluid holder with an electrode bottom plate. The fluid layer $F_t$ was chosen as a result of the miniature nature of the device. The ERF solidifies when it is subjected to the electric field, serving as an active damper for the vibrating CB.

---

[5] *This section contains information from the article of the author with the details below: IEEE Sensors Journal, vol. 20, Issue. 8, pp. 4072–4079. doi:10.1109/jsen.2019.2961380 2019. Controlling of Vibrations in Micro-Cantilever Beam Using a Layer of Active Electrorheological Fluid Damping Medium.*

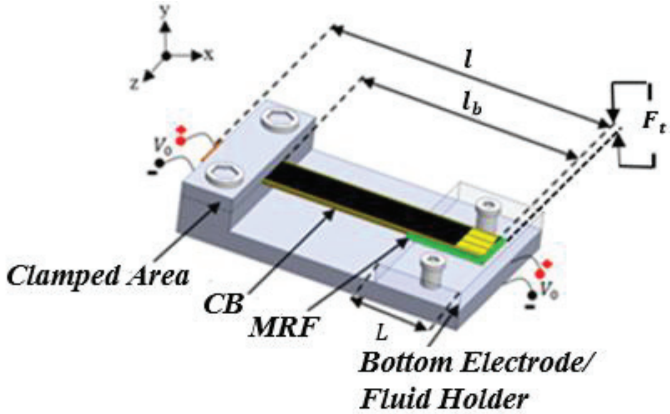


**Figure 2.1.** Configuration of CB-ERF active damping medium device

The structure presented a contact between the layer ERF and the tip end of the CB. This contact provides a high coefficient of compensation. The downwards displacement of the excitation of the clamped CB, where the tip comes into contact ERF, is in the squeeze mode. The impact between the activated ERF active damping medium and the tip of the vibrating CB produces impulse acceleration.

**Table 2.1.** Specifications of CB-ERF damping device

| Description | Value | Symbol |
|---|---|---|
| **Free (vibrating) length** | 36 mm | $l_b$ |
| **Total length** | 50 mm | $l$ |
| **Fluid layer** | 0.7 mm | $F_t$ |
| **Length of fluid holder** | 5 mm | $L$ |
| **Applied voltage** | 800 V, 900 V and 1 kV | $V_0$ |
| **Gap between electrodes** | 0.5 mm | $h_0$ |

The used CB is a piezoelectric cantilever beam consisting of a shim layer sandwiched in-between two active piezoceramic layers. CB that is used for this experiment was from Johnson Matthey Piezo Products GmbH, and it is shown in Annexe 2 [196]. In Table 2.1., the specifications of the CB-ERF damping medium device used in analytical and experimental works are presented.

### 2.2.1. ERF squeeze film analysis

The ERF active damping medium in this study was analysed in the squeezed mode. A normal force squeezes the ERF on impact. Figure 1.21. shows that the lower electrode is fixed to the base plate, while the upper electrode, in this case, is the vibrating CB, which is displaced in an upward and downward motion. The device exhibits a damping force caused by the viscosity resistance of the ERF, when the electric field is not applied to the ERF. By the application of voltage to the ERF, the electric field is generated through the gap between the bottom and the vibration electrodes. Additional damping is produced due to the yield strength of ERF [197].

The relations to estimate the characteristics of a squeeze-mode ERF damper are as follows:

$$F_d(t) = F_v(t) + F_{ERF}(t); \tag{2.1}$$

where $F_d(t)$ is the total damping force. $F_v(t)$ is the viscous damping force, and $F_{ERF}(t)$ is the controllable damping force associated with the applied electric field. These damping forces are defined by the following equations:

$$F_v(t) = \frac{L\mu w^4}{[h_0+h(t)]^3}\dot{h}(t), \tag{2.2}$$

$$F_{ERF}(t) = \frac{Lw^3}{[h_0+h(t)]^3}\tau(E)sgn\left(\dot{h}(t)\right); \tag{2.3}$$

where $h(t)$ and $\dot{h}(t)^{\cdot}$ are the displacement between the electrode and relative velocity of the cantilever beam. $h_0$ is the initial gap between the electrodes, L and w are the length and width of the electrode, and $\mu$ is the basic viscosity of the ERF when the electric field is zero. $\tau(E)$ is the applied voltage to the yield stress of the ERF. The applied voltage to the electrodes produces the electric field $(E)$.

Annexe 3 is a graph showing a typical relationship between the yield stress and the applied field given in the product catalogue of the choice of fluid for this study. The yield shear stress for the ERF varies depending on the electric field. The ERF used in this experiment is LID 3354s; the properties can be found in Annexe 4 [198]. The fibrillation of the activated ERF explains why it is the magnitude of the electric field $E$ and not the absolute voltage $V_0$, which determines the rheological response; although the two are related [199]:

$$E = \frac{V_0}{h}. \tag{2.4}$$

### 2.2.2. Dynamic response of CB-ERF system

The motion of the CB is represented as a single degree of freedom (SDOF) forced harmonic oscillator expressed as [200]:

$$\ddot{h}(t) + \left(c_{eff}/m\right)\dot{h}(t) + \left(k_{eff}/m\right)h(t) = F_p(t)/m + F_d(t)/m; \tag{2.5}$$

where $c_{eff} = c_{beam} + c_{ERF}$ is the total effective damping of the system, $k_{eff} = k_{beam} + k_{ERF}$ is the total effective stiffness of the system, $F_p(t)$ is the piezoelectric force, where $k_{beam}$is the stiffness of the free vibrating cantilever beam contact, which is expressed as follows [201]:

$$k_{beam} = \frac{3EI}{l_b^3}. \tag{2.6}$$

$l_b$ is the free (vibrating) length of the cantilever beam. The flexural rigidity of the cantilever beam $EI$ can be expressed as follows [202]:

$$I_{\mathrm{eff}} = 2I_{\mathrm{p}} + I_{\mathrm{sh}}; \tag{2.7}$$

where:

$$I_{\mathrm{p}} = \frac{1}{12} w t_p^3 + \mathrm{w} t_p \left(\frac{t_p - t_{sh}}{2}\right)^2, \tag{2.8}$$

$$I_{\mathrm{sh}} = \frac{E_{\mathrm{sh}}}{12 E_{\mathrm{p}}} w t_p^3. \tag{2.9}$$

The flexural stiffness of the cantilever beam $EI$ is given as:

$$EI = E_{\mathrm{p}} I_{\mathrm{eff}}.$$

The stiffness at the free end of the CB displaced in the vertical direction is expressed as follows [203]:

$$k_{beam} = \frac{3\mathrm{w}}{l_b^3}\left(\frac{2}{3} E_p t_p^3 + E_p t_p^2 t_{sh} + \frac{1}{2} E_p t_p t_{\mathrm{sh}}^2 + \frac{1}{12} E_{sh} t_{\mathrm{sh}}^3\right); \tag{2.10}$$

where $E_p = 1/S_{11}^E$ is Young's modulus of the piezoelectric layer, $S_{11}^E$, $w$ and $t_p$ are the piezoelectric compliance, the width of the cantilever beam and the thickness of the piezoelectric layer. $E_{sh}$ and $t_{sh}$ are the Young's modulus and the thickness of the shim. The effective mass is $m_{eff} = m_{beam}$, where the mass $m_{beam}$ of the vibrating cantilever beam is expressed as follows:

$$m_{beam} = \left(2\rho_p t_p + \rho_{sh} t_{sh}\right) \times l \times w; \tag{2.11}$$

where $\rho_p$ is the piezoelectric material density, and $\rho_{sh}$ is the density of the shim.

Figure. 2.2. shows the schematics of the vibration behaviour of CB. In Figure 1.22., the CB vibrates freely without an ERF active stopper. The stiffness of the CB $k_{beam}$ is constant during the displacement, and the vibration behaviour is linear. Figure 2.3. shows the semi-solid active stopper made of an activated ERF that is located under the bottom of the tip of the vibrating CB. When the CB is vibrating, the tip end impacts the activated solidified ERF stopper; the stiffness of the CB was converted from $k_{beam}$to $k_{ERF}$, where $k_{ERF} \gg k_{beam}$. From this stiffness effect, the vibration of the CB is transformed from a linear oscillation to nonlinear impact oscillation, as a result of the displacement constraints given by the ERF active stopper.

Giving that $k_{ERF} \gg k_{beam}$, there is an increase in the effective resonant frequency of the system. The resonance frequency will be expanded over a wider frequency range due to the increase in the stiffness of the ERF ($k_{ERF}$) At the point when the ERF active stopper behaves like a semi-solid due to the intensity of the electric field applied to the ERF in the squeeze mode, the stiffness becomes $\mathrm{k_{ERF}}(\mathrm{k_{ERF}} > \mathrm{k_{beam}})$ as shown in Figure 2.4., making the effective stiffness of the CB (after impact) changes from $\mathrm{k_{beam}}$ to $(\mathrm{k_{ERF}} + \mathrm{k_{beam}})$, and this shows that fluid and the end tip of the CB sticks together to vibrate for a part of a cycle, until they separate. This behaviour gives an increase in effective stiffness. The mechanical kinetic energy of the cantilever beam is transferred to the potential energy of the layer of ERF, without additional loss.

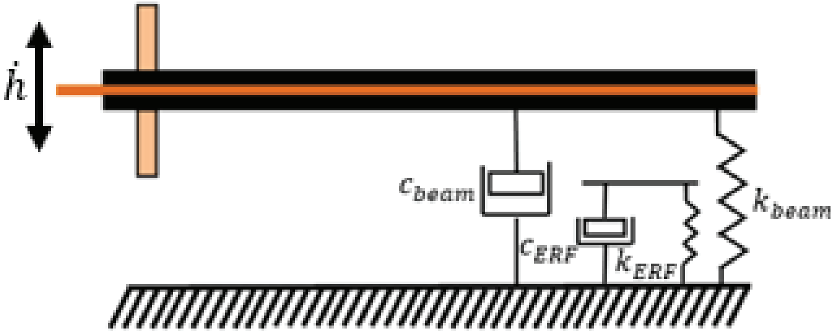


**Figure 2.2.** Schematic drawing of CB structure with ERF damping medium and its vibration behaviour, CB without any stopper

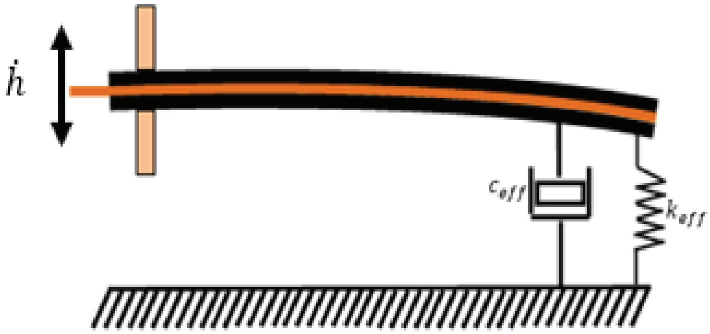


**Figure 2.3.** Schematic drawing of CB structure with ERF damping medium and its vibration behaviour, CB compressed

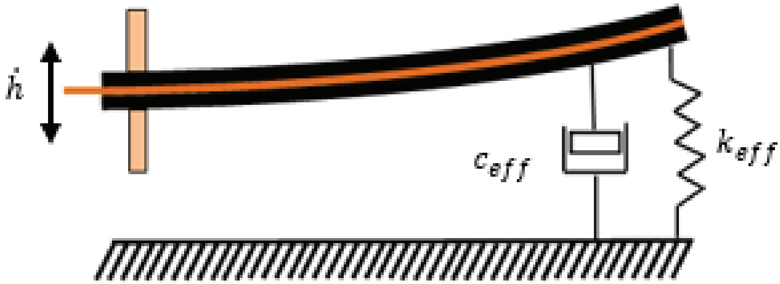


**Figure 2.4.** Schematic drawing of CB structure with ERF damping medium and its vibration behaviour, CB extended

Finding the stiffness ($k_{ERF}$) of ERF particle chain produced by ERF is calculated as shown below [204]:

$$k_{ERF} = \left|\frac{\partial F_{ERF}}{\partial y}\right| = \left(Lw\tau(E) + \frac{2\mu Lw}{h(t)}\right). \tag{2.12}$$

The resonant frequency of the active CB-ERF stopper system is given as follows:

$$\omega_n = \frac{1}{2\pi}\sqrt{\frac{k_{eff}}{m_{eff}}}. \tag{2.13}$$

In order to determine the free vibration of the CB, first, the logarithmic decay ratio was determined by the following formula [205]:

$$\delta = \frac{1}{n}\ln\left(\frac{X}{X_{n+1}}\right). \tag{2.14}$$

The equation 2.14 can be written as:

$$\delta = \frac{2\pi\lambda}{\sqrt{1-\lambda^2}}. \tag{2.15}$$

The following relation for damping ratio $\lambda$ was obtained from the equation. 2.10:

$$\lambda = \frac{c}{c_c} = \frac{c}{2m\,\omega_n} = \frac{\delta}{\sqrt{4\pi^2+\delta^2}}. \tag{2.16}$$

The equation 2.16 will give the following relation for damping factor c:

$$c = \frac{2\delta\sqrt{km}}{\sqrt{(\delta^2+4\pi^2)}}. \tag{2.17}$$

### 2.3. Experimental study of CB-ERF damping device

The schematic and experimental setup for the vibration control of cantilever beam, using active ERF damping medium at the tip, is shown in Figure 2.5. andFigure **2.6**. The experimental equipment that was used is comprised of a signal generator (Tabor WW5064) and a power amplifier (EPA-104) connected to the clamped piezoelectric cantilever beam. The generated excitation frequency was from 160 Hz to 300 Hz. In order to activate the ERF, a high-voltage with variable power DC supply 18 V 3 A was connected to the bottom copper plate electrode that holds the ERF. A laser displacement sensor (Keyence LK G82) was set above the vibrating CB at the free end. This device measures the displacement of the input excitation to the cantilever beam’s free end. The analog voltage signal recorded by the displacement sensor is sent to a controller (Keyence LK-G3001P), which is then processed and filtered by a PicoScope-3424 analog/digital oscilloscope. The oscillations are finally analysed on the computer connected to the oscilloscope.

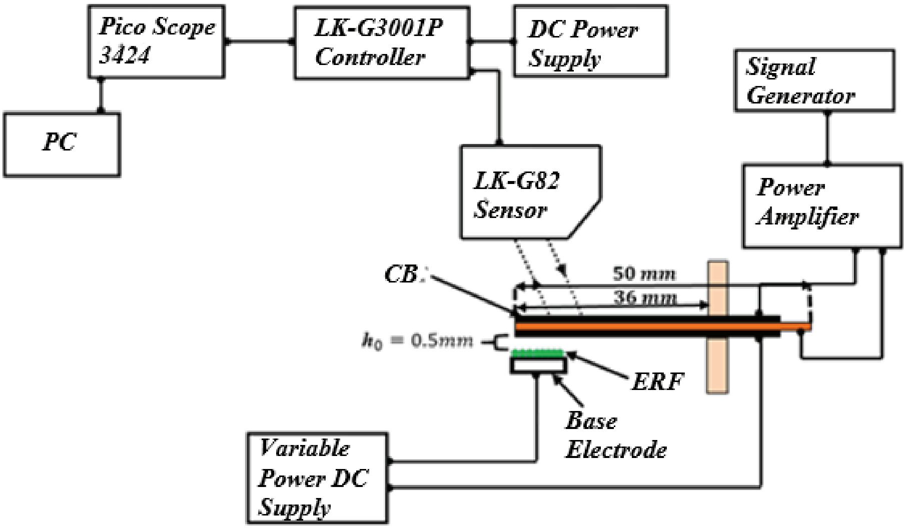


**Figure 2.5.** Schematic diagram for measuring the characteristics of CB with active ERF damping medium

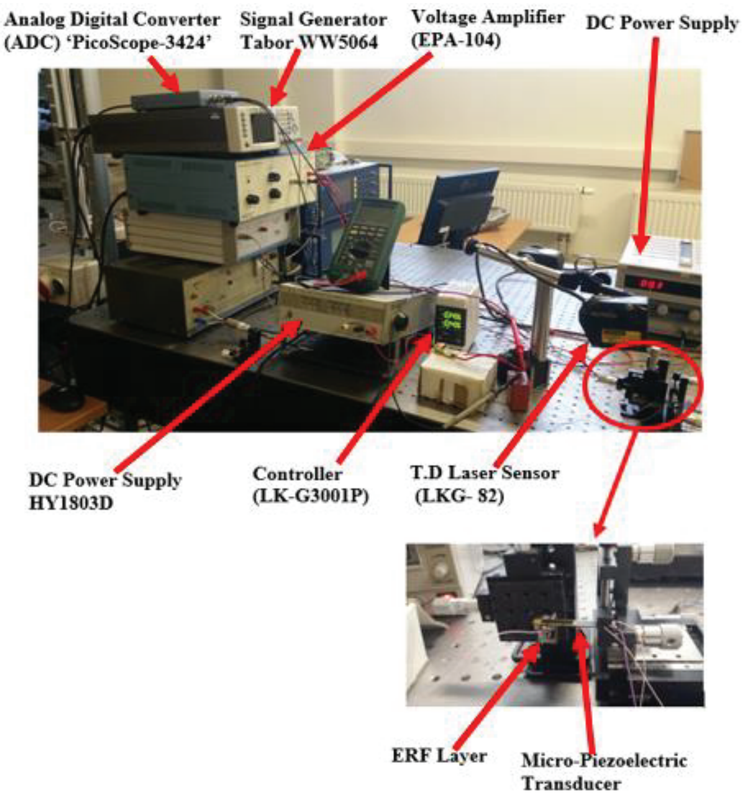


**Figure 2.6.** Experimental setup to measure the dynamic properties of the CB with active ERF damping medium

The experimental steps were conducted for the electric field ($E$), which was calculated from the equation 2.4. The calculated corresponding $E$ are 0 kV/mm (no voltage applied to ERF), 1.6 kV/mm, 1.8 kV/mm and 2 kV/mm. The corresponding yield stress $\tau(E)$ from the graph shown in Annexe 1 is 0 KPa, 0.7 KPa, 0.8 KPa and 1 KPa, respectively.

The ERF layer located at the tip of the cantilever beam behaves more like a complex spring with the stiffness $k_{eff} = k_{beam} + k_{ERF}$. In this study, the arrangement of the ERF layer is under compression/extensional deformation.

### 2.4. Dynamic simulation study of CB-ERF damping device in COMSOL Multiphysics

An equivalent model was simulated in COMSOL Multiphysics 5.4 Simulation software to predict the resonance frequency of the free vibrating CB, viscous ERF damping and the squeeze mode impact phenomena accurately. The purpose of the first dynamic simulations was to determine the mode shapes and the natural frequencies of the cantilever beam.

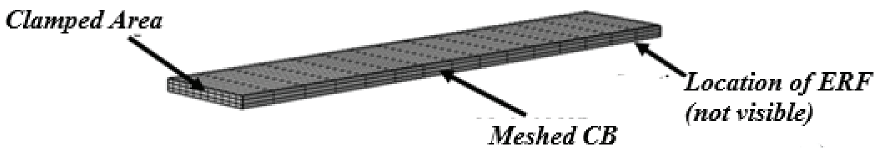


**Figure 2.7.** 3D finite element model of CB created with COMSOL Multiphysics; the cantilever beam has been meshed with swept distribution

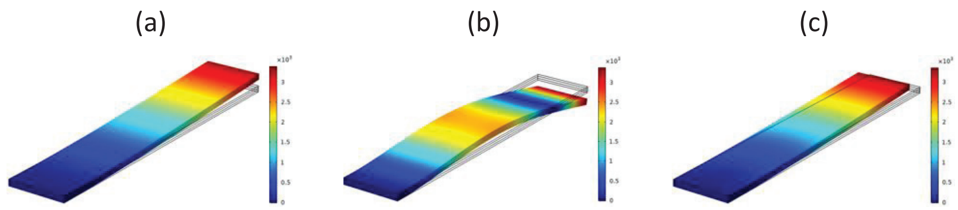


**Figure 2.8.** Simulated first four bending mode shapes and their corresponding natural frequencies: (a) 247 Hz, (b) 1551 Hz and (c) 2.4089 kHz

The FEM simulation in COMSOL starts by creating a 3D of the bimorph cantilever structure by using the given design parameters shown in Annexe 2. The model shown in Figure 2.7. reveals the geometry of the cantilever, incorporating channels, including the clamped area. The cantilever beam has been meshed with swept distribution

The first three natural bending frequencies of the CB were simulated in COMSOL Multiphysics. The values of the natural frequency ($\omega_n s$) simulated are as follows: $\omega_n s1$ = 247 Hz, $\omega_n s2$ = 1551 Hz and $\omega_n s3$ = 2.4089 kHz. The analytical values of natural frequency $\omega_n A$ of the CB is $\omega_n A1$ = 245 Hz, $\omega_n A2$ = 613.87 Hz, and $\omega_n A3$ = 1.0271 kHz. Figure 2.8. illustrates the simulated bending resonance modes of the cantilever beam structure.

## 2.5. Results and discussions

### 2.5.1. Results of CB-ERF system in frequency domain

The CB structure relates to the external dynamic forces, where frequency response depends on the stiffness and mass distribution of the structural elements. Similarly, the magnitude of this vibration is controlled by the damping characteristics exhibited by the ERF damping medium. For that matter, the vibration characteristics of the CB with the ERF damping medium were studied. The resonant natural frequencies under different configurations of the electric field were studied first. The significant shift presented in this study was the resonant frequency

The analytical values of natural frequency $\omega_n A$ of the CB is $\omega_n A1$ = 245 Hz, $\omega_n A2$ = 613.87 Hz and $\omega_n A3$ = 1.0271 kHz. From the above provided results, it is clear that simulated natural frequencies are close to the analytical values.

In order to obtain the vibrational characteristics of the CB, firstly, the frequency response of the vibrating CB without ERF damping medium was obtained. Secondly, the results presented in this study are obtained according to the 1st mode frequency of the ERF at various electric field conditions. The simulated frequency response results in Table 2.2. shows a frequency increase of 13.46 % for CB with activated ERF at 2 kV/mm, compared to the one without the activated ERF. However, the analytical results showed an increase in the frequency of the CB of 16.2 % with activated ERF at 2kV/mm, compared to the one without the activated ERF. An increase in the frequency of CB, as the applied electric field to the ERF, increased by 12.4 % experimentally with the electric field of 2 kV/mm.

Figure 2.9.,Figure **2.10**.,Figure **2.11**.,Figure **2.12**. andFigure **2.13**. show the vibration spectra obtained from the CB without ERF damping and with activated ERF medium at 0, 1.6, 1.8 and 2.0 kV/mm, respectively. It has been observed in these results that the natural frequency of the CB decreases as the electric field increases. This behaviour agrees with the theoretical prediction in most sandwiched cantilever beam studies, such as the one described in [206].

**Table 2.2.** Vibration parameters of CB with ERF active damping medium for the vibration system

| | **Natural frequency ($\omega_n$) (Hz)** | | | **Amplitude (mm)** | | |
|---|---|---|---|---|---|---|
| **Electric Field ($E$) Conditions (kV/mm)** | Hand Calculation | Simulated | Experimental | Hand Calculation | Simulated | Experimental |
| **Without ERF** | 245 | 247 | 249 | 0.38 | 0.33 | 0.44 |
| **0** | 250 | 252 | 257 | 0.30 | 0.26 | 0.36 |
| **1.6** | 256 | 260 | 266 | 0.28 | 0.21 | 0.30 |

| | | | | | | |
|---|---|---|---|---|---|---|
| **1.8** | 272 | 275 | 275 | 0.18 | 0.15 | 0.24 |
| **2** | 278 | 282 | 280 | 0.15 | 0.13 | 0.20 |

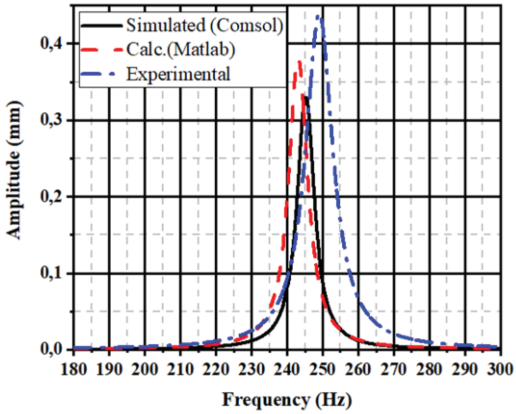


**Figure 2.9.** Frequency respond results of the CB without ERF damping medium

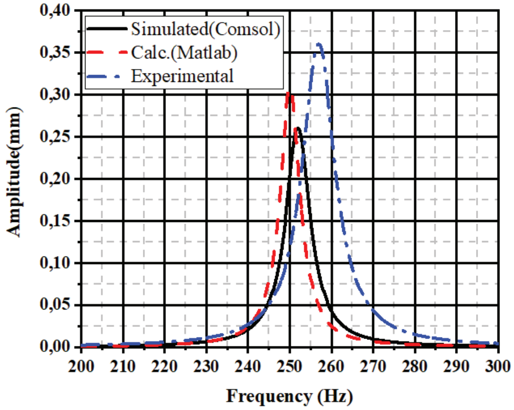


**Figure 2.10.** Frequency response results of the CB with activated ERF medium at 0 kV/mm

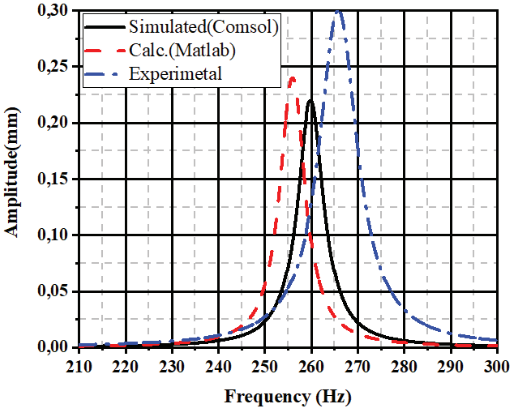


**Figure 2.11.** Frequency response results of the CB activated ERF medium at 1.6 kV/mm

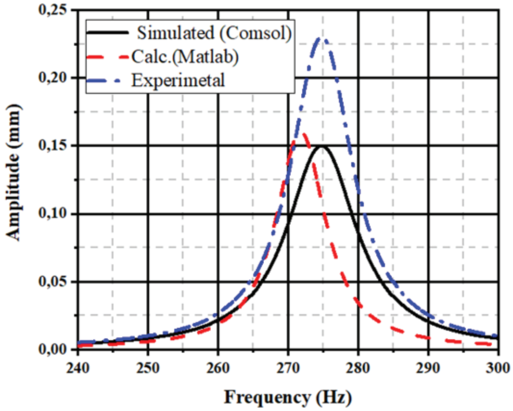


**Figure 2.12.** Frequency response results of the CB with activated ERF medium at 1.8 kV/mm

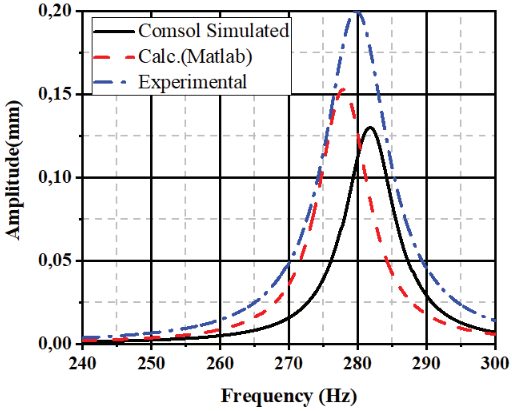


**Figure 2.13.** Frequency response results of the CB with activated ERF medium at 2.0 kV/mm

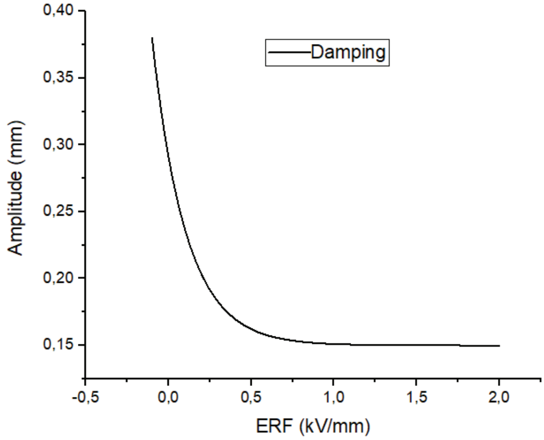


**Figure 2.14.** Comparison of the damping rate for the calculated model

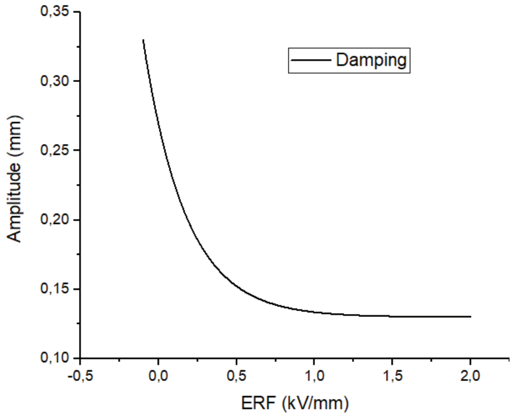


**Figure 2.15.** Comparison of the damping rate for the simulated model

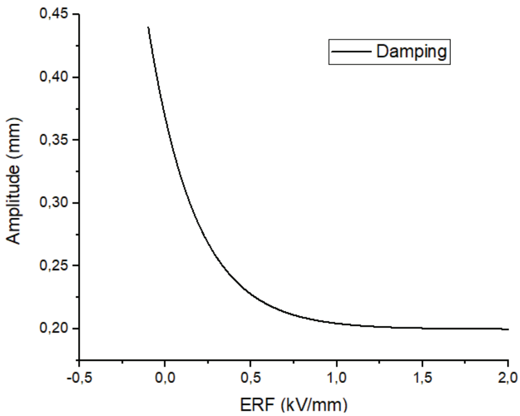


**Figure 2.16.** Comparison of the damping rate for the experimental model

Figure 2.14., Figure **2.15**. and Figure **2.16**. show the comparison graph of the rate of change in damping between the amplitude and the activated ERF for the calculated, simulated and experimental models, respectively. From these graphs, it is clear that the damping decreases as the field increases.

### 2.5.2. Experimental results of CB ERF system in time domain

As indicated in the simulated and analytical tests, the data obtained from the CB with ERF damping medium was studied without the electric field and compared to the one with the applied electric field. The CB was excited by the frequency ranging from 160 Hz to 300 Hz. The effect of the electric field intensity on the behaviour of the ERF damping medium on the CB was studied as well.

The curves for the free vibration of the CB-ERF damping medium are shown in Figs 2.17., 2.18., 2.19., 2.20. and 2.21. This presents the peak to peak time response oscillation of the CB-ERF damping medium in the absence and presence of the electric field (1.6 kV/mm, 1.8 kV/mm and 2 kV/mm). As it is can be observed from the results shown in graphs and Table 2.2., the CB damping increases considerably with the applied electric field. The rate of decay of the response shown on-time response plots can be described in terms of the damping ratio as shown in equation 2.15. The damping ratio in the absence of the magnetic field is 0.20 %; it increases to 0.45 % with a field of 2 kV/mm.

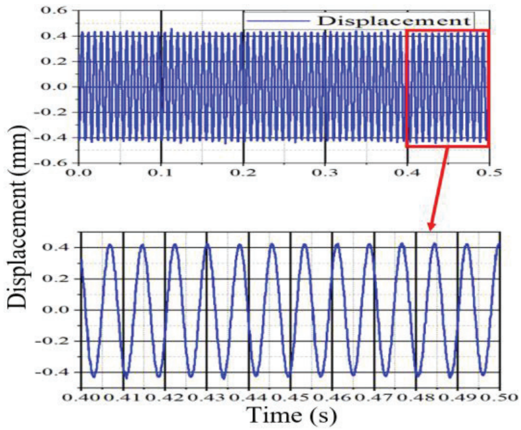


**Figure 2.17.** Experimental results of oscillating CB with no ERF damping medium

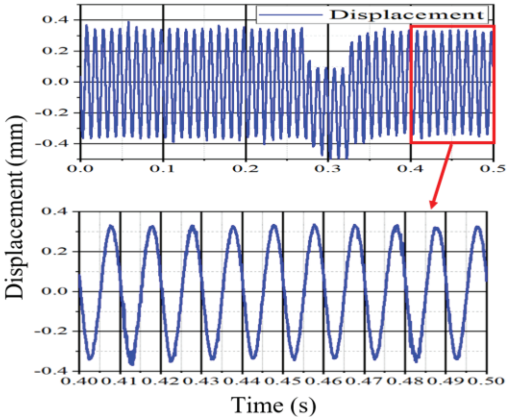


**Figure 2.18.** Experimental results of oscillating CB with activated ERF damping medium at 0 kV/mm

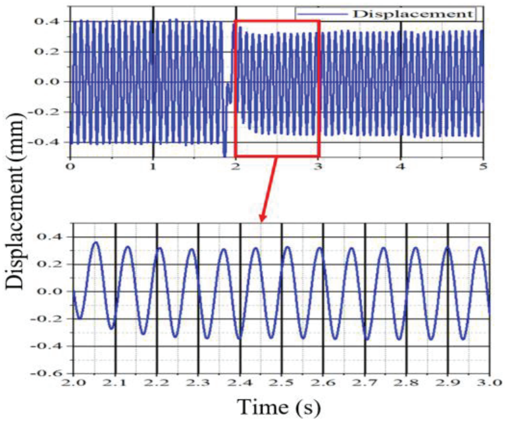


**Figure 2.19.** Experimental results of oscillating CB with activated ERF damping medium at 1.6 kV/mm

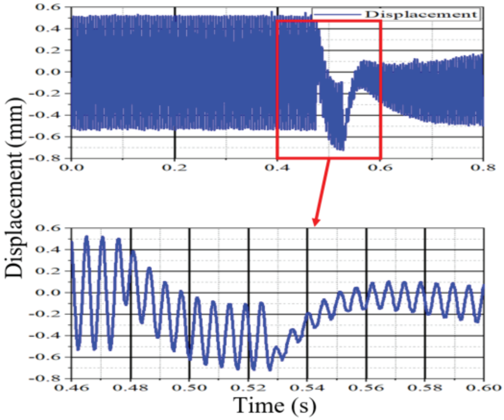


**Figure 2.20.** Experimental results of oscillating CB with activated ERF damping medium at 1.8 kV/mm

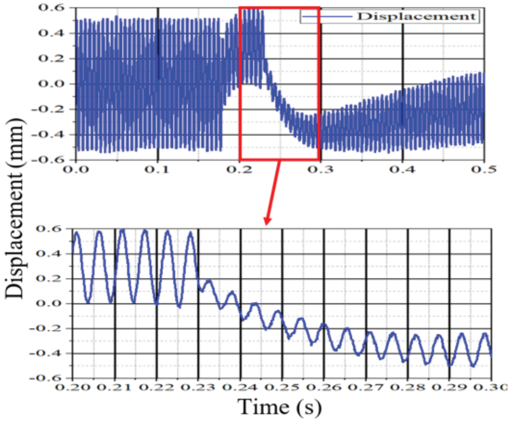


**Figure 2.21.** Experimental results of oscillating CB with activated ERF damping medium at 2.0 kV/mm

The variations of electric field intensities were obtained by varying the application of a voltage, concerning the gap between the electrodes as shown in equation 2.4. It has been observed that for stronger electric fields (E=2 kV/mm), the resonant natural frequencies are shifted to higher frequencies with higher vibration levels. This behaviour might be due to the mass concentration of the electromagnetic particles in specific ERF and non-homogeneous stiffening of the ERF under compression and stretching. The natural frequencies CB-ERF damping medium was experimentally tuned for the electric up to 12.4 %, and the vibration levels increased as much as 0.20 mm. At the same time, there was an improvement in the damping properties of the CB, since the vibration level decreased significantly.

The frequency shift was observed in analytical and simulation results. This was expected due to the stiffness of the CB when it impacts the activated ERF. The CB showed an increase in frequency, as the applied electric field to the ERF increases at 12.4 % experimentally with an electric field of 2 kV/mm. However, the simulation and the analytical results showed that the frequency of the CB increased from 16.2 % and 13.46 %.

## 2.6. Conclusions

In this chapter, the analytical simulation and experimental study of the frequency tenability of CB due to the shift in frequency with the ERF damping medium is described. The results have proven that it is possible to localise layer ERF as a damping medium under a vibrating structure. The results have shown a similarity to that of the sandwiched ERF/MRF vibrating structures that most researchers have studied.

The stiffness and damping characteristics of the CB-ERF damping medium were investigated as a function of different electric field configurations and intensities.

The observed analytical, simulated and experimental vibration characteristics of the CB are summarized as follows:

1. The time-domain decay-rate oscillations presented in the experimental results demonstrated that the changes in displacement of the structure creating damping were due to the influence of the electric field applied to the ERF. The CB showed an increase in damping of 54.5 % experimentally with an electric field of 2 kV/mm. However, the simulation and the analytical results demonstrated that the increase in the damping of the CB was more significant, going from 54.5 % and 52.6 %.

2. The CB-ERF as well demonstrated bigger shifts in natural frequencies for the same electric field level and configuration. This was expected, since the stiffness of the CB changes after affecting the activated ERF. It was shown that the CB's frequency increased with the applied electric field. The increase in the frequency of CB as the applied electric field to the ERF increased at 12.4 % experimentally with the electric field of 2 kV/mm. However, the simulation and the analytical results showed an increase in the frequency of the CB from 16.2 % and 13.46 % respectively.

The studies as well encountered some limitations in the experimental studies. The nonlinear nature of the ERF has shown instability in results. Nevertheless, the results demonstrated that localising the ERF layer under the vibrating cantilever beam device is achievable.

# 3. FREQUENCY TUNING OF A PIEZOELECTRIC ENERGY GENERATOR VIA THE APPLICATION OF MRF IMPACTING

## 3.1. Introduction

The following chapter will briefly review the approaches to frequency tuning of piezoelectric energy generators and determine the application of the MRF impact based on the frequency enhancer technique, where low-frequency input vibrations are converted into high-frequency vibrations of electromechanical transduction. The mathematical theory on the effect of impacting MRF on the natural frequency of a cantilever beam was documented. The results from the mathematical theory, finite element simulation and the results from the experiment were compared. It has been found that there was an increase in the natural frequency and power output with the MRF impacting technique.

## 3.2. Mathematical study of PEG

The proposed piezoelectric bimorph energy generator and mode of operation are shown in Figure 3.1. The system consists of a vibrating piezoelectric bimorph cantilever beam and two permanent magnets that are mounted on the opposite sides of the beam. The MRF, as an impacting element, is attached to one of the permanent magnets. The permanent magnets are arranged to face each other with opposite poles and a gap $d_m$ apart in the horizontal x-plane. The system was modelled with the magnets placed at $0.8l_b$ of the free length of the piezoelectric bimorph cantilever beam. Figure 3.2. and Figure **3.3**. show the working principle of the PEG system[6].

[6] *This section contains information from the article of the author with the details below: International Journal of Green Energy, vol. 17, Issue 9, pp. 529–539, 2020, doi: /10.1080/15435075.2020.1763356. Modeling and Study of Magnetorheological Fluid Impact Base Frequency Enhancement for a Micro-Piezoelectric Energy Generator.*

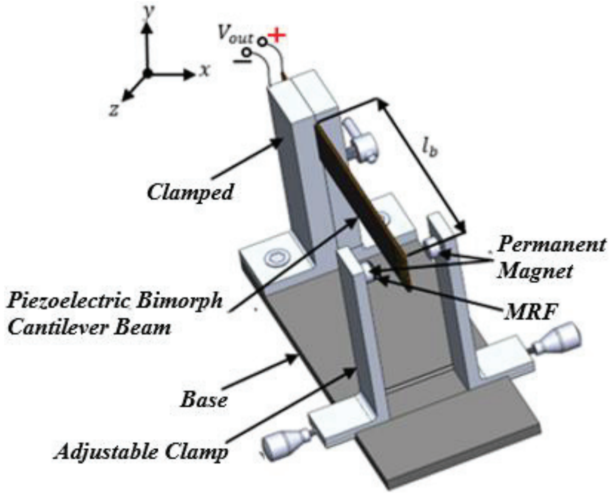


**Figure 3.1.** Proposed MRF PEG

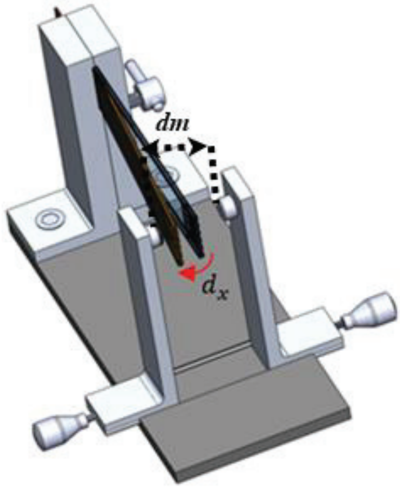


**Figure 3.2.** Displacement of excited cantilever beam impacting the MRF

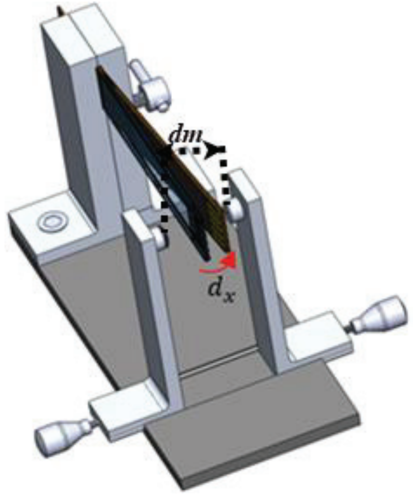


**Figure 3.3.** Pull away displacement of the excited cantilever beam

A piezoelectric bimorph cantilever beam was chosen for this application. This kind of cantilever beam is a typical piezoelectric device that has many mechanical vibrational applications such as energy harvesting for battery-free remote-control switches, a battery-free power supply for sensors in the field of automation technology, control systems and tire pressure monitoring systems and many more. The type of piezoelectric bimorph cantilever beam that was considered for this study is as well known as "Piezo Bending Actuator 427.0085.11Z" from Johnson Matthey Piezo Products GmbH [207]. Annexes 2 and 3 show a typical piezoelectric bimorph cantilever beam and its properties.

Figure 3.4. shows a single degree of freedom (SDOF), spring-mass-damper model, to illustrate the linear modelling of the MRF based impacting piezoelectric energy generating device. The equations of motion for the system are given below:

$$m_{eff}\ddot{x} + c_{total}\dot{x} + k_{eff}x = f; \tag{3.1}$$

where $m_{eff}$ is the cantilever beam, given as:

$$m_{eff} = \left(2\rho_p t_p + \rho_{sh} t_{sh}\right) \times L \times w. \tag{3.2}$$

$c_{total}$ is the total damping coefficient, which is the sum of the damping of the cantilever beam $c_{beam}$ and damping caused by MRF $c_{MRF}$. $k_{eff}$is the effective stiffness, which is the sum of the beam stiffness $k_{beam}$ and stiffness caused by the MRF $k_{MRF}$, and f is the external force applied to the piezoelectric cantilever beam. $x$ is the tip displacement of the cantilever beam at a distance of $h$ between the MRF and piezoelectric cantilever beam.

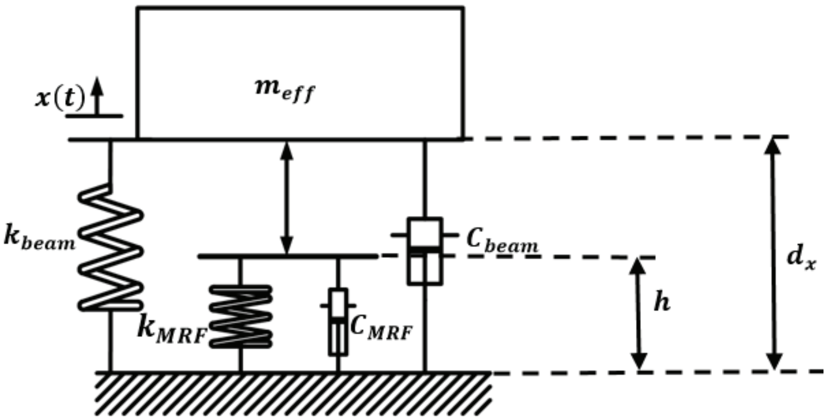


**Figure 3.4.** SDOF of the MRF energy generating system

The rheological properties of MRF, due to the intensity of the magnetic field, determine the effective stiffness of the beam at the point of impact. The stiffness of the cantilever beam $k_{beam}$ is constant during the displacement, and the vibration behaviour is linear. The arrangement of stiffness of the beam $k_{beam}$ to the stiffness of MRF $k_{MRF}$ are aligned in parallel. At the point of impact with the MRF, the stiffness of the vibrating cantilever beam is converted from $k_{beam}$ to $k_{MRF}$, where $k_{MRF} \gg k_{beam}$ . From this stiffness effect, the vibration of the cantilever beam is transformed from linear oscillations to nonlinear impact oscillations, as a result of the displacement constraints given by the MRF stopper. Then, the stiffness becomes $k_{MRF}(k_{MRF} > k_{beam})$, making the effective stiffness of the cantilever beam (after impact) change from $k_{beam}$ to $(k_{MRF} + k_{beam})$, and this shows that there is an adhesive or tensile force between the vibrating cantilever beam and MRF for the part of the vibrating cycle, until the magnetic particles are dispersed. This behaviour gives an increase in the effective stiffness, which in effect changes the frequency response of the cantilever beam and diverges from its normal behaviour, allowing resonance to extend over a wider interval, in the vicinity of its resonant frequency. The kinetic energy of the cantilever beam is transformed into the potential energy of the layer of MRF without the additional loss.

The first point to consider in modelling the MRF is the yield stress of the fluid as a function of the magnetic field. The MRF type that is considered for the application in this study is the MRF 140-CG [208]. The properties of this type of MRF are listed in Annexe 6.

The yield stress $\tau_B(H)$ of this type of fluid is given by an experimentally derived equation, which depends on the magnetic field intensity and the particle volume fraction $\varphi$ as [209].

$$\tau_B(H) = C \times 271700 \times \varphi^{1.5239} \times tanh(6.33 \times 10^{-6}H); \tag{3.3}$$

where $C$ is a coefficient dependent on the carrier fluid of the MRF, and $H$ is the magnetic field intensity.

The change in the viscosity of the MRF is used to generate a viscous force between the two surfaces of both magnets, which is in relative motion due to the vibrating cantilever beam. The equation, which relates the magnetic flux density $B$ to the magnetic field intensity $H$ [210], is as follows:

$$B = 1.91 \times \varphi^{1.133}\{1 - [\mu_0 e^{-10.97\mu_0 H}]\} + \mu_0 H. \tag{3.4}$$

Therefore, MRF stiffness $k_{MRF}$ and squeeze damping $c_{MRF}$ depend on the force $F_{MRF}$ , the yield stress $\tau_B(H)$. The determination of $\tau_B(H)$ depends on the distance $d_m$ between the two permanent magnets as shown in Figure 3.2. andFigure **3.3**.

The force generated due to the magnetic field intensity and with the fluid $F_{MRF}$ fixed at its free end is given as [211]:

$$F_{MRF} = \frac{4}{3}\frac{\pi r_m^2 \tau_B(H)}{(h+x)} sign(\dot{x}); \tag{3.5}$$

where $\tau_B(H)$ is the yield stress of the MRF given in equation 3.3, $r_m$ is the radius of the magnet, $h$ is the initial gap between the MRF and cantilever beam, and $x$,$\dot{x}$ are the displacement of the cantilever beam.

The force due to the MRF is just an approximation and does not consider the hysteresis effect between the magnets, while the MRF is either being compressed or separated from the oscillation of the cantilever beam. The magnitude of the magnetic stiffness $k_{MRF}$ is analytical from $F_{MRF}$, as shown in [212]:

$$k_{MRF}(h) = \left|\frac{\delta k_{MRF}}{\delta h}\right| = \left|\frac{\partial k_{MRF}}{\partial h}\right|, \tag{3.6}$$

$$k_{MRF} = \frac{4}{3}\frac{\pi r_m^3 \tau_B(H)}{(h+x)^2}. \tag{3.7}$$

The equivalent stiffness of the cantilever beam is given as in [213]:

$$k_{beam} = \frac{3E_p I}{l_b^3}; \tag{3.8}$$

where $I$ is the moment of inertia. The moment of inertia of the reference layer can be expressed as shown in equation 3.9, and $l_b$ is the free (vibrating) length of the cantilever beam [214]:

$$I = \frac{w}{12}\left(\frac{E_{sh}}{E_p} t_{sh}^3 + 2t_p^3\right) + \frac{wt_p}{2}\left(t_{sh} + t_p\right)^2; \tag{3.9}$$

where w is the cantilever beam width, $E_{sh}$ is the shim layer modulus of elasticity, $E_p$ is the Young's modulus of piezoelectric material, $t_{sh}$ is the shim layer thickness, and $t_p$ is the thickness of the ceramic layer of the piezoelectric cantilever beam.

The resonant frequency of the generating system is given as follows:

$$\omega_{sys} = \sqrt{\frac{k_{eff}}{m_{eff}}}; \tag{3.10}$$

where $k_{eff}$ is the effective stiffness of the cantilever beam and $m_{eff}$ is the effective mass of the cantilever beam.

The damping ratio of the system is defined as the mechanical energy losses due to the fluid squeeze force [215]. Therefore, the total mechanical damping is given as $c_{total} = c_{MRF} + c_{beam}$.

The damping effect owing to the squeeze force is due to the flow of viscous fluid through the small gaps, which can be calculated as follows:

$$c_{MRF} = \frac{3}{2}\frac{\pi \eta r_m^4}{(h+x)^3}; \tag{3.11}$$

where $\eta$ is the viscosity of the MRF. The damping coefficient of the piezoelectric cantilever beam $c_{beam}$ can be expressed as [216, 217]:

$$c_{beam} = 2 \times \zeta \times m_{eff} \times \omega_{beam}; \tag{3.12}$$

where $\zeta$ is the damping ratio the free vibrating cantilever beam, giving $\delta/2\pi$. $\delta$ is the log decrement corresponding to $\delta = (1/n)(ln\, z_1/z_{n+1})$.

### 3.2.1. Modelling of the output power of PEG

The equation 3.10 shows the resonant frequency of the vibrating cantilever beam. The piezoelectric material conserves most of the generated power. In order to generate the electrical power, a resistive load is required. The electrical load is modelled as a single resistor. It is described by [218] that the output power reaches its maximum value when the calculated load resistance described by equation 3.15 is applied. The averaged power generated by a bimorph piezoelectric cantilever beam according to [219] is given as follows:

$$Power = \frac{{\omega_{sys}}^2 {t_{sh}}^2 w^2 {e_{31}}^2 x^2}{4\left(1 + w l_b \varepsilon_{33} \times \frac{\omega_{sys} R}{t_p}\right)^2} \times R; \tag{3.14}$$

where $\omega_{sys}$ is the resonant frequency of the MRF-based system, $t_{sh}$ is the shim layer thickness, $w$ is the width of the cantilever beam , $x$ is the max deflection and $t_p$ is the thickness of the piezoelectric layer. $e_{31}$ is piezoelectric constant. The load resistance $R$ of the piezoelectric material is given as [220]:

$$R = \frac{1}{C_p \omega_{sys}}; \tag{3.15}$$

where $C_p$ is the capacitance of the piezoelectric bimorph.

### 3.2.2. Conversion power efficiency due to the impact of PEG

The efficiency of the system depends on the conversion of mechanical energy to electrical energy. The power generated from the MRF impacts the piezoelectric bimorph cantilever beam energy generator compared with the power generated without the impact. The efficiency model that is used in this work was the one proposed by [221]. In this formula, the energy conversion efficiency $eff$ was defined as the ratio of the generated electrical power $(P_L)$ in the load resistor $R_L$ to the consumed power ($P_c$) in the entire energy generator device, including the load resistor, at $= \omega_{sys}$ , which derived as:

$$eff \approx \frac{P_L}{P_c} = \frac{k_{33}^2/2(1-k_{33}^2)}{(1/Q_m + k_{33}^2/2(1-k_{33}^2))}; \tag{3.16}$$

where $Q_m$ is the mechanical quality factor of the piezoelectric bimorph. The load resistance $R_L$ is given in equation (3.15). $k_{33}$ is the Piezoelectric coupling coefficient.

### 3.3. FEM study of PEG

The generated power from the piezoelectric bimorph cantilever beam depends on the magnetic field intensity on the MRF, which corresponds to the gap ($d_m$) between the two permanent magnets and MRF stopper. Figure 3.5. shows the simulation of the magnetic circuit to develop the required magnetic field that affects the characteristics of the MRF in COMSOL Multiphysics. The permanent magnet considered for this simulation is Nd-Fe-B (N42) [222]. The magnetic field was used to identify the magnetic poles (north and south) and measure the magnetic flux generated by the magnets.

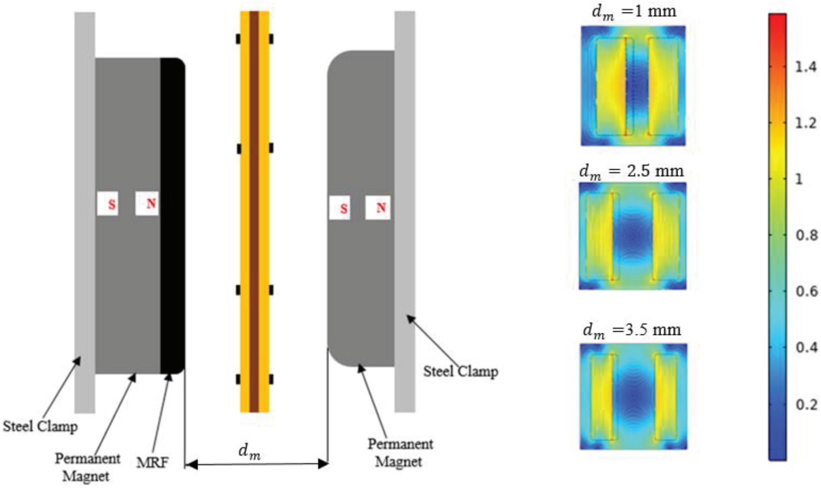


**Figure 3.5.** FEM simulation of magnetic flux density at different magnetic gaps ($d_m = 1\ mm$ , $d_m = 2.5\ mm$ and $d_m = 3.5\ mm$)

The simulation conducted on MRF and the piezoelectric bimorph cantilever beam was classified as follows: free vibration of the cantilever beam (i) without fluid corresponding to 0 T, when the gap between the permanent magnets, (ii) $d_m = 1\ mm$ , corresponding to 0.3 T, (iii) $d_m = 2.5\ mm$, corresponding to 0.2T, and (iv) $d_m = 3.5\ mm$, corresponding to 0.1 T.

### 3.4. Experimental study

In order to verify the mathematical and FEM presented in this study, the experimental study was conducted. Figure 3.6. shows the experimental setup of the clamped piezoelectric bimorph cantilever beam. The piezoelectric cantilever beam is excited between two permanent magnets with a layer of MRF attached to one magnet facing the cantilever beam. The layer of MRF placed on top of the permanent magnet is 0.06 mm thick.

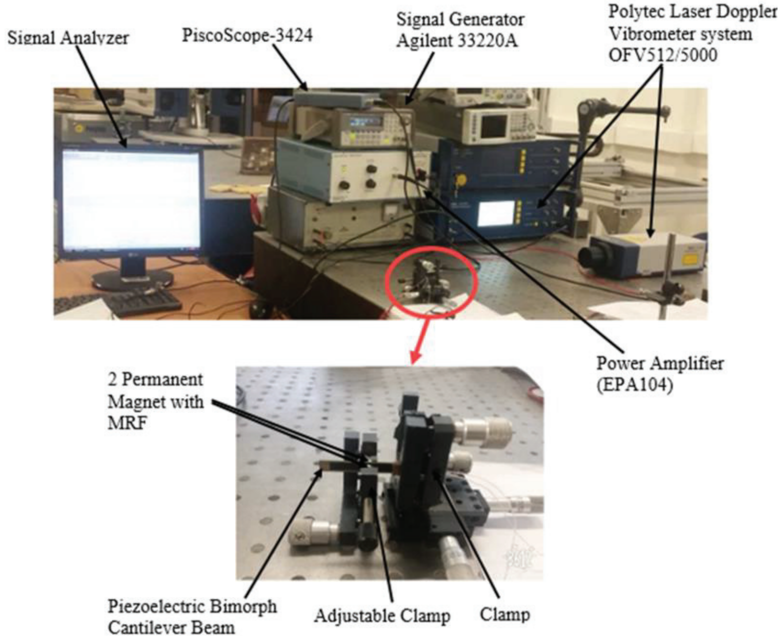


**Figure 3.6.** Experimental setups of impact-based frequency enhancement using vibrating bimorph piezoelectric energy generator

The main equipment used in the experiment is the bimorph cantilever beam, two permanent magnets Nd-Fe-B (N42), an amplifier, a signal generator, a laser vibrometer and an oscilloscope. A magnetic field Gauss Meter (HHG191) was used to identify the magnetic poles (north and south) and measure the magnetic flux generated by the magnets.

A signal generator (Signal Generator Agilent 33220A) was used to excite the piezoelectric bimorph cantilever beam with a set swept sine actuation frequency ranging from 0 Hz to 300 Hz. The vibration response of the piezoelectric bimorph cantilever beam was measured by a non-contact Laser Doppler Vibrometer (Polytec Laser Doppler Vibrometer system OFV512/5000). This is a single-point Laser Doppler Vibrometer with a He-Ne (Helium-Neon). The oscilloscope (PiscoScope-3424 collected signals from a laser vibrometer) sent them to the signal analyser. The signals were processed and Fourier transformed to get the natural frequencies of the cantilever beam. The vibration data response was obtained in the frequency domain where the results of the natural frequencies and amplitudes of vibration were presented.

### 3.5. Results and discussion

The results from Table 3.1. have proven that the frequency could be tuned when a vibrating cantilever beam is impacted by an activated MRF stopper. A frequency increase was observed when there is an increase in the magnetic field applied to the MRF. From the analytical perspective, the results showed 4 % increase in the frequency from a free vibrating cantilever beam without the impact on the MRF stopper to the highest magnetic field of 0.3 T application to the MRF stopper. The results from the FEM simulation model showed 3.8 % increase in frequency when 0.3 T magnetic field is applied to the MRF stopper as compared to the free vibrating cantilever beam without the MRF stopper. However, the experimental results showed a frequency increase of 6.5 % at 0.3 T magnetic field application. Therefore, the experimental results validate the frequency enhancement of the analytical results and FEM simulated results. The results as well show a decrease in amplitude when the magnetic field is increased as demonstrated in Table 3.2. This explains the effects of the rheological properties of the MRF on the damping. The results that are demonstrated in this research, compared to other frequency tuning articles, are similar. For example, the results are similar to the ones reported by [223], where the results clearly showed a substantial increase in the natural frequencies with increasing magnetic flux density. Figure 3.7., Figure **3.8**.,Figure **3.9**. andFigure **3.10**. presented the graphs of the analytical, FEM simulation and experimental results of the frequency response of the piezoelectric bimorph cantilever beam with MRF stopper.

**Table 3.1.** Comparisons of computed frequency response to simulated and experimental response

| Magnetic Field (T) | Natural Frequency ($\omega_n$) (Hz) | | | | | |
|---|---|---|---|---|---|---|
| | **Analytical** | **FEM** | **Experimental** | **Percent Deviation Analytical and FEM** | **Percent Deviation Experimental and Analytical** | **Percent Deviation Experimental and FEM** |
| **No field** | 233 | 232.8 | 230 | 0.1 | 1.3 | 1.2 |
| **0.1** | 236 | 235.9 | 232 | 0.1 | 1.7 | 1.7 |
| **0.2** | 240 | 240.5 | 242 | 0.2 | 0.8 | 0.6 |
| **0.3** | 243 | 241.9 | 245 | 0.5 | 0.8 | 1.3 |

**Table 3.2.** Comparisons of computed amplitude to simulated and experimental response

| Magnetic Field (T) | Natural Frequency ($\omega_n$) (Hz) | | | Peak Amplitude (mm) | | |
|---|---|---|---|---|---|---|
| | Analytical | FEM | Experimental | Analytical | FEM | Experimental |
| **No field** | 233 | 232.8 | 230 | 4.1 | 4.3 | 4.0 |
| **0.1** | 236 | 235.9 | 232 | 3.8 | 3.9 | 3.5 |
| **0.2** | 240 | 240.5 | 242 | 3.6 | 3.4 | 3.3 |
| **0.3** | 243 | 241.9 | 245 | 3.2 | 3.1 | 2.8 |

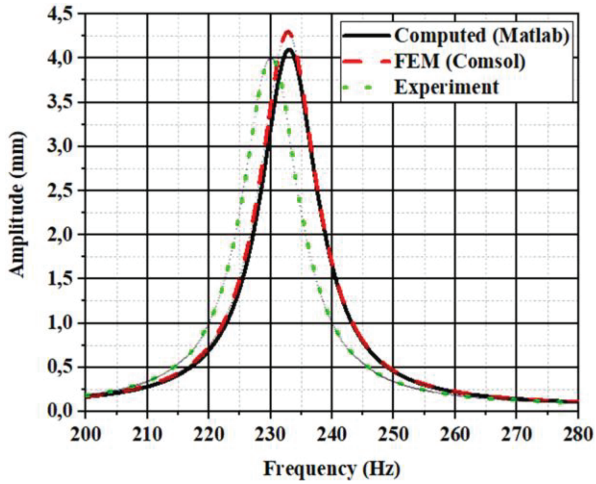


**Figure 3.7.** Frequency response of the piezoelectric bimorph cantilever beam with no MRF stopper

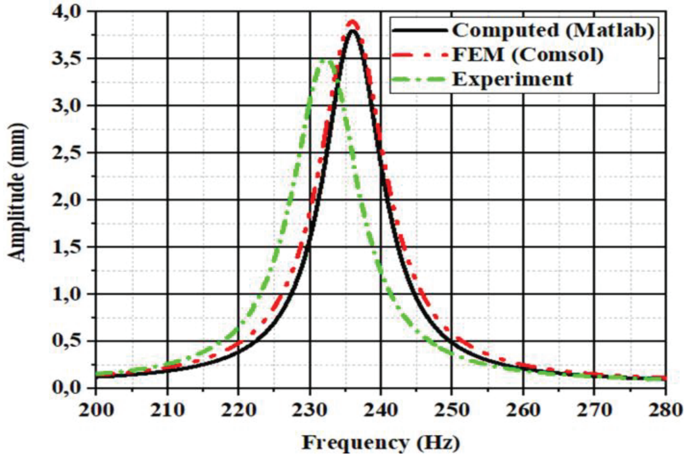

**Figure 3.8.** Frequency response of the piezoelectric bimorph cantilever beam with MRF stopper at 0.1T

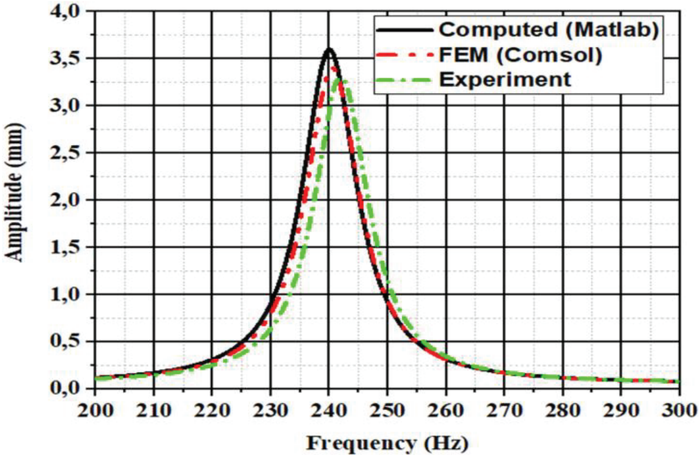


**Figure 3.9.** Frequency response of the piezoelectric bimorph cantilever beam with MRF stopper at 0.2T

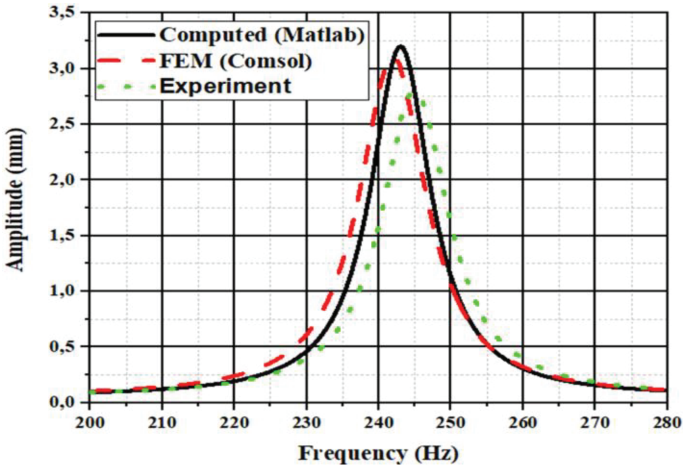


**Figure 3.10.** Frequency response of the piezoelectric bimorph cantilever beam with MRF stopper at 0.3T

Table 3.2. shows the analytical and simulation results for the theoretical output power that was generated. From equation 3.14, the calculated power output results in Table 3.3. revealed that the ability to tune the frequency of the system has paved the way to model and compute the amount of power that can be harnessed from this system. The analytical load resistance and corresponding power output were calculated by using equations 3.15 and 3.14. The maximum power achieved from the FEM simulation study was 410 $\mu W$ and a load resistance of 37 $k\Omega$ when the cantilever beam impacts the activated MRF at 0.3T magnetic field application. However, the analytical results show a maximum power output 410 $\mu W$ and a load

resistance of 37.2 $k\Omega$. A power output of 403 $\mu W$ was obtained from the experimental studies at 0.3 T and with a load resistance of 36.7 $k\Omega$. These results showed 38 % increase in power from the vibrating cantilever beam without affecting the MRF stopper to impact the MRF with 0.3 T magnetic field application for the FEM analysis. The analytical results gave 42 % increase in the out-power for the vibrating cantilever beam impacting the MRF at 0.3 T magnetic field application, compared to the free vibrating cantilever beam. The experimental results as well gave 68.6 % increase.

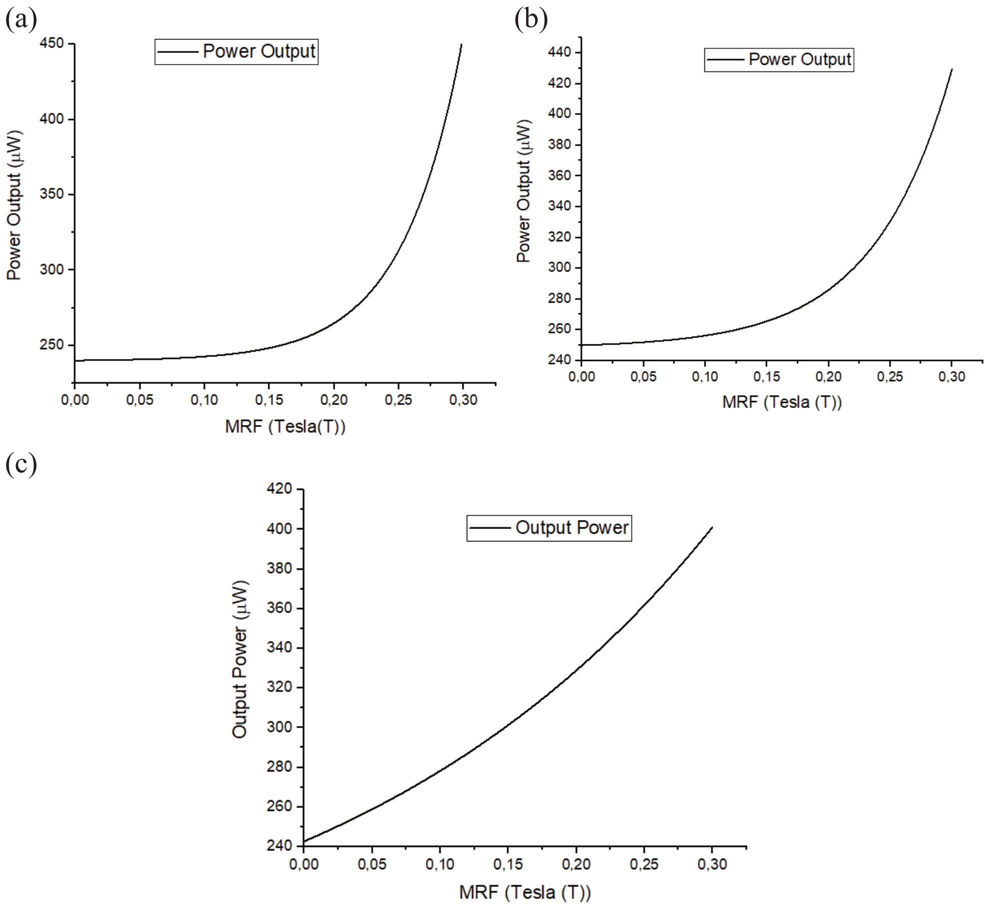


**Figure 3.11.** Comparison of rate of power output against MRF impacting medium: (a) analytical model, (b) COMSOL model and (c) experimental model

**Table 3.3.** Output power results of computed, FEM simulation and experimental models

| **Calculated Resistance** | | | **Power Out-power (μW)** | | | | | | |
|---|---|---|---|---|---|---|---|---|---|
| Experimental | COMSOL Model | Analytical Calculation | Efficiency $eff$ | Experimental | Efficiency $eff$ | COMSOL Model | **Efficiency** $eff$ | **Analytical** | **Magnetic Field (T)** |
| 39.1 | 38.8 | 38.6 | 22% | 239 | 23% | 250 | 22% | 240 | No Field |
| 38.8 | 38.2 | 38.1 | 52% | 287 | 53% | 344 | 53% | 355 | 0.1 |
| 37.2 | 37.2 | 37.5 | 52% | 322 | 53% | **365** | 53% | 370 | 0.2 |
| 36.7 | 37.2 | 37.1 | 54% | 403 | 53% | 405 | 54% | 410 | 0.3 |

Figure 3.11. (a), (b) and (c) shows the comparison graph of the rate of change in the power output with activated MRF, for the analytical, COMSOL and experimental models. These graphs reveal that the power output increases as the field increases.

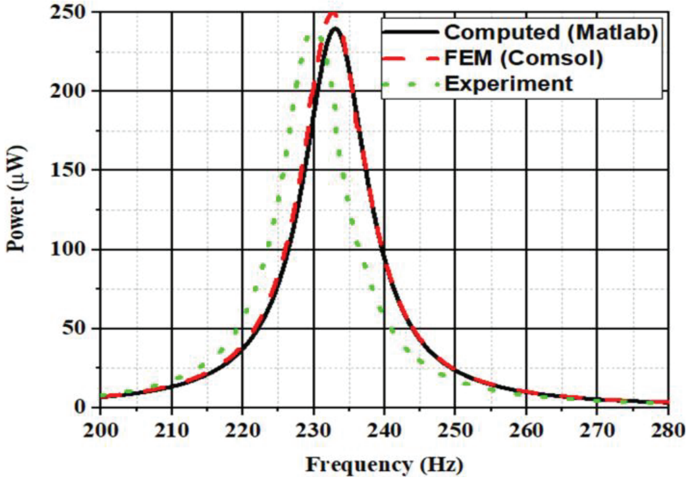


**Figure 3.12.** Output power versus frequency response of the piezoelectric bimorph cantilever beam with no MRF stopper

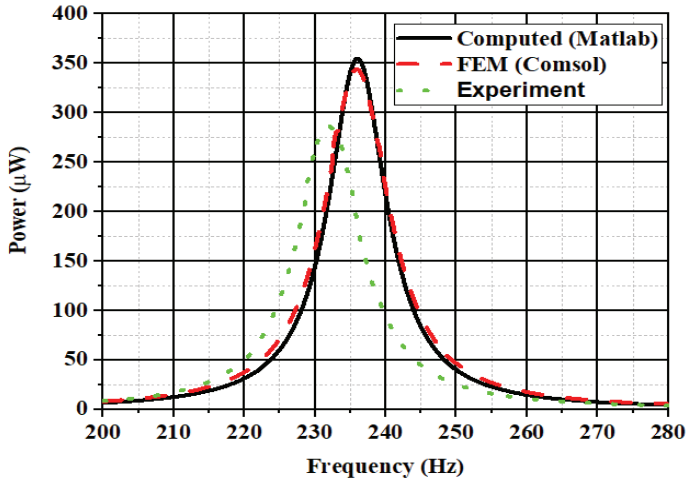


**Figure 3.13.** Output power versus frequency response of the piezoelectric bimorph cantilever beam with MRF stopper at 0.1 T

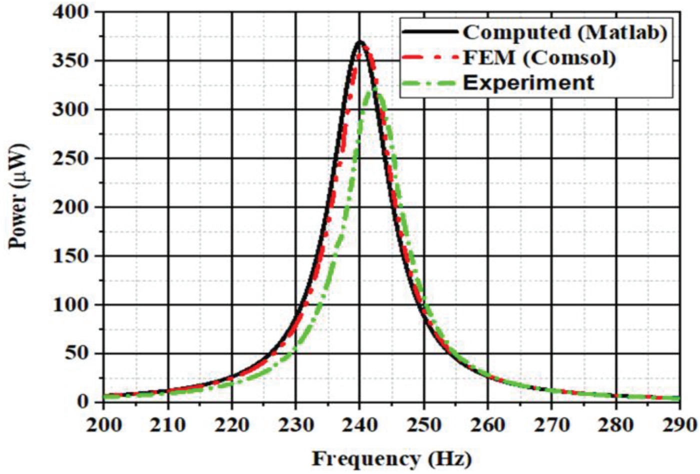


**Figure 3.14.** Output power versus frequency response of the piezoelectric bimorph cantilever beam with MRF stopper at 0.2 T

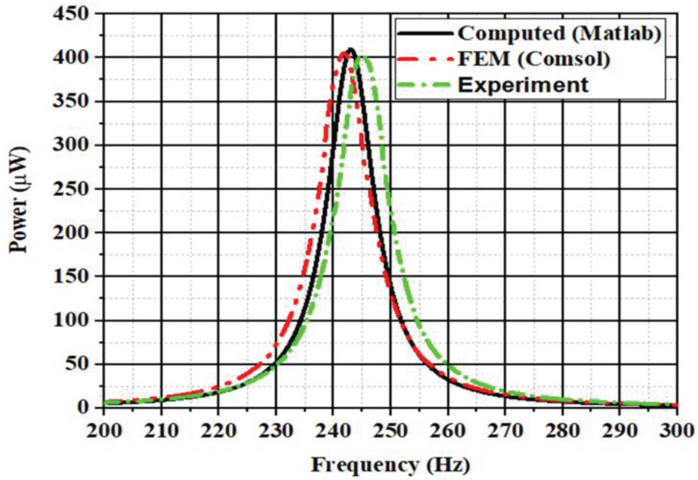


**Figure 3.15.** Output power versus frequency response of the piezoelectric bimorph cantilever beam with MRF stopper at 0.3T

Figure 3.12.,Figure 3.10., Figure **3.14**. andFigure 3.13. show the output power of the analytical, FEM analysis and experimental results.

The output power results that have been obtained in this work correspond to the other results presented for piezoelectric frequency tuning devices. The results reported by [224] have presented a piezoelectric cantilever beam with a natural frequency of 26 Hz used as the energy harvesting cantilever beam, which is successfully tuned over a frequency range of 22–32 Hz to enable a continuous power output 240–280 $\mu W$ over the entire frequency range that is tested.

The efficiency numbers shown in Table 3.3. demonstrated that a higher efficiency for the analytical, COMSOL Model and Experimental models were achieved by using the MRF impacting based medium. The maximum efficiency for the analytical model of the PEG with MRF Impacting Base Frequency Enhancer was improved by 54 % compared to 22 % of the one without MRF impacting medium. The maximum efficiency for the COMSOL Model of the PEG with MRF Impacting Base Frequency Enhancer was improved by 53 % compared to 23 % of the one without MRF impacting medium. The maximum efficiency for the COMSOL Model of the PEG with MRF Impact Base Frequency Enhancer was improved by 54 % compared to 22 % of the one without MRF impacting medium.

### 3.6. Conclusions

This chapter presented a new concept of using MRF as an impacting object for frequency tuning as well as power enhancement for a vibrating piezoelectric bimorph cantilever beam. MRF is a smart fluid that changes from the liquid state to the semi-solid state within milliseconds, when a magnetic field is applied. In the study of this research, the analytical results and FEM simulation results were compared to the experimental results. The FEM simulation was conducted by using COMSOL Multiphysics 5.4 simulation software. The system was modelled as a Single Degree of Freedom (SDOF). There were two sets of results that were presented in the study.

Firstly, the analytical frequency response of the vibrating cantilever beam was tuned at 4 %, as it impacts the activated MRF stopper at 0.3 T magnetic field application compared to the free vibrating cantilever beam without the impact on the MRF stopper. However, the FEM simulation results showed that the frequency was tuned at 3.8 %, as it impacts the activated MRF stopper at 0.3 T magnetic field application compared to the free vibrating cantilever beam without the impact on the MRF stopper. Both results have been validated experimentally. The frequency increased by 6.5 % at 0.3 T magnetic field application in the experimental study. These changes are very significant to a structure like a piezoelectric energy generator.

Secondly, the analytical output power for the vibrating cantilever beam, when it impacted the activated MRF at 0.3 T, gave a maximum power of 410 $\mu W$ and a load resistance of $37k\,\Omega$. However, the FEM results showed a maximum power output of 405 $\mu W$ and a load resistance of 37.2 $k\,\Omega$ for the impacting MRF with 0.3 T magnetic application. The experimental results demonstrated a power output of 403 $\mu W$ at 0.3T and a load resistance of 36.7 $k\,\Omega$.

These results demonstrated that the influence of MRF increases as the magnetic field increases. The MRF changes from liquid to semi-solid state during the application of the magnetic field. The changing of magnetic fields increases the frequency of the beam during the impact on the activated MRF. It was observed that there was a significant amount of power harnessed for the impacting beam. The squeeze mode damping characteristics of the fluid as well demonstrated that significant damping could be achieved in structures using MRF.

# 4. SPHERICAL BRAKE WITH SMART FLUID FOR 3D ROTATIONAL PIEZOELECTRIC DEFLECTOR

## 4.1. Introduction

The properties and characteristics of Smart Fluids that were described in chapter 2 led to exploring the design of SF (MRF and ERF) spherical brake for a 3D Rotational Piezoelectric Deflector. This chapter presents the design of RPD by solving the major problem of the design of this device, which is the deviation in angular positioning due to the moment of inertia of the spherical body. The introduction of SF to the RDF served as a braking medium for precision in angular positioning.

The analytical study of the braking phenomenon was presented as well in this chapter. Through the subsequent execution of the electromagnetic finite element model, created in the COMSOL Multiphysics, it was possible to assess the distribution of the magnetic field inside the MRF more accurately and hence, the resistance to relative motion between hemisphere and stationary disk holding the fluid. The theoretical and experimental results showed a significant improvement in the resolution of the 3D RDP when activated SF was applied. The theoretical calculations show 8 % and 68 % improvements in angular resolution of the 3D RPD for MRF and ERF, respectively. The FEM result as well shows 11 % improvement in the angular resolution of the 3D RPD for MRF. Finally, the experimental results showed 20 % and 56 % improvement in angular resolution of the 3D RPD for MRF and ERF, respectively[7].

## 4.2. Design of 3D RPD utilizing SFs

The prototype of the piezoelectric 3D optical beam deflector is based on the previous research given by [225]. Figure 4.1. andFigure **4.2**. show a prototype of the 3D RPD, which comprises of two parts, i.e., a lead zirconate titanate (PZT)-8 piezoelectric transducer ring with axial polarization and hollow ferromagnetic hemispherical rotor. There are three high frictional contact elements made of friction-proof material glued to the top surface of the piezoelectric transducer ring that has frictional contact with the surface of the hemispherical rotor.

Detailed properties of the PZT-8, hollow ferromagnetic hemispherical rotor and other materials used in 3D PRD are provided in Table 4.1. This type of mechanism is subject to kinematic pair with one active element. The hemispherical rotor could be rotated in three directions around the x, y and z-axis and positioned at the desired angle when the oscillation frequency, amplitude and phase of the piezoelectric ring

---

[7] *This section contains information from the article of the author with the details below: IEEE* Xplore*: 2020 International Conference Mechatronic Systems and Materials (MSM), Controlling the Positioning 3D Rotational Piezoelectric Deflector Using ERF: An Experimental Study, doi:10.1109/MSM49833.2020.9202130.*

transducer change. Nanoscale vibrations of the piezoelectric actuator can be excited by using harmonic voltage.

Piezoelectric deflectors are piezoelectric devices that transform multi-directional resonant oscillations of the piezoelectric transducer into continuous or step motion of the mirror with high accuracy (up to 0.1 μrad) and are used for the precise laser beam steering. The ability to adjust the laser beam pointer is crucial for the optical system. The beam should be able to make rotational movements and set in the angular position. Therefore, different optomechanical elements, including mirrors, are used. The accuracy of the optical system strongly depends on the dynamic characteristics of the deflector [226].

Rotational speed, maximum rotational angle, spatial resolution, stabilization and number of degrees of freedom are the key features of the beam positioning system. There have been developed many different positioning systems of the mirror [227]. The operating principle of these systems can be divided into electro-mechanical and piezoelectric. Most industrial laser optical systems use different types of electrical motors to rotate or move the mirrors. However, the accuracy of such systems is limited to several micrometres.

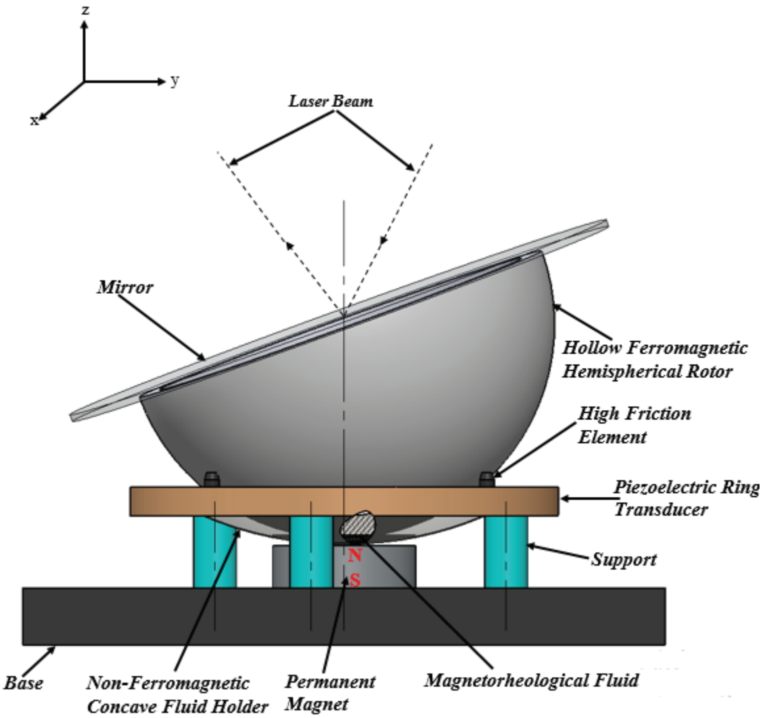


**Figure 4.1.** Principle of the rotational piezoelectric deflector with MRF braking medium

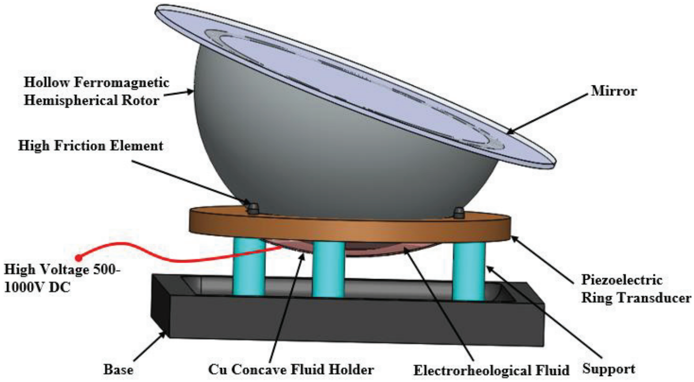


**Figure 4.2.** Principle of 3D rotational piezoelectric deflector (3D RPD) device using ERF as a braking medium

In general, the 3D RPD device requires an actuating component for rotational positioning. Currently, the 3D RPD is driven by a piezoelectric ring transducer, which has some disadvantages. Some of the disadvantages of such a complex mechanism are when the driving actuator is switched off, and due to the inertia, forces of the rotor; it is difficult to maintain a continuous and smooth force control, and precision positioning of the 3D RPD. As a result, the researchers are working on a new actuating spherical braking mechanism based on smart fluids, such as magnetorheological fluids or electrorheological (ERF) fluids. The yield stress of the smart fluids is easily changed by controlling the intensity of the electric or magnetic field. The phenomenological behaviour of the smart fluids has several benefits on the 3D RPD, such as resistance to external forces or pressures, high stability (smooth motion), precision positioning and reliable control performance.

### 4.2.1. Braking analysis of the RPD by using MRF

Figure 4.3. (a) shows a cross-section of the 3D RPD. The $r_s$ is the radius of the hemispherical rotor, $g$ is the height of the MRF filled between the rotor and the ferromagnetic fluid holder, and $r_f$ is the radius of the high friction element. The height between the friction element and the piezoelectric ring transducer is denoted by $h_1$, and the height between the curved part of the rotor, the piezoelectric ring transducer is given by $h_2$. The angles corresponding to the arc portions of the lower rotor to the fluid and the piezoelectric ring transducer are denoted by $\beta_{MRF}$ and $\beta_{pr}$, respectively. In Figure 4.7., the magnetic flux that passes through the fluid holder is according to the magnetic flux conservation law of the magnetic circuit $\Phi = BA$. In order to obtain the ideal force effect, it is necessary to ensure the uniformity of the magnetic flux density applied to the MRF [228]. Therefore, the following equation can be obtained:

$$\int_{\beta_a}^{\beta_s+\beta_a}\int_0^{\alpha_{MRF}}(r+h)^2\sin\beta\, d\alpha\, d\beta = \int_{\beta_s+\beta_a+\beta_{pr}}^{\beta_{MRF}}\int_0^{\alpha_{MRF}}(r+h)^2\sin\beta\, d\alpha\, d\beta = \cos(\beta_s+\beta_a)+\cos\left(\beta_s+\beta_a+\beta_{pr}\right)-\cos(\beta_{MRF}) = \cos\beta_s. \tag{4.1}$$

Based on Fig. 4.3. (b), the following dependencies are obtained:

$$\sin \beta_s = \frac{r_f}{r_s + g}, \tag{4.2}$$

$$\beta_s + \beta_a + \beta_{pr} = \beta_{MRF}, \tag{4.3}$$

$$h_1 = (r_s + g)(\cos \beta_s - \cos(\beta_s + \beta_a)), \tag{4.4}$$

$$h_2 = (r_s + g)\big(\cos(\beta_s + \beta_a) - \cos\big(\beta_s + \beta_a + \beta_{pr}\big)\big). \tag{4.5}$$

When an external magnetic field is applied to the MRF, the rheological properties such as viscosity changes. In the absences of the magnetic field, the fluid returns to the liquid state behaving as Newtonian [229] and can be described as:

$$\tau = \mu\dot{\gamma}; \tag{4.6}$$

where $\tau$ is the shear stress, $\mu$ is the viscosity of the fluid, and $\dot{\gamma}$ is the shear rate. The MRF torque braking is given as:

$$\dot{\gamma} = \frac{\omega \times r}{g}; \tag{4.7}$$

where $r$ is the rotor radius, ω and $g$ are the angular speed and the MRF gap length, respectively.

When the magnetic field is applied to MRF, the rheological properties of the fluid are altered. The magnetic particles in the carrier fluid induce polarization and form chain-like structures in magnetic flux path direction, thus changing the viscosity of the fluid. The behaviour of the fluid is often represented as a non-Newtonian [230], having a variable yield strength. Bingham's model is described as [231]:

$$\tau = \tau_B + \mu\dot{\gamma}; \tag{4.8}$$

where $\tau_B$ is the yield stress, which is developed in response to the applied magnetic field. Its value is a function of the magnetic field induction B.

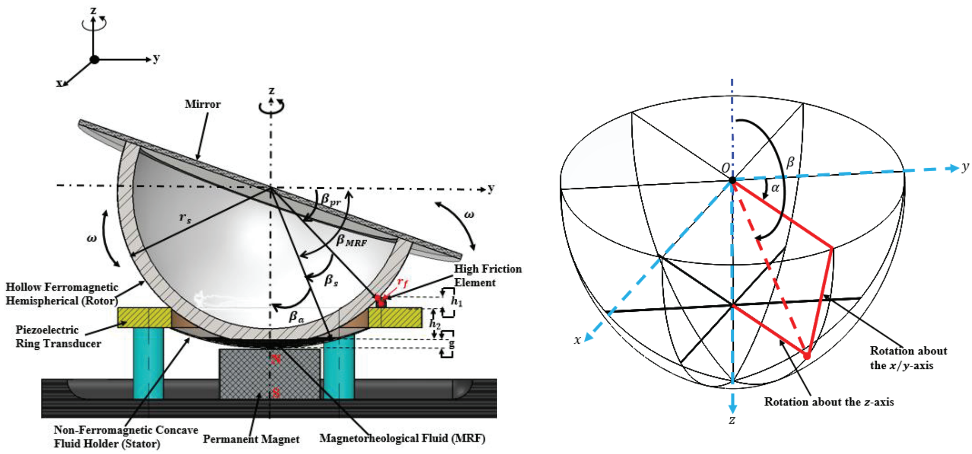

(a) (b)

**Figure 4.4.** a) Scheme of the proposed 3D RPD, b) spherical coordinate system for the torque model

Therefore, the output torque $T_{output}$ generated by the hemispherical rotor is given as:

$$T_{output} = T_\tau + T_\mu + T_\eta; \tag{4.9}$$

where $T_\eta$ is the mechanical friction, and $T_\tau$ is the controllable torque given as:

$$T_\tau = \int_{A_s} r_r \tau_y(B)\, dA_s. \tag{4.10}$$

$T_\mu$ is the viscous torque given as:

$$T_\mu = \int_{A_s} r_r \mu \dot{\gamma}\, dA_s; \tag{4.11}$$

where $A_s$ denotes the surface area of the sphere that is activated by the magnetic field, $r_r$ is the moment arm, which is the distance from the point on the surface of the sphere to the axis of rotation. In the application, the rotational speed of the 3D RPD is slower; therefore, the $T_\mu$ is proportional to the angular velocity, and this is negligible.

The maximal torque rotation of the rotor on the three axes has to be formulated and calculated with and without the MRF application. The torque model of the three coordinates system of the hemispherical rotor is represented in Figure 4.4. (b).

From Figure 4.4. (a), the rotation angles $\gamma$ and $\beta$ are formulated based on the point location on the hemispherical surface. The angle of rotation of the rotor on the 3 axes is given as:

$$r_r{}^x = r \sin\beta, \tag{4.12}$$

$$r_r{}^x = r_r{}^y = r\sqrt{(\cos\beta)^2 + (\sin\alpha \sin\beta)^2}. \tag{4.13}$$

Based on the equations 4.12 and 4.13, the torque output at the z-axis is given as:

$$T_{output}{}^z \approx T_\tau{}^z = \int_0^{\beta_0}\int_0^{\alpha_0} T_\tau r^3 (\sin\beta)^2 d\alpha d\beta == T_\tau r^3 \alpha_0 \left(\frac{\beta_0}{2} - \frac{\sin 2\beta_0}{4}\right); \tag{4.14}$$

where $\alpha_0$ and $\beta_0$ are the angles of the stator.

Based on the equations 4.10 and 4.13, the output torque in the $x$ and $y$ axis is given as:

$$T_{output}{}^x = T_{output}{}^y \approx T_\tau{}^{x\ or\ y} =\approx T_\tau{}^z(\beta_0 = \pi) -$$

$$\int_0^{\pi-\beta_0}\int_0^{\alpha_0} T_y r^3 \sin\beta\sqrt{(\cos\beta)^2 + (\sin\alpha\sin\beta)^2}\, d\alpha d\beta\ . \tag{4.15}$$

The equations 4.14 and 4.15 describe the dependence of the yield stress $\tau_y$ of the MRF 140-CG developed by the Lord Corporation [82]. That work has shown that the torque output increases when the yield stress of the MRF increases. In this study, the MRF-140CG was used. This type of MRF has a yield strength that is highly saturated. With the increase of magnetic flux density, the yield stress of MR fluid increases approximately linearly and tends to saturate when the magnetic flux density reaches 1T. An approximate polynomial of the dynamic yield stress $\tau_y(B)$ can be obtained from the least-squares curve-fitting method, which is expressed as:

$$\tau_y(B) = -66.434B^3 + 99.911B^2 + 24.188B + 0.6812. \tag{4.16}$$

### 4.2.2. Design of the magnetic circuit

The magnetic circuit generates an appropriate magnetic field in the MRF, which is important for the 3D RPD in motion. The magnetic circuit analysis was conducted based on the following criteria introduced in [232]. The Ampere's circuital law, the circulation of magnetic field intensity (H) around the closed path (C), which is equal to the free current (I), and the surface bounded by the path are related as:

$$\oint_C H.dI = I. \tag{4.17}$$

The equation 4.17 that is given in a closed loop can be rewritten as:

$$H_a I_a + H_f I_f + H_{MRF} I_{MRF} + H_m I_m = 0; \tag{4.18}$$

where $I_a, I_f, I_{MRF}$ and $I_m$ are the cumulative lengths of the air, the ferromagnetic material, the MRF, and the permanent magnet along the path, respectively. $H_a$, $H_f$, $H_{MRF}$ and $H_m$ are the average magnetic field intensities along the path lines in these materials. When the flux leakage is neglected, the relation that is established follows the continuity of the magnetic flux given as:

$$\Phi = A_a B_a = A_f B_f = A_{MRF} B_{MRF} = A_m B_m; \tag{4.19}$$

where $\Phi$ is the magnetic flux, $A_a$, $A_f$, $A_{MRF}$ and $A_m$ are the cross-sectional areas of the materials along the magnetic circuit, and $B_a$, $B_f$ , $B_{MRF}$ and $B_m$ are the average magnetic flux densities over these cross-sectional areas. Assuming that the magnetic properties of the materials are linear:

$$\frac{B_a}{\mu_a H_a} = \frac{B_f}{\mu_f H_f} = \frac{B_{MRF}}{\mu_{MRF} H_{MRF}} = \mu_o; \tag{4.20}$$

where $\mu_a$, $\mu_f$ and $\mu_{MRF}$ are the relative permeability of the air, the ferromagnetic material, and the MRF, respectively, and where $\mu_o$ is the permeability of the vacuum. Moreover, Br is the remnant flux density, and $H_c$ is the coercive field intensity. For convenience, the demagnetization curve can be approximately described as:

$$B = \frac{B_r}{H_c} H + B_r. \tag{4.21}$$

Combining the equations 4.18 and 4.21, the average magnetic field intensity at the MRF can be expressed as:

$$H_{MRF} = \frac{A_m l_m B_r}{\mu_0 \mu_{MRF} A_{MRF}\left(l_m + D\frac{B_r}{H_c} A_m\right)}; \tag{4.22}$$

where

$$D = \frac{l_a}{\mu_a \mu_0 A_a} + \frac{l_f}{\mu_f \mu_0 A_f} + \frac{l_{MRF}}{\mu_{MRF} \mu_0 A_{MRF}}. \tag{4.23}$$

The equation 4.22 shows that in order to increase the magnetic field intensity at the MRF, the magnetic path length of the air ($l_a$), the ferromagnetic material ($l_f$) and the MRF ($l_{MRF}$) have to be decreased, when all other variables are fixed. As the relative permeability of ferromagnetic materials is much larger than that of the air and the MRF, decreasing the length of air and the MRF will be much more effective than decreasing that of the ferromagnetic material.

### 4.2.3. The equations of motion of ERF

The ideal Bingham theory defines the behaviour of the smart fluids as a solid, until the yield stress $\tau_y$ is exceeded and exhibits a linear relationship between the stress and the rate of shear or deformation. However, the yield stress is a function of the applied field. As the applied field increases, the yield stress increases as well. In Annexe 5, the graph shows the change in the yield stress and apparent viscosity by changing the applied field.

From the experiment conducted by [233], it was found that the yield shear stress for the ERF varies concerning the electric field. The results showed that the relation between the yield shear stress $\tau_0$ and the electric field strength $E$ is given as follows:

$$\tau_{\mathrm{y}}(E) = \alpha \left(\frac{U}{2h}\right)^{\beta}; \tag{4.24}$$

where $E$ is the magnitude of the vector $E$, but $U$ and $2h$ are the applied voltage and the film thickness, respectively. Both parameters $\alpha$ and $\beta$ are the experimental constants, of which the range of the exponent $\beta$ is from 1 to 2.4 [234, 235]. The shear yield stress ($\tau_{\mathrm{y}}(E)$) is as well written as shown in the equation 2, based on the experimental data presented by [236]:

$$\tau_{\mathrm{y}}(E) = \alpha_1 \left(\frac{U}{2h}\right) + \alpha_2 \left(\frac{U}{2h}\right)^{\beta}; \tag{4.25}$$

where $\alpha_1$ and $\alpha_2$ are constants. For relatively high field strengths, a simpler formula may be used:

$$\tau_{\mathrm{y}}(E) = \alpha \left(\frac{U}{2h}\right)^{2}; \tag{4.26}$$

where $\alpha$ is an experimental constant.

### 4.2.4. Torque modelling for ERF braking medium

The torque generated by the activated ERF hemispherical 3D RPD is affected by the viscous friction torque $T_\mu$ and the controllable torque $T_{ERF}$. This is given as:

$$T_\mu = \iint_{S_h} \mu \dot{\gamma} r_r dA, \tag{4.27}$$

$$T_{ERF} = \iint_{s_h} \tau_y r_r dA, \tag{4.28}$$

where $s_h$ is the surface area of the hemispherical rotor. $r_r$ is the distance of the rotation arm from one point on the hemispherical rotor surface to the rotational axis.

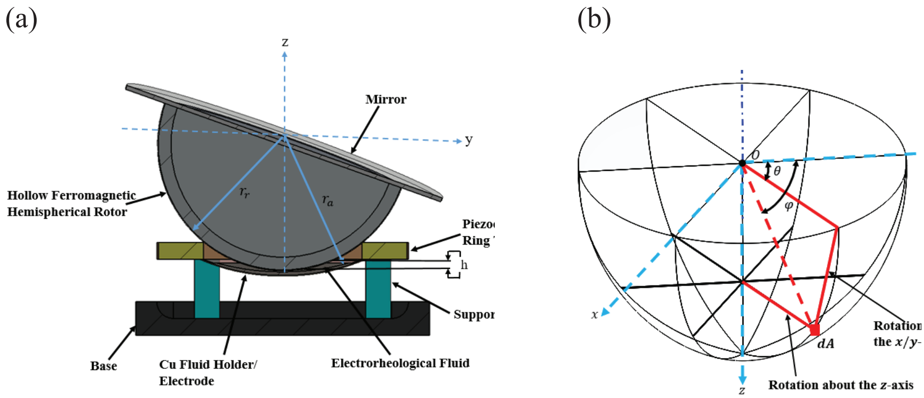


**Figure 4.5.** a) Scheme of the proposed 3D RPD, b) spherical coordinate system for the torque model

The rotation of the rotor about the three coordinates is shown in Figure 4.5. (b). An arbitrary point on the surface of the electrode is described by the angles $\varphi$ and $\theta$. The moment arm for X, Y and Z axis is determined by:

$$X_{r_m} = r_a\sqrt{(\sin\theta)^2 + (\cos\theta\sin\varphi)^2}, \tag{4.29}$$

$$Y_{r_m} = r_a\sqrt{(\sin\theta)^2 + (\cos\theta\sin\varphi)^2}, \tag{4.30}$$

$$Y_{r_m} = r_a\cos\theta, \tag{4.31}$$

where $r_a$ is the radius of the spherical joint. The generated controllable torque, viscous friction torque in three rotational motions have derived by surface integral as follows:

$$X_{T_{ERF}} = \tau_y(E) r_a^3 \pi^2 - \int_0^{\frac{\pi}{2}-\theta_0}\int_0^{2\pi} \tau_y(E) r_a^3 \sqrt{(\sin\theta)^2 + (\cos\theta\sin\varphi)^2}\,\cos\theta d\varphi d\theta, \tag{4.32}$$

$$Y_{T_{ERF}} = \tau_y(E) r_a^3 \pi^2 \neg \int_0^{\frac{\pi}{2}-\theta_0}\int_0^{2\pi} \tau_y(E) r_a^3 \sqrt{(\sin\theta)^2 + (\cos\theta\sin\varphi)^2}\,\cos\theta d\varphi d\theta, \tag{4.33}$$

$$Z_{T_{ERF}} = \int_{-\frac{\pi}{2}}^{\theta_0}\int_0^{2\pi} \tau_y(E) r_a^3 \cos^2\theta d\varphi d\theta, \tag{4.34}$$

$$X_{T_\mu} = \mu\frac{8\pi\omega}{3h}r_a^4\pi^2 \neg \int_0^{\frac{\pi}{2}-\theta_0}\int_0^{2\pi}\mu\frac{\omega}{h}r_a^4\sqrt{(\sin\theta)^2+(\cos\theta\sin\varphi)^2}\cos^2\theta d\varphi d\theta, \quad (4.35)$$

$$Y_{T_\mu} = \mu\frac{8\pi\omega}{3h}r_a^4\pi^2 \neg \int_0^{\frac{\pi}{2}-\theta_0}\int_0^{2\pi}\mu\frac{\omega}{h}r_a^4\sqrt{(\sin\theta)^2+(\cos\theta\sin\varphi)^2}\cos^2\theta d\varphi d\theta, \quad (4.36)$$

$$Z_{T_\mu} = \int_{-\frac{\pi}{2}}^{\theta_0}\int_0^{2\pi}\mu\frac{\omega}{h}r_a^4\cos^3\theta d\varphi d\theta, \quad (4.37)$$

where $\omega$ is the angular velocity of the rotor, and $h$ is the fluid thickness. $\theta_0$ is the constant angle of the electrode

### 4.3. FEM simulation

In order to design a high-performance 3D RPD, three main factors are considered. These factors are structural design, excitation design and dynamic characteristics. This section focuses on the experimental analysis, theoretical and finite-element method to optimize the structure of the 3D RPD. Since the geometry of a single magnetic circuit unit in the 3D RPD is not symmetric about the z-axis, in this section, the finite element simulation was performed with COMSOL 5.4a Multiphysics [237], where electromagnetic modules were used. As a basis for a time-dependent solver, the relations defined by Maxwell's equations were employed, including the equation of continuity for constant electric charge density; the Comsol 5.4 software is employed to perform three-dimensional (3-D) finite-element analysis (FEA) of the magnetic circuit. Before using FEA to optimize the structure, some design specifications of the 3D RPD were specified.

In order to design the 3D RPD electromagnetic FE model, these dependencies were used in the Comsol Multiphysics software:

$$\nabla \times J = 0\,, \quad (4.38)$$

and Ampere's law,

$$\nabla \times H = J. \quad (4.39)$$

There, H is the magnetic field intensity and J the current density. The constitutive relations are established between the magnetic field intensity and magnetic flux density, B:

$$\mathrm{B} = \mu_0 \times \mu_r \times H, \quad (4.40)$$

and between current density and electric field intensity, E:

$$\mathrm{J} = \sigma E \times J_e. \quad (4.41)$$

In these equations, $\mu_r$ and $\mu_0$ are the material permeability and the permeability of free space, respectively, and σ is the electrical conductivity. The two potentials are described as direct consequences of Gauss's law:

$$E = -\nabla V, \quad (4.42)$$

and Faraday's law,

$$B = \nabla \times \mathrm{A}; \quad (4.43)$$

where $V$ is the electric scalar potential and A is the magnetic vector potential. Finally, the $J_e$ term from the equation 4.41 was generated with COMSOL's multi-turn coil domain interface, the value representing the external contribution of the electromagnetic coil to the ambient current density:

$$J_e = \frac{N_{coil} \times I_{coil}}{A} \times \phi. \quad (4.44)$$

There, $N_{coil}$ is the number of turns in the electromagnetic coil, and $I_{coil}$ is the applied current. In order to simulate the behaviour of the magnetorheological fluid, a direct relationship was defined between the fluid's dynamic viscosity and the intensity of the local magnetic field. This viscosity regularization and the general fluid flow dynamics of the model are discussed in detail in the following section.

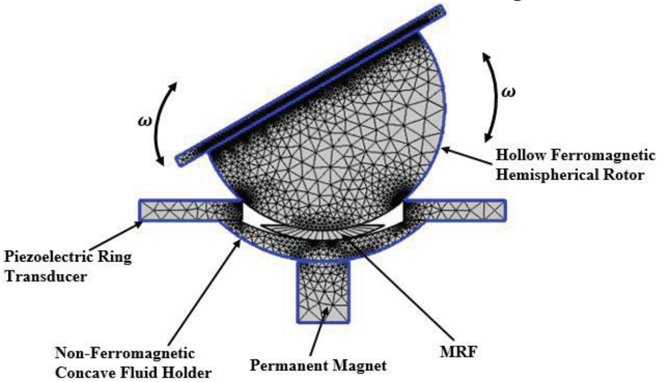


**Figure 4.6.** Mesh model of the asymmetric RPD using MR3

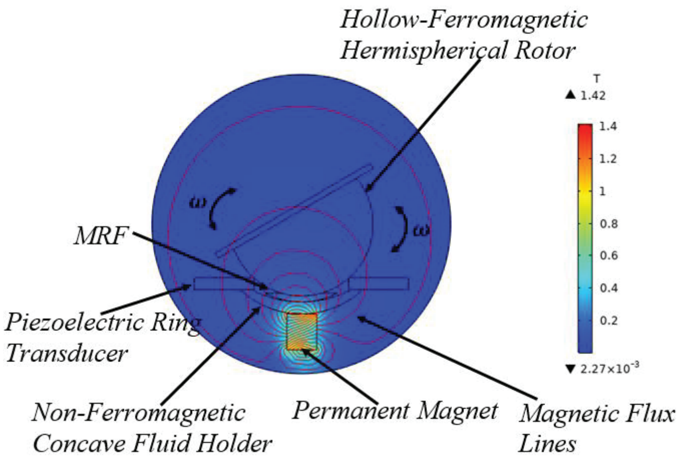


**Figure 4.7.** Distribution of the magnetic flux density

The simulation mesh model is presented in Figure 4.6., where the defined meshed asymmetrical geometry of the RPD model, due to the complexity of the model, the entire system is given as well. In order to perform the electromagnetic analysis, the materials were defined: namely, steel for the hemispherical body, glass for the deflector, iron for the electromagnetic coil and magnetorheological fluid. After the definition of the materials, it is possible to get the magnetic flux density field characteristics at two different initial inputs, i.e., angular speed of the RPD and the magnetic flux. Figure 4.7. gives the magnetic flux density.

### 4.4. Experimental analysis

In this section, the experimental investigation of the effects of MRF and ERF on the positioning of 3D RPD was demonstrated. The experimental results compared the difference in the resolution of the 3D RPD, when there is a fluid applied as a breaking media and when the fluid is not applied. The experimental setup presented in Figure 4.8. and Figure **4.9**. shows a prototype of the 3D RPD with MRF and ERF setup, respectively. The angular displacement results were obtained through the excitation of the piezoelectric transducer ring. The produced signal was a burst-type harmonic vibration signal of 22 cycles that is repeated at every 0.5 s. The operational frequency generated from the Agilent 33220 A and linear amplifier EPA-104 was set at 32.5 kHz. The results compared the cases where there was no Smart fluid present and where an activated SF was present.

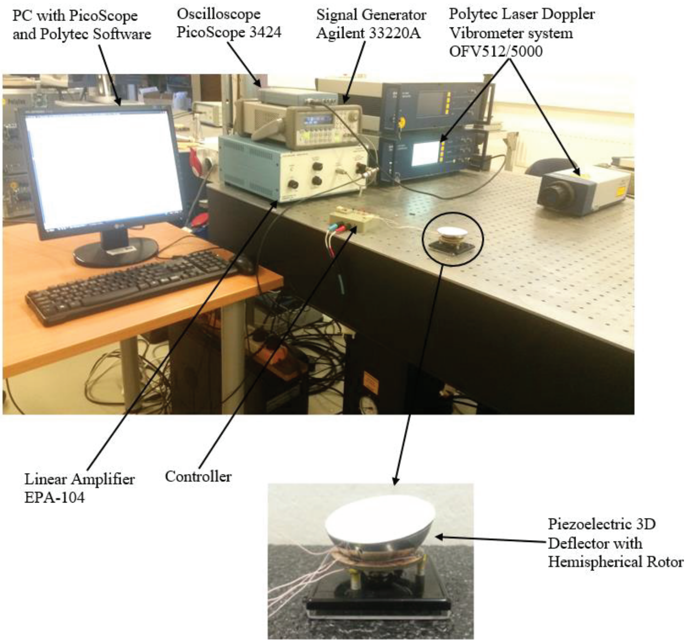


**Figure 4.8.** Experimental setup of the RPD using MRF as a braking medium

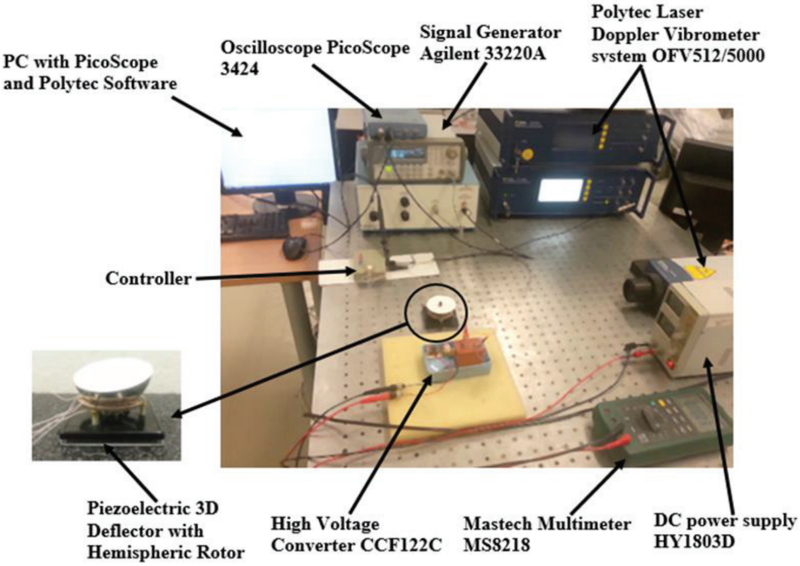


**Figure 4.9.** Experimental setup of the 3D RPD using ERF as a braking medium

**Table 4.1.** Design parameters of the 3D RPD

| **Description** | **Symbol** | **Value** |
|---|---|---|
| **Radius of sphere** | R | 15 mm |
| **Piezoelectric ring thickness** | $t_p$ | 6 mm |
| **Piezoelectric ring inner diameter** | $P_{id}$ | 19.5 mm |
| **Piezoelectric ring outer diameter** | $P_{od}$ | 30 mm |
| **Radius of non-ferromagnetic concave fluid holder** | $r_{SD}$ | 23 mm |
| **Inner radius of the magnet ring** | $M_{ir}$ | 4.2 mm |
| **Outer radius of the magnet ring** | $M_{or}$ | 12 mm |
| **Magnet thickness** | $t_m$ | 8 mm (+/-0.1 mm) |
| **Thickness of MRF/ERF** | H | 0.5 mm |
| **Magnetic field** | Bf.max | 0.4 T |
| **Magnetic permeability of the vacuum** | $\mu$ | 4 π 10-7 N/A2 |
| **Remnant flux density of magnet** | Br | 1.28T |
| **Coercivity field intensity of magnet** | Hc | 955 kA/m |
| **Applied voltage** | $\boldsymbol{V}$ | **800 V** |

This electric field applied to the ERF was achieved due to the fluid thickness $h$ as shown in Figure 4.5. and the applied voltage, which in this case is 800 V. The electric field is obtained from the equation 4.25. The ERF that is used in this experiment is LID 3354s, the properties of which can be found in Table 1. in Annexe

3 [163]. The trajectory of the 3D RPD was measured by using Polytec laser doppler vibrometer OFV512/5000.

### 4.5. Results and discussion

The graphs shown in Figure 4.10. (a) and (b) reveal the theoretical results conducted in Matlab and the experimental results of the angular displacement when the resolution of one-step without MRF applied. The rotation of the hemispherical rotor is about 40 $\mu rad$ at a transient time of about 350 ms for the 3D RPD without MRF for the calculated model, and the angular step amplitude is about 25 $\mu rad$, and the transient time is about 100 ms for the experimental model without MRF applied. The graphs that are shown in Figure 4.11. (a) and (b) are the FEM COMSOL simulated and experimental results of the 3D RPD without MRF application. The angular displacement of the 3D RPD without the application of MRF, at a resolution of one step for the simulated model, is about 38 $\mu rad$, and a transient time is about 750 ms.

However, Figure 4.12. (a) and (b) shows the results of the angular rotor displacement responses to the sinusoidal burst type input voltage signal with the amplitude of 70 V (peak to peak) and frequency of 32.5 kHz. The angular displacement of it is about 37 $\mu rad$ at a transient time of about 340 ms for the 3D RPD with the activated MRF for the calculated model and the angular step of 20 $\mu rad$ and the transient time of 230 ms for the experimental model with activated MRF. Figure 4.13. (a) shows the angular displacement of the 3D RPD when the activated MRF is applied for the simulated model, where the resolution of one-step is shown on the graph to be 34 $\mu rad$ at a transient time of 740 ms, and Figure 4.13. (b) reveals the angular displacement of the experimental model with the activated MRF.

The theoretical and experimental results showed a significant improvement in the resolution of the 3D RDP when activated MRF is applied. The theoretical calculations show 8 % improvement in the angular resolution of the 3D RPD. The FEM result as well shows 11 % improvement in the angular resolution of the 3D RPD. Finally, the experimental results showed 20 % improvement in the angular resolution of the 3D RPD.

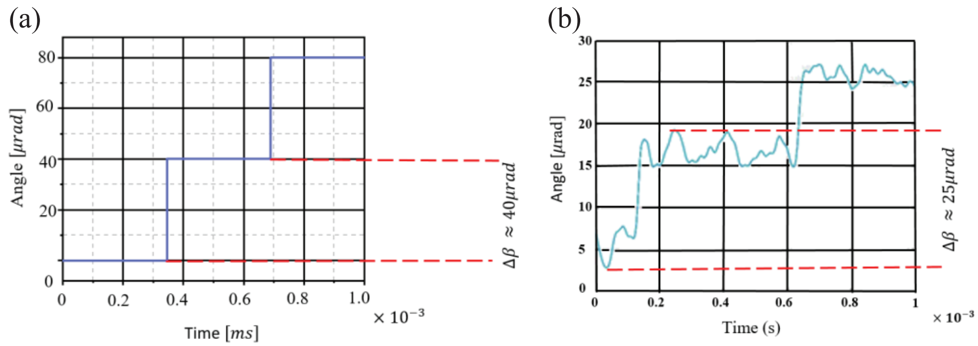


**Figure 4.10.** (a) Calculated results of rotor step angular displacement as a function of time without MRF application, and (b) experimental results of rotor step angular displacement as a function of time without MRF application

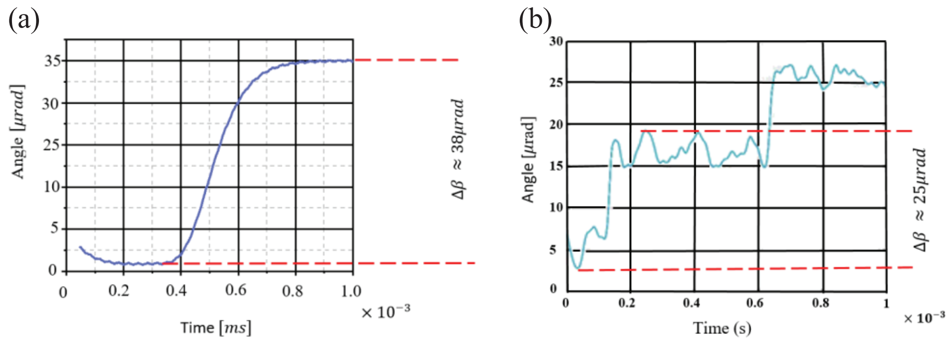


**Figure 4.11.** (a) FEM results of rotor step angular displacement as a function of time without MRF application and (b) experimental results of rotor step angular displacement as a function of time without MRF application

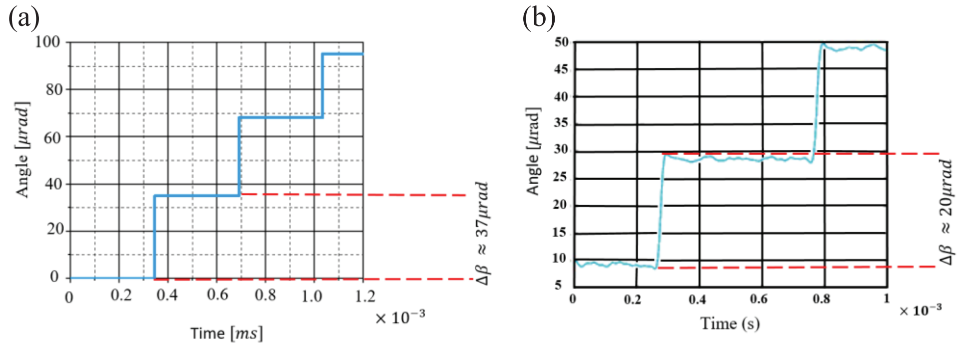


**Figure 4.12.** (a) Calculated results of rotor step angular displacement as a function of time with activated MRF and (b) experimental results of rotor step angular displacement as a function of time with activated MRF

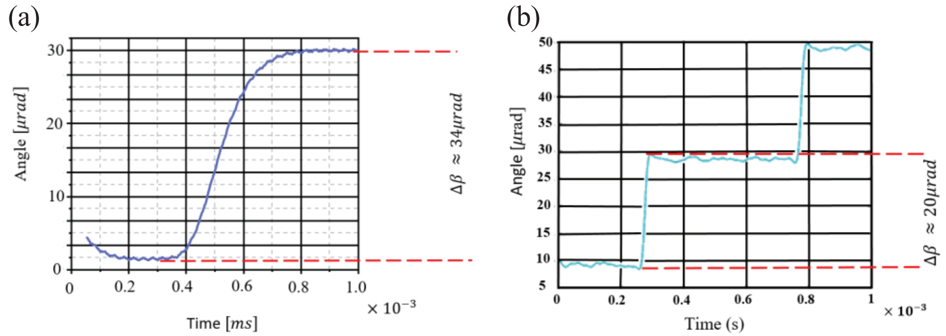


**Figure 4.13.** (a) FEM results of rotor step angular displacement as a function of time with activated MRF and (b) experimental results of rotor step angular displacement as a function of time with activated MRF

(a) (b)

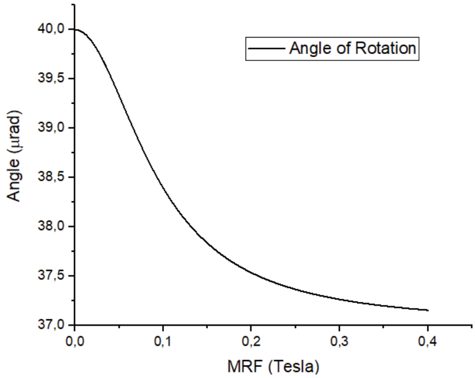


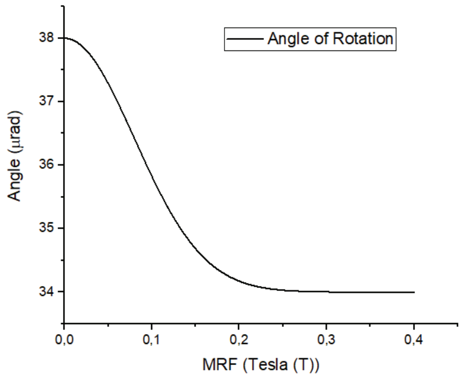


(c)

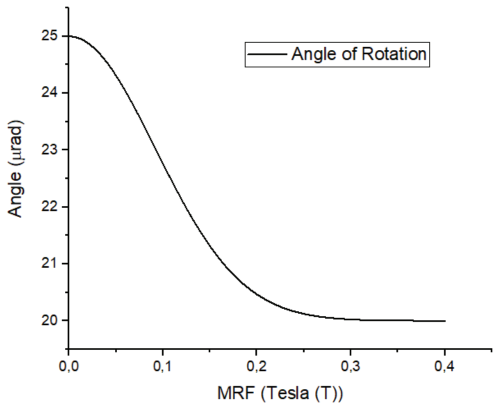


**Figure 4.14.** Comparison of rate of angle of rotation for MRF (a) analytical model, (b) COMSOL model and (c) experimental model

Figure 4.14. (a), (b) and (c) shows the comparison graph of the rate of change in the angle of rotation of 3D RPD with activated MRF for the analytical, COMSOL and experimental models, respectively. These graphs show that the angular rotation decreases, as the applied field to the MRF increases

The graphs shown in Figure 4.15. (a) and (b) are the theoretical results conducted in Matlab and the experimental results. The angular displacement: the resolution of one-step is at 85 $\mu$ rad at a transient time of 49 ms for the RPD without ERF braking medium for the theoretical model, and a resolution of one-step is about 90 $\mu rad$ at a transient time of 80 ms for the experimental model.

The graphs that are shown in Figure 4.16. (a) and (b) are the theoretical and experimental results of the angular displacement of the 3D RPD with ERF applied. The graph shows a resolution of one-step of 27 $\mu$ rad at a transient time of about 38 ms and a resolution of one-step at 40 μrad at a transient time of 38 ms for the experimental model.

The theoretical and experimental results showed a significant improvement in the resolution of the 3D RDP when activated ERF is applied. The theoretical calculations show 68 % improvement in the angular resolution of the 3D RPD. However, the experimental results showed 56 % improvement in angular resolution of the 3D RPD.

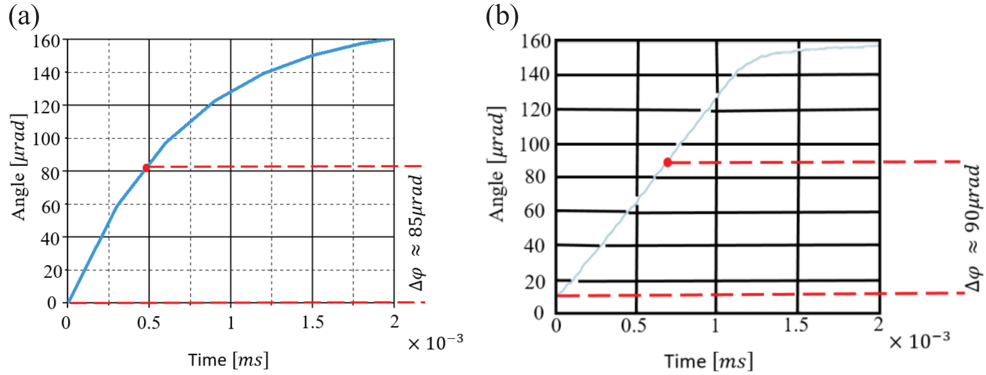


**Figure 4.15.** (a) Theoretical results with angular rotation without ERF applied and (b) experimental results with angular rotation without ERF applied

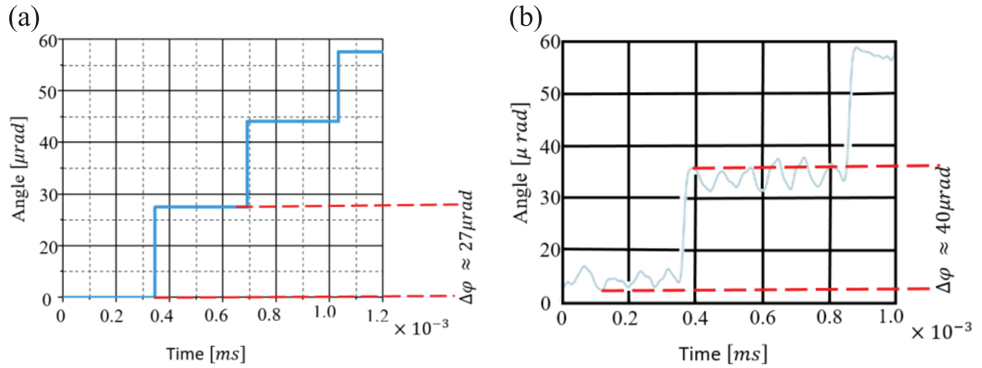


**Figure 4.16.** (a) Theoretical angular rotation with the activated ERF and (b) experimental results with the activated ERF

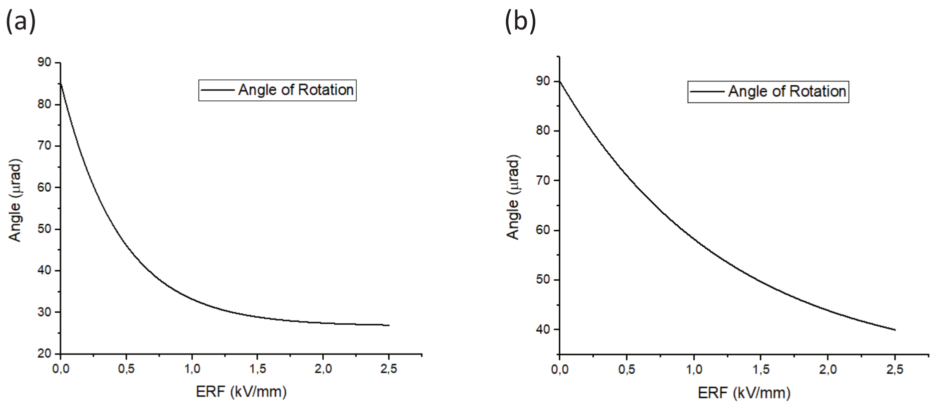


**Figure 4.17.** Comparison of rate of angle of rotation for ERF (a) analytical model, (b) experimental model

Figure 4.17. (a) and (b) shows the comparison graph of the rate of change in the angle of rotation of 3D RPD with activated ERF for the analytical and experimental models. These graphs show that the angular rotation decreases as the applied field to the ERF increases.

### 4.6. Conclusions

In this research, the MRF was proposed to design a brake for the RPD. The main part of the RPD consists of a hemispherical hollow body, a spherical fluid holder or disc, a permanent magnet that holds the RPD in place. The gap between the hemispherical body and the disc is filled with MRF. This created the necessary magnetic circuit for the proper magnetization of the fluid and the required braking torque. The preliminary configuration of brake fluid is obtained by the evaluation of the main factors influencing the design of the magnetic circuit and the performance obtained in terms of brake torque. Through the subsequent realization of a finite element magnetic flux density model, it was possible to assess the distribution of the magnetic field inside the MRF and the resistance to relative motion between the hemispherical body and the disc more accurately. However, it is possible in the next analysis of FEM model results to compare the calculated results to the actual experimental results.

The theoretical and experimental results showed a significant improvement in the resolution of the 3D RDP when activated MRF is applied. The theoretical calculations show 8 % improvement in the angular resolution of the 3D RPD. The FEM result as well shows 11 % improvement in the angular resolution of the 3D RPD. Finally, the experimental results showed 20 % improvement in the angular resolution of the 3D RPD.

The other design introduced another novel form of controlling the 3D RPD to achieve that precision positioning of the 3D RPD by using an activated ERF. The theoretical and experimental results using shear forces were created by activated ERF as a controlling medium for the 3D RPD. The theoretical results show 68 %

improvement in the resolution steps of the 3D RPD when ERF is applied compared to the one without ERF. The experimental results show 56 % improvement in the resolution steps of the 3D RPD when ERF is applied, comparing to the one without ERF. However, these results show that by applying ERF to the 3D RPD can significantly reduce the slip of the rotor and improve its positioning.

## CONCLUSIONS

The research work that was conducted within the scope of this dissertation was aimed at providing theoretical and experimental studies for using SF to improve the functionality of a cantilever beam used in resonant sensors, enhancing the output power of a piezoelectric generator and serving as a braking medium for 3D Rotational Piezoelectric Deflector. The outcome and conclusions can be summarized by highlighting the following points:

1. The evaluation of the rheological properties of smart fluids makes them a good choice as a material to help improve the functionalities in mechatronic devices. A resonant sensor was designed by using sandwiched SF cantilevers that did not achieve the needed damping effects, when the field is applied to the fluid. It has been found that the use of a solid object as frequency tuner for piezoelectric energy generators was not effective enough in terms of damages caused to the cantilever beam when vibrating. The 3D Rotational Piezoelectric Deflector has some limitations in the precision of angular positioning when it brakes.
2. The analysis of simulation, the analytical and experimental results of CB with ERF as damping medium at 1.6 kV/mm, 1.8 kV/mm and 2kV/mm for a vibrating CB shows that the stiffness and damping characteristics of the CB were controlled. An increase of frequency and a decrease of amplitude were obtained by comparing to non-activated ERF. The maximum increase of the frequency of CB was at 2kV/mm: in the experimental results, 12.4 %, in the simulation and the analytical results, 16.2 % and 13.46 %, respectively.
3. A new method of using rheological change in MRF as a soft impacting medium for frequency tuner for PEG was created. The results showed an increase in the frequency and power output of the PEG when MRF is activated, compared to the free vibrating beam without the presence of the MRF medium. The maximum power output results for analytical, simulation and experimental investigation, when the MRF was activated at 0.3T, were $410\ \mu W$, $405\ \mu W$ and $403\ \mu W$, respectively, compared to the one without the presence of MRF, the results were $240\ \mu W$, $250\ \mu W$ and $239\ \mu W$ respectively.
4. A theoretical and experimental study of the ERF and MRF as a braking medium for 3D Rotational Piezoelectric Deflector shows a higher precision of angular positioning of the 3D RPD, compared to them without the presence of the braking medium. The theoretical, simulation and experimental results, when MRF is applied, show 8 %, 11 %, and 20 % higher angular resolution of the 3D RPD, compared to the one without the presence of the MRF braking medium. The theoretical and experimental results of 3D RPD when ERF is applied show 68 % and 56 % higher angular resolution, compared to the one without the presence of the ERF braking medium.

**ACKNOWLEDGEMENTS**

Firstly, the author of the dissertation would like to express his sincere gratitude to the supervisor Prof. Dr. Egidijus Dragašius for his support and guidance on writing this dissertation and helping to begin PhD journey in Kaunas, Lithuania.

Secondly, the author of the dissertation is grateful to Prof. Dr Vytautas Jūrėnas for his support and guidance through all the experimental work and technical advices over the years.

The author of the dissertation would like to indicate his appreciation to the reviewers from the department and the faculty: Prof. Dr. Giedrius Janušas, Assoc. Prof. Dr. Saulius Baskutis and Dr. Darius Mažeika for their valuable criticism.

In addition to the supervisor and reviewers from the department, the author of the dissertation would like to thank the Head of the PhD Prof. Dr. Vytautas Ostaševičius and the entire PhD committee members for their insightful comments and criticism during 4 years of study in KTU.

The author of the dissertation would like to sincerely thank Assoc. Prof. Dr. Martin Agelin-Chaab from the Ontario Technical University, Oshawa, Canada, for his support during the author's research in Canada and for his advices during the process of writing articles and conference proceedings. Without his precious encouragement, it would not be possible to conduct this research.

The author of the dissertation would like to thank his family: mother Dorothy Akorfa Djokoto and sister Lawrencia Emefa Aning who lost their lives during the author's Ph.D studies. The author wishes to thank his wife Synthia Fafa Djokoto, brothers Michael Nornudzor Djokoto, Enyonam Djokoto, Gabriel Selorm Djokoto and sisters Pascaline Atikpui and Anna Caquo, his uncles Dr. Maxwel Avoke and Mr. Siegfried Djokoto, aunt Dr. Fenella Avoke, cousins Dr. Edem Avoke, Mr. Patrick Senyo Avoke, Chief Leslie Kofi Avoke, Miss Sarah Djokoto and Miss Ivy Lawson for providing moral and emotional support throughout the PhD studies.

Lastly, the author of the dissertation would like to thank Lithuania for being his home for the last four years.

## REFERENCES


1. Rajeshkumar S. and Manoharan R. (2020) " Recent developments in semi-active control of magnetorheological materials-based sandwich structures: A review" *Journal of Thermoplastic Composite Materials*, 1–33, doi:10.1177/0892705720930749
2. Yuan, L., Sun, S., Pan, Z., Ding, D., Gienke, O., & Li, W. (2019). "Mode coupling chatter suppression for robotic machining using semi-active magnetorheological elastomers absorber". *Mechanical Systems and Signal Processing*, 117, 221–237. doi:10.1016/j.ymssp.2018.07.051
3. Liu, J., Tian, H., Lucas, E., Raja, A. S., Lihachev, G., Wang N.R., He, J., Liu, T., Anderson, M.H., Weng, W., Bhave, S.A., and Kippenberg T.J., (2020) "Monolithic piezoelectric control of soliton microcombs." *Nature* 583, 385–390. doi:10.1038/s41586-020-2465-8
4. Qiu Z. (2012) "Optical MEMS. Microelectromechanical Systems and Devices", *InTech*, pp. 291-330
5. Kalscheur M. P. and Nawasra J., "Actuated optical element for light beam scanning device" (2015) *U.S. Patent* No. US10107914B2
6. Bansevičius, R., Mazeika, D., Kulvietis, G., Tumasoniene, I., Drukteinienė, A., Jurenas, V., and Bakanauskas, V. (2017). "Investigation of sphere trajectories of a rotational type piezoelectric deflector". *Mechanical Systems and Signal Processing*. vol.136. doi:10.1016/j.ymssp.2017.05.038
7. Qiu Z., Pulskamp J. S., Lin X., Rhee C. H., Wang T., Polcawich R. G., and Oldham K. (2010) "Large displacement vertical translational actuator based on piezoelectric thin films". *Journal of Micromechanics and Microengineering*, vol. 20, issue 7, p. 1-10.
8. Wu L., Dooley S., Watson E., McManamon P. F., and Xie H. (2012) "A tip-tilt-piston micromirror array for optical phased array applications." *Journal of Microelectromechanical Systems*, vol. 19, issue 6, p. 1450-1461.
9. Janutėnaitė-Bogdanienė, J. (2019). "Control of piezorobots' trajectories for nanosatellite stabilization" *doctoral dissertation*. Vilnius: Technika, 126 p.
10. McManamon P. F., and Ataei (2019), "Progress and opportunities in optical beam steering," *Proc. SPIE 10926, Quantum Sensing and Nano Electronics and Photonics XVI*, 1092610 ; doi: 10.1117/12.2511987
11. Beltran-Carbajal F. and Silva-Navarro G. (2020), " Output feedback dynamic control for trajectory tracking and vibration suppression" *Applied Mathematical Modelling*, vol. 79, pp. 793-808, doi.10.1016/j.apm.2019.11.004
12. Frahm, H. "Device for damping vibrations of bodies". *U.S. Patent* No. 989958, 18 April 1911
13. Kolekar, S., Venkatesh, K., Oh, J. (2019)."Vibration Controllability of Sandwich Structures with Smart Materials of Electrorheological Fluids and Magnetorheological Materials: A Review". *J. Vib. Eng. Technol.* 7, 359–377. https://doi.org/10.1007/s42417-019-00120-5

14. Lara-Prieto, V., Rob P., Mike J., Vadim S. and Zbigniew K., (2010). "Vibration characteristics of MR cantilever beam sandwich beams: experimental study". *Smart Materials & Structures*, vol. 19 (1), 015005.
15. Chih-Jer L., Her-Terng Y., Chun-Ying L., and Kai-Hung T. (2013). "System Identification and Semiactive Control of a Squeeze-Mode Magnetorheological Damper", *IEEE/ASME Transactions on Mechatronics* , vol. 18, no. 6,
16. Asif K. and Heung S-K., (2019) "Active Vibration Control of a Piezo-Bonded Laminated Composite in the Presence of Sensor Partial Debonding and Structural Delaminations". *Sensors*, vol.19, pp.540; doi:10.3390/s19030540
17. Hong, S.-W.; Yoon, J.-Y.; Kim, S.-H.; Lee, S.-K.; Kim, Y.-R.; Park, Y.-J.; Kim, G.-W., and Choi, S.-B. (2019) "3D-Printed Soft Structure of Polyurethane and Magnetorheological Fluid: A Proof-of-Concept Investigation of its Stiffness Tunability". *Micromachines*, 10, 655.
18. Chih-Jer L., Chun-Ying L. and Ying L., (2017) "Vibration Control Design for a Plate Structure with Electrorheological ATVA Using Interval Type-2 Fuzzy System". *Appl. Sci*,7, 707; doi:10.3390/app7070707
19. Sudhawiyangkul, T., Yoshida, K., Eom, S. I., & Kim, J. (2019), "A study on a hybrid structure flexible electro-rheological microvalve for soft microactuators". *Microsystem Technologies*. vol. 26, pp. 309–321. doi:10.1007/s00542-019-04492-2
20. Maurya, J. B., Prajapati, Y. K., Singh, V., Saini, J. P., and Tripathi, R. (2016)."Improved performance of the surface plasmon resonance biosensor based on graphene or MoS2 using silicon." *Optics Communications*, 359, 426–434. doi:10.1016/j.optcom.2015.10.010
21. Setiono, A., Xu, J., Fahrbach, M., Bertke, M., Nyang'au, W., Wasisto, H., and Peiner, E. (2019)."Real-Time Frequency Tracking of an Electro-Thermal Piezoresistive Cantilever beam Resonator with ZnO Nanorods for Chemical Sensing". *Chemosensors*, 7(1), 2. doi:10.3390/chemosensors7010002
22. Liao, J., Wang, J., Li, N., Zhu, Y., Zhang, J., Yang, J., and Yang, F. (2016)."Resonance frequency tracking and measuring system for micro-electromechanical cantilever beam array sensors." *Microsystem Technologies*, 23(6), 2013–2021. doi:10.1007/s00542-016-2930-3
23. Kaluvan, S., and Zhang, H. (2016). "A Novel DC Current Sensor Using SMA Controlled Piezoelectric Bimorph Cantilever beam." *Multifunctional Materials; Mechanics and Behavior of Active Materials; Integrated System Design and Implementation; Structural Health Monitoring*. Vol. 1 doi:10.1115/smasis2016-9239
24. Chen, T.-H., Chiu, J., Cheng, C.-W., and Lu, M. S.-C. (2018)."Design and Characterization of Capacitively Sensed Squeeze-Film Pressure Sensors." *IEEE Sensors Journal*, 1–1. doi:10.1109/jsen.2018.2883477
25. Kaluvan, S., Shah K. and Choi S-B, (2014) "A new resonant based measurement method for squeeze mode yield stress of magnetorheological fluids" *Smart Mater. Struct*. 23 115017 doi:10.1088/0964-1726/23/11/115017.

26. Haiqing, G., Lim Mong King, and Tan Bee Cher. (1993)."Influence of a Locally Applied Electro-Rheological Fluid Layer on Vibration of a Simple Cantilever Beam." *Journal of Intelligent Material Systems and Structures*, 4(3), 379–384. doi:10.1177/1045389x9300400311
27. Tan, A. S., Belkner, J., Stroschke, A., and Sattel, T. (2019)."Damping Adjustment utilizing Digital Electrorheological Valves with Parallely Segmented Electrodes." *Smart Materials and Structures.* vol.28, issue 7. doi:10.1088/1361-665x/ab18d6
28. Bowen, C.R.; Kim, H.A.; Weaver, P.M.; and Dunn, S. (2014) "Piezoelectric and ferroelectric materials and structures for energy harvesting applications." *Energy Environ. Sci.*, 7, 25–44.
29. Dauksevicius, R., Gaidys, R., Ostasevicius, V., Lockhart, R., Vásquez Quintero, A., de Rooij, N. F., and Briand, D. (2018). "Nonlinear piezoelectric vibration energy harvester with frequency-tuned impacting resonators for improving broadband performance at low frequencies." *Smart Materials and Structures.* vol.28, issue 2. doi:10.1088/1361-665x/aaf358
30. Li H., Tian C., and Deng Z. D. (2014) "Energy harvesting from low frequency applications using piezoelectric materials" Applied Physics Reviews, vol. 1, no. 4. American Institute of Physics Inc., pp. 041301,
31. Tang L., Yang Y., and Soh C. K., (2010) "Toward broadband vibration-based energy harvesting," *J. Intell. Mater. Syst. Struct.*, vol. 21, no. 18, pp. 1867–1897.
32. Kumar R. and Weber R. J. (2015), "A broadband bistable piezoelectric cantilever beam-based vibration energy harvester with nonlinear high power extraction" *IEEE Transactions on Power Electronics*. vol. 30, Issue: 12, pp. 6763 – 6774, doi:10.1109/TPEL.2015.2394392
33. Staaf, L. G. H., Smith, A. D., Lundgren, P., Folkow, P. D., and Enoksson, P. (2018). "Effective Piezoelectric Energy Harvesting with Bandwidth Enhancement by Asymmetry Augmented Self-Tuning of Conjoined Cantilever beams". *International Journal of Mechanical Sciences*. vol.150, pp. 1-11. doi:10.1016/j.ijmecsci.2018.09.050.
34. Zhang, J., and Qin, L. (2019)."A tunable frequency up-conversion wideband piezoelectric vibration energy harvester for low-frequency variable environment using a novel impact- and rope-driven hybrid mechanism." *Applied Energy*, 240, pp. 26–34. doi:10.1016/j.apenergy.2019.01.261
35. Žižys, D., Gaidys, R., Ostaševičius, V., and Narijauskaitė, B. (2017). "Vibro-Shock Dynamics Analysis of a Tandem Low Frequency Resonator—High Frequency Piezoelectric Energy Harvester." *Sensors*, 17(5), 970. doi:10.3390/s17050970.
36. Zhang J. and Qin L., (2019) "A tunable frequency up-conversion wideband piezoelectric vibration energy harvester for low-frequency variable environment using a novel impact- and rope-driven hybrid mechanism," *Appl. Energy*, vol. 240, pp. 26–34,
37. Panthongsy, P., Isarakorn, D., Janphuang, P., and Hamamoto, K. (2018). "Fabrication and evaluation of energy harvesting floor using piezoelectric

frequency up-converting mechanism". *Sensors and Actuators A: Physical*, 279, 321–330. doi:10.1016/j.sna.2018.06.035

38. Challa, V. R., Prasad, M. G., Shi, Y., and Fisher, F. T. (2008). "A vibration energy harvesting device with bidirectional resonance frequency tenability". *Smart Materials and Structures*, 17(1), 015035. doi:10.1088/0964-1726/17/01/015035
39. Ostasevicius, V., Janusas, G., Milasauskaite, I., Zilys, M., and Kizauskiene, L. (2015). "Peculiarities of the Third Natural Frequency Vibrations of a Cantilever beam for the Improvement of Energy Harvesting". *Sensors*, 15(6), 12594–12612. doi:10.3390/s150612594
40. Yan L., Chen I-M., Lim C. K, Yang G. and Lee K-M. (2011) “Design, Modeling and Experiments of 3-DOF Electromagnetic Spherical Actuators", *Mechanisms and Machine Science,* vol. 4.
41. Tertitski, L., Kuttannair, Hunter, K. A. and Moffatt, S. "Laser beam positioning system", *US Patent* application number: 20110239421, 2011.
42. Huff M. (2020) "Microsystems Manufacturing Methods: MEMS Processes". *In: Process Variations in Microsystems Manufacturing. Microsystems and Nanosystems*. *Springer, Cham*, doi.10.1007/978-3-030-40560-1_4
43. Bansevicius R., Navickaitė, S., Jurenas, V, Mačiukienė V., Kulvietis, G., and Mazeika, D. (2016), " Piezoelectric laser beam deflector for space applications" *Journal of Vibroengineering*, vol. 18, issue 2, pp. 1008-1015.
44. Aimanoto, T., (2014) "Optical deflector including narrow piezoelectric sensor element between torsion bar and piezoelectric actuator", *United States Patent* Application 20140071507.
45. Zhi, D., Ma, Y., Si, L., Wang, X. and Zhou, P., (2014), "Experimental demonstration of adaptive fiber-optics collimator based on flexible hinges", *Proc. SPIE 9294, International Symposium on Optoelectronic Technology and Application 2014: Development and Application of High Power Lasers,* 92940, doi.10.1117/12.2072865
46. Pichugina, Y.V., Nosov, P.A., Batshev, V.I. Machikhin, A.S., Kozlov, A.B., and Krasin, G.K., (2019) "3D manipulation of micro-objects based on optical tweezers using acousto-optic deflector and variofocal system", *Proc. SPIE 11060, Optical Methods for Inspection, Characterization, and Imaging of Biomaterials IV*, 110601A, doi;10.1117/12.2525390
47. Abiri, A., Pensa, J., Tao, A. Ma, J., Juo, Y-Y, Askari, S.J., Bisley J., Rosen, J., Dutson, E.P., and Grundfest, W. S. (2019) "Multi-Modal Haptic Feedback for Grip Force Reduction in Robotic Surgery". *Sci Rep*. 9, 5016. doi;/10.1038/s41598-019-40821-1
48. Luo, J., Lin, Z., Li, Y., & Yang, C. (2020). "A Teleoperation Framework for Mobile Robots Based on Shared Control". *IEEE Robotics and Automation Letters*, 5(2), 377–384. doi:10.1109/lra.2019.2959442
49. Mazursky, A., Koo, J.-H., and Yang, T.-H. (2019)."Design, modeling, and evaluation of a slim haptic actuator based on electrorheological fluid". *Journal of Intelligent Material Systems and Structures*, 1045389X1983617. doi:10.1177/1045389x19836172

50. Chen, D., Song, A., Tian, L., Zeng, H., and Xiong, P. (2019). "Development of a Multi-Directional Controlled Small-scale Spherical MR Actuator for Haptic Applications". *IEEE/ASME Transactions on Mechatronics*, 1–1. doi:10.1109/tmech.2019.2916099
51. Mousavi, S. H., and Sayyaadi, H. (2018)."Optimization and Testing of a New Prototype Hybrid MR Brake With Arc Form Surface as a Prosthetic Knee". *IEEE/ASME Transactions on Mechatronics*, 23(3), 1204–1214. doi:10.1109/tmech.2018.2820065
52. Quoc, N. V., Tuan, L. D., Hiep, L. D., Quoc, H. N., and Choi, S. B. (2019)."Material Characterization of MR Fluid on Performance of MRF Based Brake". *Frontiers in Materials*, doi:10.3389/fmats.2019.00125
53. Jinaga R., Kolekar S., and Jagadeesha T. (2019) "Magneto Rheological Fluid Based Smart Automobile Brake and Clutch Systems*". In: Katiyar J., Bhattacharya S., Patel V., Kumar V. (eds) Automotive Tribology. Energy, Environment, and Sustainability*. Springer, Singapore
54. Ghavghave, M. A., and Darade, P. D. (2017)."Spherical Smart Brake for Multi-Degree of Freedom and Positional Stability". *Materials* , 4(8), 7793–7800. doi:10.1016/j. matpr.2017.07.114
55. Song, Y., Panas, R. M., and Hopkins, J. B. (2018). "A review of micromirror arrays". *Precision Engineering*, 51, 729–761. doi:10.1016/j.precisioneng.2017.08.012
56. Bansevicius, R., Jurenas, V., Kulvietis, G., and Drukteiniene, A. (2017). "Robots with increased number of degree-of-freedom with single exciting force". *Precision Engineering*, 48, 315–322. doi:10.1016/j.precisioneng.2017.01.001
57. Kang, S.-R., Cha, S.-W., Hwang, Y.-H., Lee, Y.-S., and Choi, S.-B. (2018). “Controllable magnetorheological fluid based actuators for 6-degree-of-freedom haptic master applicable to robot-assisted surgery". *Sensors and Actuators A: Physical*, 279, 649–662. doi:10.1016/j.sna.2018.06.057
58. Rabinow, J. (1948) "The magnetic fluid clutch." *AIEE Trans*. 67, 1308–1315
59. Senjoti, F. G., Ghori, M. U., Diryak, R., Conway, B., Morris, G. A., and Smith, A. M. (2019). "Rheo-Dissolution: A new platform for the simultaneous measurement of rheology and drug release". *Carbohydrate Polymers*, 115541. doi:10.1016/j.carbpol.2019.115541
60. Hilber, W. (2016) "Stimulus-active polymer actuators for next-generation microfluidic devices." *Appl. Phys. A* 122, 751. doi: 10.1007/s00339-016-0258-6
61. Bansevičius, R., Zhurauski M., Dragašius, E. and Chodočinskas, S., (2008) " Destruction of chains in magnetorheological fluids by high frequency oscillation" *Mechanika.* vol. 73(5): 2029-6983
62. Winslow, W. M. (1947) "Method and Means for Translating Electrical Impulses into Mechanical Force", *US Patent* 2417850.
63. Winslow, W. M. (1949) "Induced Fibration of Suspensions", *Journal of Applied Physics*, vol. 20, pp.1137-1140.
64. Li, Q., Zhao, J., Jin, L., and Li, D. (2020). "Experimental Study on Thermal Conductivity and Magnetization Behaviors of Kerosene-Based Ferrofluid Loaded

with Multiwalled Carbon Nanotubes". *ACS Omega*. doi:10.1021/acsomega.0c00964

65. Deng H., Du Y., Wang Z., Ye J., Zhang J., Ma M. and Zhong Xi. (2019)." Poly-stable energy harvesting based on synergetic multistable vibration ". *Communication Physics* doi:10.1038/s42005-019-0117-9
66. Hajalilou, A., Amri Mazlan, S., Lavvafi, H., and Shameli, K. (2016). "Magnetorheological (MR) Fluids". *Engineering Materials*, 13–50. doi:10.1007/978-981-10-2495-5_3
67. Carlson, J. D., and Jolly, M. R. (2000). "MR fluid, foam and elastomer devices". *Mechatronics*, 10(4-5), 555–569. doi:10.1016/s0957-4158(99)00064-1
68. Ziabska, E., Duchowski, J., Olszak, A., Osowski, K., Kesy, A., Kesy, Z., and Choi, S. B. (2017)."Wear forms of heterogeneous electro-rheological fluids working in a hydraulic clutch system". *Smart Materials and Structures*, 26(9), 095032. doi:10.1088/1361-665x/aa78dc
69. Genc, S. (2017). "Heat Transfer of Ferrofluids. Nanofluid" *Heat and Mass Transfer in Engineering Problems*. doi:10.5772/65912
70. Nepomnyashchaya, E. K., Prokofiev, A. V., Velichko, E. N., Pleshakov, I. V., and Kuzmin, Y. I. (2017). "Investigation of magneto-optical properties of ferrofluids by laser light scattering techniques". *Journal of Magnetism and Magnetic Materials*, 431, 24–26. doi:10.1016/j.jmmm.2016.10.002
71. Nagornyia, A.V., Socoliucc, V., Petrenkoa, V.I. , Almasy , L., Ivankova, O.I., Avdeeva , M.V., Bulavin, L.A., and Vekasc, L., (2020) " Structural characterization of concentrated aqueous ferrofluids", *Journal of Magnetism and Magnetic Materials* 501 166445, doi:10.1016/j.jmmm.2020.166445
72. Korobko, V. E., Zhurauski, M. A., Novikova, Z. A., (2017), "Viscoelastic Properties of Composite Electrorheological Suspensions", *Current Smart Materials*, vol. 2, no 1, pp. 12-19(8), doi;/10.2174/2405465801666161017122730
73. Lu, Q., Han, W., and Choi, H. (2018)." Smart and Functional Conducting Polymers: Application to Electrorheological Fluids". *Molecules*, 23(11), 2854. doi:10.3390/molecules23112854
74. Wang, D., Zi, B., Zeng, Y., Xie, F., and Hou, Y. (2015)."Measurement of temperature-dependent mechanical properties of magnetorheological fluids using a parallel disk shear stress testing device". *Proceedings of the Institution of Mechanical Engineers, Part C: Journal of Mechanical Engineering Science,* 231(9), 1725–1737. doi:10.1177/0954406215621099
75. Vtulkina, E. D., and Elfimova, E. A. (2017). "Thermodynamic and magnetic properties of ferrofluids in external uniform magnetic field". *Journal of Magnetism and Magnetic Materials*, 431, 218–221. doi:10.1016/j.jmmm.2016.08.033
76. Khuntia, S., Yadav, R., Singh, R. C., and Rastogi, V. (2020). "Design, development and analysis of a magnetorheological damper". *IOP Conference Series: Materials Science and Engineering*, 804, 012009. doi:10.1088/1757-899x/804/1/012009

77. Larose, P., Denninger, M., Julio, G., Plante, J-S, (2016). " Strength training device using magnetorheological fluid clutch apparatus" *US Patent*, US20180214730A1
78. Anupama, A. V., Kumaran, V., and Sahoo, B. (2019). "Synthesis of highly magnetic Mn-Zn ferrite (Mn0.7Zn0.3Fe2O4) ceramic powder and its use in smart magnetorheological fluid". *Rheologica Acta*. vol. 58, pp 273–280. doi:10.1007/s00397-019-01137-z
79. Bastola, A. K., Hoang, V. T., and Li, L. (2017). "A novel hybrid magnetorheological elastomer developed by 3D printing". *Materials & Design*, 114, 391–397. doi:10.1016/j.matdes.2016.11.006
80. Kumar, R., A.V., A., Kumaran, V., and Sahoo, B. (2018). "Effect of solvents on the structure and magnetic properties of pyrolysis derived carbon globules embedded with iron/iron carbide nanoparticles and their applications in magnetorheological fluids". *Nano-Structures & Nano-Objects*, pp. 16, 167–173. doi:10.1016/j.nanoso.2018.06.002
81. Bhaiya V., Bharti S.D., Shrimali M.K., and Datta T.K. (2019) "Performance of Semi-Actively Controlled Building Frame Using MR Damper for Near-Field Earthquakes". *In: Rao A., Ramanjaneyulu K. (eds) Recent Advances in Structural Engineering*, Lecture Notes in Civil Engineering, vol 12. pp 397-407 https://doi.org/10.1007/978-981-13-0365-4_34
82. L. Corporation, MRF-140CG, Magneto-Rheological Fluids, http://www.lord.com/products-and solutions/magnetorheological-(mr)/product.xml/1646. (2014)
83. Bastola, A. K., Ang, E., Paudel, M., and Li, L. (2019). "Soft hybrid magnetorheological elastomer: gap bridging between MR fluid and MR elastomer". *Colloids and Surfaces A: Physicochemical and Engineering Aspects*, 123975. doi:10.1016/j.colsurfa.2019.123975
84. Ahmadian, M. (2017). "Magneto-rheological suspensions for improving ground vehicle’s ride comfort, stability, and handling". *Vehicle System Dynamics*, vol. 55, issue 10, pp.1618–1642. doi:10.1080/00423114.2017.1323106
85. Türkücü, T., and Keleş, Ö. (2018) "Magneto-rheological engine mount design and experimental characterization". *J. Mech Sci Technol* vol. 32, pp. 5171–5178. https://doi.org/10.1007/s12206-018-1015-y
86. Daniel C., Hemalatha G., Sarala L., Tensing D., Manoharan S.S., and Bai X.X. (2020) "Experimental Investigation of a Self-powered Magnetorheological Damper for Seismic Mitigation". In: Ha-Minh C., Dao D., Benboudjema F., Derrible S., Huynh D., Tang A. (eds) CIGOS 2019, *Innovation for Sustainable Infrastructure.* Lecture Notes in Civil Engineering, vol 54. pp 397-402, Singapore. https://doi.org/10.1007/978-981-15-0802-8_61
87. Aguilera Portillo, M., Santa Ana Lozada, P., Figueroa, I., Suárez, M., Delgado, A., and Iglesias, G. (2015). "Synergy between magnetorheological fluids and aluminum foams: Prospective alternative for seismic damping". *Journal of Intelligent Material Systems and Structures*, vol.27 issue 7, pp. 872–879. doi:10.1177/1045389x15596624

88. Warrier, J., and Ali, S. F. (2017). "Control of ground resonance in helicopters using semi active damping". *Indian Control Conference (ICC).* doi:10.1109/indiancc.2017.7846461
89. Hasheminejad, S. M., and Fadavi-Ardakani, A. (2018). "Elasto-acoustic response damping performance of a smart cavity-coupled electro-rheological fluid sandwich panel". *Journal of Sandwich Structures & Materials*, vol 20, issue 6, 109963621667385. doi:10.1177/1099636216673857
90. Binyet, E.M. and Chang, J. (2020) "Magnetohydrodynamics modelling of a permanent magnets activated MRF clutch–brake". *Microsyst Technol*. vol. 26 pp. 3451–3457 https://doi.org/10.1007/s00542-020-04910-w
91. Olszak, A., Osowski, K., Kęsy, Z., and Kęsy, A. (2019)."Modelling and testing of a hydrodynamic clutch filled with electrorheological fluid in varying degree". *Journal of Intelligent Material Systems and Structures*, vol 30, issue 4 1045389X1881878. doi:10.1177/1045389x18818780
92. Migus, M., Musiałek, I., Mędrek, G., Kęsy, Z., Kęsy, A., Kim, J-H and Choi, S-B, (2020), "Measurements of shear stress in ER/MR fluids used in valves by adapting centrifugal force" *Journal of Intelligent Material Systems and Structures*, vol. 29, no. 7
93. Wu, J., Song, Z., Liu, F., Guo, J., Cheng, Y., Ma, S. and Xu, G. (2016). "Giant electrorheological fluids with ultrahigh electrorheological efficiency based on a micro/nano hybrid calcium titanyl oxalate composite". *NPG Asia Materials*, 8(11), e322–e322. doi:10.1038/am.2016.158
94. Bhowmik S.,and Zindani D. (2019) "Electrorheological Fluid-Assisted Micro-USM. In: Hybrid Micro-Machining Processes". *Springer Briefs in Applied Sciences and Technology. Springer, Cham.* https://doi.org/10.1007/978-3-030-13039-8_4
95. Su, J., Cheng, H., Feng, Y., and Tam, H.-Y. (2016)."Study of a wheel-like electrorheological finishing tool and its applications to small parts". *Applied Optics*, 55(4), 638. doi:10.1364/ao.55.000638
96. Mazursky, A., Koo, J.-H., & Yang, and T.-H. (2019). "Design, modeling, and evaluation of a slim haptic actuator based on electrorheological fluid". *Journal of Intelligent Material Systems and Structures*, vol 30, issue 17 1045389X1983617. doi:10.1177/1045389x19836172
97. Han, Y.-M., Choi, S.-B., and Oh, J.-S. (2015). "Tracking controls of torque and force of 4-degree-of-freedom haptic master featuring smart electrorheological fluid". *Journal of Intelligent Material Systems and Structures,* 27(7), 915–924. doi:10.1177/1045389x15610901
98. Ahamed, R., Ferdaus, M. M., and Li, Y. (2016). "Advancement in energy harvesting magneto-rheological fluid damper: A review". *Korea-Australia Rheology Journal*, 28(4), 355–379. doi:10.1007/s13367-016-0035-2
99. Khairul, M. A., Doroodchi, E., Azizian, R., and Moghtaderi, B. (2017). "Advanced applications of tunable ferrofluids in energy systems and energy harvesters: A critical review". *Energy Conversion and Management*, vol.149, pp. 660–674. doi:10.1016/j.enconman.2017.07.064

100. Volkova, T. I., Böhm, V., Naletova, V. A., Kaufhold, T., Becker, F., Zeidis, I., and Zimmermann, K. (2017). "A ferrofluid based artificial tactile sensor with magnetic field control". *Journal of Magnetism and Magnetic Materials*, vol. 431, pp.277–280. doi:10.1016/j.jmmm.2016.09.105
101. Bannwarth, M. B., Utech, S., Ebert, S., Weitz, D. A., Crespy, D., and Landfester, K. (2015). "Colloidal Polymers with Controlled Sequence and Branching Constructed from Magnetic Field Assembled Nanoparticles". *ACS Nano*, vol. 9(3), pp. 2720–2728. doi:10.1021/nn5065327
102. Yu, Y., Shang, L., Gao, W., Zhao, Z., Wang, H., and Zhao, Y. (2017). "Microfluidic Lithography of Bioinspired Helical Micromotors". *Angewandte Chemie*, vol. 129(40), pp.12295–12299. doi:10.1002/ange.201705667
103. Wang, W., Fan, X., Li, F., Qiu, J., Umair, M. M., Ren, W., Ju, B., Zhang, S., and Tang, B. (2017). "Magnetochromic Photonic Hydrogel for an Alternating Magnetic Field-Responsive Color Display". *Advanced Optical Materials*, 6(4), 1701093. doi:10.1002/adom.201701093
104. Panaseti, P., Damianou, Y., Georgiou, G. C., and Housiadas, K. D. (2018). "Pressure-driven flow of a Herschel-Bulkley fluid with pressure-dependent rheological parameters". *Physics of Fluids*, 30(3), 030701. doi:10.1063/1.5002650
105. Ulbrich, K., Holá, K., Šubr, V., Bakandritsos, A., Tuček, J., and Zbořil, R. (2016). "Targeted Drug Delivery with Polymers and Magnetic Nanoparticles: Covalent and Noncovalent Approaches, Release Control, and Clinical Studies". *Chemical Reviews*, vol. 116(9), pp. 5338–5431. doi:10.1021/acs.chemrev.5b00589
106. Jose, J., Kumar, R., Harilal, S., Mathew, G. E., Parambi, D. G. T., Prabhu, A., Uddin, M. S., Aleya, L., Kim, H. and Mathew, B. (2019). "Magnetic nanoparticles for hyperthermia in cancer treatment: an emerging tool". *Environmental Science and Pollution Research*. vol. 27, pp.19214–19225 doi:10.1007/s11356-019-07231-2
107. Li, G., and Yang, Z.-B. (2020). "Modelling and Analysis of a Magnetorheological Damper with Nonmagnetized Passages in Piston and Minor Losses". *Shock and Vibration*, 1–12. doi:10.1155/2020/2052140
108. Namgung, R., Singha, K., Yu, M. K., Jon, S., Kim, Y. S., Ahn, Y., Park, I-K., and Kim, W. J. (2010). "Hybrid superparamagnetic iron oxide nanoparticle-branched polyethylenimine magnetoplexes for gene transfection of vascular endothelial cells". *Biomaterials*, 31 (14), 4204–4213. doi:10.1016/j.biomaterials.2010.01.123
109. Donato, P., Mardare, S. and Vernescu, B. (2018) "Bingham Flows in Periodic Domains of Infinite Length". *Chinese Annals of Mathematics,* vol. 39, Issue 2, pp183-200. https://doi.org/10.1007/s11401-018-1059-3
110. Kumar, A., and Subudhi, S. (2017). "Preparation, characteristics, convection and applications of magnetic nanofluids": *A review. Heat and Mass Transfer*, 54(2), 241–265. doi:10.1007/s00231-017-2114-4

111. Marinca, V., Ene, R.-D., and Bereteu, L. (2017). "Application of the optimal homotopy asymptotic method to nonlinear Bingham fluid dampers". *Open Physics*, 15 (1), 620–626. doi:10.1515/phys-2017-0072
112. Anupama, A.V., Kumaran, V. and Sahoo, B. (2019) "Synthesis of highly magnetic Mn-Zn ferrite (Mn0.7Zn0.3Fe2O4) ceramic powder and its use in smart magnetorheological fluid". *Rheol Acta* vol. 58, pp. 273–280. https://doi.org/10.1007/s00397-019-01137-z
113. Yang, J., Sun, S., Guo, N., Ning, D., Nakano, M., Li, Li, Z., Du , H.. Zhang, S.W. and Li, W. (2019)."Development of a smart rubber joint for train using shear thickening fluids". *Smart Materials and Structures*. vol 29, nr. 5 doi:10.1088/1361-665x/ab5cf9
114. Shou, M., Liao, C., Zhang, H., Li, Z., and Xie, L. (2018). "Modeling and testing of magnetorheological energy absorbers considering inertia effect with non-averaged acceleration under impact conditions". *Smart Materials and Structures*. vol.27, issue 11. doi:10.1088/1361-665x/aae6a0
115. Li, S., Tian, T., Wang, H., Li, Y., Li, J., Zhou, Y., and Wu, J. (2020). "Development of a four-parameter phenomenological model for the nonlinear viscoelastic behaviour of magnetorheological gels". *Materials & Design*, vol.194, 108935. doi:10.1016/j.matdes.2020.108935
116. Wei, K., Zhao, Z., Du, X., Li, H., and Wang, P., (2019) " A theoretical study on the train-induced vibrations of a semi-active magneto-rheological steel-spring floating slab track", *Construction and Building Materials* vol. 204 703–715
117. Zhu, H., Rui, X., Yang, F., Zhu, W., and Wei, M. (2019)". An efficient parameters identification method of normalized Bouc-Wen model for MR damper". *Journal of Sound and Vibration*. vol. 448, pp. 146-158 doi:10.1016/j.jsv.2019.02.019
118. Barriere, T., Gabrion, X., and Holopainen, S. (2019). “A compact constitutive model to describe the viscoelastic-plastic behaviour of glassy polymers: Comparison with monotonic and cyclic experiments and state-of-the-art models". *International Journal of Plasticity*. vol. 122, pp. 31-48 doi:10.1016/j.ijplas.2019.05.010
119. Mazursky, A., Koo, J.-H., and Yang, T.-H. (2019). "Design, modeling, and evaluation of a slim haptic actuator based on electrorheological fluid". *Journal of Intelligent Material Systems and Structures*, vol.30, issue 17. 1045389X1983617. doi:10.1177/1045389x19836172
120. Ghorbanpour Arani, A., BabaAkbar-Zarei, H. and Jamali, S.A. (2019) "Application of smart electro-rheological dampers in semi-active control of electro-rheological sandwich plates with nanocomposite facesheets rested on orthotropic visco-Pasternak foundation". *J Braz. Soc. Mech. Sci. Eng*. 41, 426. https://doi.org/10.1007/s40430-019-1903-8
121. Zhou, H., Zhao, W., Zhang, H., Wang, Y., Wu, X., and Sun, Z. (2019). "Magnetorheological seal: A review". *International Journal of Applied Electromagnetics and Mechanics*, 1–24. doi:10.3233/jae-190082

122. Rossi, A., Orsini, F., Scorza, A., Botta, F., Belfiore, N., and Sciuto, S. (2018). "A Review on Parametric Dynamic Models of Magnetorheological Dampers and Their Characterization Methods". *Actuators,* 7(2), 16. doi:10.3390/act7020016
123. Peng, Y., Yang, J., and Li, J. (2017). "Parameter identification of modified Bouc–Wen model and analysis of size effect of magnetorheological dampers". *Journal of Intelligent Material Systems and Structures*, 29(7), 1464–1480. doi:10.1177/1045389x17740963
124. Spitas, C., Amani, A., and Spitas, V., (2015). "A review of emerging computational models for the design of smart structures and powertrains". *Journal of Coupled Systems and Multiscale Dynamics*, vol. 3, no. 4, https://doi.org/10.1166/jcsmd.2015.1090
125. Elsaady, W., Oyadiji, S. O., and Nasser, A. (2020). "A review on multi-physics numerical modelling in different applications of magnetorheological fluids". *Journal of Intelligent Material Systems and Structures*, vol.31, issue 16. 1045389X2093563. doi:10.1177/1045389x20935632
126. Zheng J, Li Y, and Li Z (2015) "Transient multi-physics analysis of a magnetorheological shock absorber with the inverse Jiles–Atherton hysteresis model". *Smart Materials and Structures* 24(10): 105024.
127. Bai, X.-X., Cai, F.-L., and Chen, P. (2019). "Resistor-capacitor (RC) operator-based hysteresis model for magnetorheological (MR) dampers". *Mechanical Systems and Signal Processing*, 117, 157–169. doi:10.1016/j.ymssp.2018.07.050
128. Elsaady W, Oyadiji SO and Nasser A (2020) "A one-way coupled numerical magnetic field and CFD simulation of viscoplastic compressible fluids in MR dampers". *International Journal of Mechanical Sciences* 167: 105265.
129. Spanner, K. and Koc, B., (2016) "Piezoelectric Motors, an Overview". *Actuators* 5, 6−24.
130. Sappati, K., and Bhadra, S. (2018). "Piezoelectric Polymer and Paper Substrates: A Review". *Sensors*, 18(11), 3605. doi:10.3390/s18113605
131. Joy, A., Varughese, S., Shanmugam, S., and Haridoss, P. (2019). "Multiwalled Carbon Nanotube Reinforced Epoxy Nanocomposites for Vibration Damping". *ACS Applied Nano Materials*. doi:10.1021/acsanm.8b01865
132. Bhudolia, S.K., Perrotey, P., and Joshi, S.C., (2017) "Enhanced Vibration damping and dynamic mechanical characteristics of composites with novel pseudo-thermoset matrix system", *Composite Structures*, vol.179, pp.502-513. doi: 10.1016/j.compstruct.2017.07.093
133. Zhang, C. M., Chen, Y. J., Li, H., Xue, W. C. Tian, R., Dugnani, R., and Liu, H. Z. (2018) "Facile fabrication of polyurethane-based graphene foam/lead zirconate titanate/polydimethylsiloxane composites with good damping performance". *RSC Adv*., 8, 7916−7923.
134. Choudhary, N., and Kaur, D. (2015) "Vibration Damping Materials and Their Applications in Nano/Micro-Electro-Mechanical Systems: A Review". *J. Nanosci. Nanotechnol*, 15, 1907−1924.

135. Carponcin, D., Dantras, E., Michon, G., Dandurand, J., Aridon, G., Levallois, F., Cadiergues, L. and Lacabanne, C. (2015) "New hybrid polymer nanocomposites for passive vibration damping by incorporation of carbon nanotubes and lead zirconate titanate particles". *J. Non-Cryst. Solids*, 409, 20−26
136. Trotter, C. (2018) "Dancefloor generates electricity at London's first eco-disco" https://inhabitat.com/green-a-go-go-at-londons-first-ecodisco/
137. Ryall, J. (2018) "Japan harnesses energy from footsteps". https://www.telegraph.co.uk/news/earth/energy/3721841/Japan-harnessesenergy-from-footsteps.html
138. Tone, T., and Suzuki, K. (2018). "An Automated Liquid Manipulation by Using a Ferrofluid-Based Robotic Sheet". *IEEE Robotics and Automation Letters*, 3(4), 2814–2821. doi:10.1109/lra.2018.2842251
139. Marinca, V., Ene, R.-D., and Bereteu, L. (2017). "Application of the optimal homotopy asymptotic method to nonlinear Bingham fluid dampers". *Open Physics*, 15(1), 620–626. doi:10.1515/phys-2017-0072
140. Chorsi, M. T., Curry, E. J., Chorsi, H. T., Das, R., Baroody, J., Purohit, P. K., Ilies H. and Nguyen, T. D. (2018). "Piezoelectric Biomaterials for Sensors and Actuators". *Advanced Materials*, 1802084. doi:10.1002/adma.201802084
141. Salazar, R., and Abdelkefi, A. (2020). "Nonlinear analysis of a piezoelectric energy harvester in body undulatory caudal fin aquatic unmanned vehicles". *Applied Energy*, 263, 114627. doi: 10.1016/j.apenergy.2020.114627
142. Kim, G., Hwang, Y.-I., Seo, M.-K., and Kim, K.-B. (2020). "Electrical tuning for sensitivity enhancement of a piezo-electric ultrasonic transducer: Simulation and fabrication". *Journal of Mechanical Science and Technology*, vol.34, pp. 3155–3164. doi:10.1007/s12206-020-0707-1
143. Ibn-Mohammed, T., Koh, S. C. L., Reaney, I. M., Sinclair, D. C., Mustapha, K. B., Acquaye, A., and Wang, D. (2017) "Are lead-free piezoelectrics more environmentally friendly" *MRS Commun*., 7, 1−7
144. Sethi, P., and Sarangi, S. R. (2017) "Internet of Things: Architectures, Protocols, and Applications". *Journal of Electrical and Computer Engineering* vol. 2017, pp. 25 doi:10.1155/2017/9324035 9324035.
145. Ponnamma, D., Sadasivuni, K. K., Cabibihan, J.-J., and Al-Maadeed, M. A. A. (2017) "Smart Polymer Nanocomposites: Energy Harvesting, Self-Healing and Shape Memory" *Applications*; Springer International Publishing: New York, NY.
146. Ji, S. H, Cho, J. H., Paik, J.-H., Yun, J., and Yun, J. S. (2017) "Poling effects on the performance of a lead-free piezoelectric nanofiber in a structural health monitoring sensor". *Sens. Actuators*, 263, 633−638
147. Zhou, M., Al-Furjan, M. S. H., Zou, J. and Liu, W. (2018)"A Review on heat and mechanical energy harvesting from human- Principles, prototypes, and perspectives". *Renewable Sustainable Energy* Rev. 82, 3582−3609
148. Hou, Y., Fast, D. B., Ruther, R. E., Amador, J. M., Fullmer, L. B., Decker, S. R., Zakharov, L. N., Dolgos, M. R. and Nyman, M., (2015) "The Atomic Level Journey from Aqueous Polyoxometalate to Metal Oxide". *J. Solid State Chem.*, 221, 418−425

149. Stempin, P., and Sumelka, W. (2020). "Space-Fractional Euler-Bernoulli beam model - theory and identification for silver nanobeam bending". *International Journal of Mechanical Sciences*, vol. 186, doi:10.1016/j.ijmecsci.2020.105902
150. Qin, Y., Wei, T., Zhao, Y., and Chen, H. (2018). "Simulation and experiment on bridge-shaped nonlinear piezoelectric vibration energy harvester". *Smart Materials and Structures*. vol. 28, nr. 4 doi:10.1088/1361-665x/aaf5ae
151. Lin, C., Shen, Z., Yu, J., Li, P., and Huo, D. (2018). "Modelling and Analysis of Characteristics of a Piezoelectric-Actuated Micro-/Nano Compliant Platform Using Bond Graph Approach". *Micromachines*, 9(10), 498. doi:10.3390/mi9100498
152. Shahab, S., and Erturk, A. (2016). "Coupling of experimentally validated electroelastic dynamics and mixing rules formulation for macro-fiber composite piezoelectric structures". *Journal of Intelligent Material Systems and Structures*, 28(12), 1575–1588. doi:10.1177/1045389x16672732
153. Ahoor, Z. H., Ghafarirad, H., and Zareinejad, M. (2021). "Nonlinear dynamic modeling of bimorph piezoelectric actuators using modified constitutive equations caused by material nonlinearity". *Mechanics of Advanced Materials and Structures,* vol. 28, Issue 8, pp. 763-773. doi:10.1080/15376494.2019.1590885
154. Bowen, C. R., Topolov, V. Y., and Kim, H. A. (2016). "Modern Piezoelectric Energy-Harvesting Materials". *Springer Series in Materials Science*. vol. 238 doi:10.1007/978-3-319-29143-7
155. Li F., Shen T., Wang C., Zhang Y., Qi J., and Zhang H. (2020). "Recent Advances in Strain-Induced Piezoelectric and Piezoresistive Effect-Engineered 2D Semiconductors for Adaptive Electronics and Optoelectronics". *Nano-Micro*, *12* (1) doi.org/10.1007/s40820-020-00439-9
156. Ramya R., Saravanakumar G., and Ravi S. (2016) "Energy Harvesting in Wireless Sensor Networks". In: Dash S., Bhaskar M., Panigrahi B., Das S. (eds) *Artificial Intelligence and Evolutionary Computations in Engineering Systems. Advances in Intelligent Systems and Computing*, vol. 394. Springer, New Delhi. https://doi.org/10.1007/978-81-322-2656-7_76
157. Zizys, D., Gaidys, R., Dauksevicius, R., Ostasevicius, V., and Daniulaitis, V. (2015). "Segmentation of a Vibro-Shock Cantilever -Type Piezoelectric Energy Harvester Operating in Higher Transverse Vibration Modes". *Sensors*, 16(1), 11. doi:10.3390/s16010011
158. Du, S., Jia, Y., Chen, S.-T., Zhao, C., Sun, B., Arroyo, E., and Seshia, A. A. (2017). "A new electrode design method in piezoelectric vibration energy harvesters to maximize output power". *Sensors and Actuators A*: *Physical*, 263, 693–701. doi:10.1016/j.sna.2017.06.026
159. Huang, H.-H., and Chen, K.-S. (2016). "Design, analysis, and experimental studies of a novel PVDF-based piezoelectric energy harvester with beating mechanisms". *Sensors and Actuators A: Physical*, 238, 317–328. doi:10.1016/j.sna.2015.11.036

160. Zhou, S., Yan, B., and Inman, D. (2018). "A Novel Nonlinear Piezoelectric Energy Harvesting System Based on Linear-Element Coupling: Design, Modeling and Dynamic Analysis". *Sensors*, 18(5), 1492. doi:10.3390/s18051492
161. “Data Sheet Piezoceramic Trimorph Bending Actuator, Part No. 427.0085.11Z, Johnson Matthey Piezoproducts Bahnhofstraße 43, D- 96254 Redwitz,” (2011). Johnson Matthey Piezoproducts
162. Chen, P., Bai, X.-X., Qian, L.-J., and Choi, S.-B. (2016). "A magneto-rheological fluid mount featuring squeeze mode: analysis and testing". *Smart Materials and Structures*, 25(5), 055002. doi:10.1088/0964-1726/25/5/055002
163. Electro-rheological fluid LID 3354s. Internet: www.smarttec.co.uk/res/lid3354s%20Rev%202.pdf
164. Luning, X., Han, L., Yufei, L., Shen, R., and Kunquan, L. (2017). "Operational durability of a giant ER valve for Braille display". *Smart Materials and Structures*, 26(5), 054003. doi:10.1088/1361-665x/aa64c4
165. Dragašius E., Jūrėnas V., Mačiukienė V., and Navickaitė S. (2012) "Investigation of magneto-rheological fluid parameters using cantilever beam-type piezoactuator". *Vibroengineering. Journal*. vol. 14, issue 1. ISSN 1392-8716
166. Lee J.-H., Han C., Ahn D., Lee J. K., Park S.-H., Park S., (2013) "Design and performance evaluation of a rotary magnetorheological damper for unmanned vehicle suspension systems", *Scientific World Journal*., vol.2013, pp.10. doi:/10.1155/2013/894016
167. Urekabharathi S and Padmasine K G, (2019), " Enhancement of Micro Cantilever’s Rectangular and Triangular Beam for Improvising the Sensitivity of Biosensor – a Comparative Study " *IOP Conf. Series: Materials Science and Engineering* 561 012011 IOP Publishing doi:10.1088/1757-899X/561/1/012011
168. Kaluvan S., Thirumavalavan V., Kim S. and Choi S-B, (2015) " A novel magnetorheological actuator for micro-motion control: identification of actuating characteristics" *Smart Mater. Struct*. 24 105006 doi:10.1088/0964-1726/24/10/105006
169. Halim, M. A., Kabir, M. H., Cho, H., & Park, J. Y. (2019)."A Frequency Up-Converted Hybrid Energy Harvester Using Transverse Impact-Driven Piezoelectric Bimorph for Human-Limb Motion". *Micromachines*, 10(10), 701. doi:10.3390/mi1010070
170. Richards C.D, Anderson M.J and Bahr D.F, 2004 "Efficiency of energy conversion for devices containing a piezoelectric component". *Journal of Micromechanics and Microengineering* 14(5): 717–721.
171. Wu L., Dooley S., Watson E., McManamon P.F., and Xie, H. A., (2012) "Tip-tilt-piston micromirror array for optical phased array applications", *J. Microelectromech. Syst.* 19 (6) 1450–1461.
172. Rabinow, J., “Magnetic fluid torque and force transmitting device”, *US Patent* 2,575,360, 1951
173. Spaggiari, A., Castagnetti, D., Golinelli, N., Dragoni, E., and Scirè Mammano, G. (2016)."Smart materials: Properties, design and mechatronic applications". *Proceedings of the Institution of Mechanical Engineers, Part L:*

*Journal of Materials: Design and Applications*, 146442071667367. doi:10.1177/1464420716673671
174. Mazlan, S.A. (2008). " The Behavior of Magnetorheological Fluids in Squeeze Mode." *doctoral dissertation. Dublin City University* , 253 p.
175. Carlson J.D. "Magnetorheological fluids" – ready for realtime motion control http://server2.docfoc.com/uploads/ Z2015/12/20/Yn4vmHgIdN/082d4d29ef3b7fcfc1979 c94332514f8.pdf (2000, accessed 7 October 2016).
176. Wereley N.M. (2013) "Magnetorheology". *Cambridge: Royal Society of Chemistry*. doi: 10.1039/9781849737548.
177. Qian, F., Zhou, W., Kaluvan, S., Zhang, H., and Zuo, L. (2018). "Theoretical modeling and experimental validation of a torsional piezoelectric vibration energy harvesting system". *Smart Materials and Structures*, 27(4), 045018. doi:10.1088/1361-665x/aab160
178. Dechant, E., Fedulov, F., Fetisov, L., and Shamonin, M. (2017). "Bandwidth Widening of Piezoelectric Cantilever Beam Arrays by Mass-Tip Tuning for Low-Frequency Vibration Energy Harvesting". *Applied Sciences*, 7(12), 1324. doi:10.3390/app7121324
179. Senthilkumar, M., Vasundhara, M.G. and Kalavathi, G.K. (2019) "Electromechanical analytical model of shape memory alloy based tunable cantilever beamed piezoelectric energy harvester". *Int J Mech Mater Des* 15, 611–627. https://doi.org/10.1007/s10999-018-9413-x
180. Deutz, D. B., Pascoe, J.-A., Schelen, B., van der Zwaag, S., de Leeuw, D. M., and Groen, P. (2018). "Analysis and experimental validation of the figure of merit for piezoelectric energy harvesters". *Materials Horizons*, 5(3), 444–453. doi:10.1039/c8mh00097b
181. Kang S-R, Cha S-W, Hwang Y-H, Lee Y-S and Cho S-B, (2018), " Controllable magnetorheological fluid based actuators for 6-degree-of-freedom haptic master applicable to robot-assisted surgery" *Sensors and Actuators A: Physical,* Vol. 279, pp. 649-662
182. Chen D., Song A., Tian L., Yu Y., and Zhu, L. (2018) "MH-Pen: A pen-type multi-mode haptic interface for touch screens interaction," *IEEE Trans. Haptics*, vol. 11, no. 4, pp. 555–567.
183. Walicka A. and Falick J. (2017) ,"Reynolds Number Effects in the Flow of a Vočadlo Electrorheological Fluid in a Curved Gap" *International Journal of Applied Mechanics and Engineering*, vol. 22, Issue 3, pp. 675–695, doi:/10.1515/ijame-2017-0043
184. Poddar A., Mandal S., Bandopadhyay A. and Chakraborty S., (2019) "Electrorheology of a dilute emulsion of surfactant-covered drops". *J. Fluid Mech*., vol. 881, pp. 524–550. doi:10.1017/jfm.2019.745.
185. Do ,T., Lee H., Ko Y. G., Chun Y., Choi U. S., and Kim C. H., (2017) "Influence of amine- and sulfonate-functional groups on electrorheological behavior of polyacrylonitrile dispersed suspension" *Journal of Colloids and*

*Surfaces A: Physicochemical and Engineering Aspects*, vol.514, pp. 56–62.. https://doi.org/10.1016/j.colsurfa.2016.11.032.
186. Heinken, H., Ulrich, S., Bruns, R., and Schneider, S. (2020). "High-response electrorheological servo valve". *Journal of Intelligent Material Systems and Structures*, vol 31, Issue 2, doi:10.1177/1045389X19873427
187. COMSOL, Inc., Los Angeles, CA
188. Ju, S., and Ji, C.-H. (2018). "Impact-based piezoelectric vibration energy harvester". *Applied Energy*, 214, 139–151. doi:10.1016/j.apenergy.2018.01.076
189. Marchetti, L., Berg, Y., Mirmotahari, O., and Azadmehr, M. (2016). "Bidirectional front-end for piezoelectric resonator". *IEEE 13th International Conference on Networking, Sensing, and Control (ICNSC)*. doi:10.1109/icnsc.2016.7479028
190. Truong, B. D., Williams, S., and Roundy, S. (2019). "Experimentally validated model and analytical investigations on power optimization for piezoelectric-based wireless power transfer systems". *Journal of Intelligent Material Systems and Structures*, vol. 30, Issue 16, doi:10.1177/1045389x19862383
191. Tarleton E. Balint D.S. Gong J. and Wilkinson A.J., (2015) " A discrete dislocation plasticity study of the micro-cantilever size effect" Acta Materialia Vol. 88, P 271-282 doi:10.1016/j.actamat.2015.01.030
192. Cantera, M. A., Behrooz, M., Gibson, R. F., and Gordaninejad, F. (2017). "Modeling of magneto-mechanical response of magnetorheological elastomers (MRE) and MRE-based systems: a review". Smart Materials and Structures, 26(2), 023001. doi:10.1088/1361-665x/aa549c
193. Yang, J., Sun, S. S., Zhang, S. W., and Li, W. H. (2019). "Review of structural control technologies using magnetorheological elastomers." *Current Smart Materials*, vol. 4, pp.22-28(7), doi:10.2174/2405465804666190326152207
194. Zhang, X., Sun, L., Yu, Y., and Zhao, Y. (2019). "Flexible Ferrofluids: Design and Applications." *Advanced Materials*, vol. 31, Issue 51. doi:10.1002/adma.201903497
195. Deng, Z., and Dapino, M. J. (2018). "Review of magnetostrictive materials for structural vibration control." Smart Materials and Structures, vol. 27, nr. 11, doi:10.1088/1361-665x/aadff5
196. Bruno, N. M., Wang, S., Karaman, I., and Chumlyakov, Y. I. (2017). "Reversible Martensitic Transformation under Low Magnetic Fields in Magnetic Shape Memory Alloys". *Scientific Reports*, nr. 40434. doi:10.1038/srep40434
197. Dong, Y. Z., Seo, Y., and Choi, H. (2019). "Recent Development of Electro-responsive Smart Electrorheological Fluids." *Soft Matter*. vol. 15, pp. 3473-3486, doi:10.1039/c9sm00210c
198. Eshaghi, M., Sedaghati, R., and Rakheja, S. (2016). "Dynamic characteristics and control of magnetorheological/electrorheological sandwich structures: A state-of-the-art review." *Journal of Intelligent Material Systems and Structures*, vol. 27(15), pp. 2003–2037. doi:10.1177/1045389x15620041

199. Zhu, Z.-L., Ni, S.-F., Chen, W.-C., Chen, M., Zhu, J.-J., Yuan, Y., and Lee, C.-S. (2018). "Tuning electrical properties of phenanthroimidazole derivatives to construct multifunctional deep-blue electroluminescent materials." *Journal of Materials Chemistry C*, 6(14), 3584–3592. doi:10.1039/c7tc04972b
200. Granqvist, C. G., Arvizu, M. A., Bayrak Pehlivan, İ., Qu, H.-Y., Wen, R.-T., and Niklasson, G. A. (2018). "Electrochromic materials and devices for energy efficiency and human comfort in buildings: A critical review." *Electrochimica Acta*, vol. 259, pp. 1170-1182. doi:10.1016/j.electacta.2017.11.169
201. Gridnev, S. A., Khakhlenkov, M. V. and Fetisov, L. Y., (2020) "The influence of the electric field on the magnetoelectric response of a layered ferromagnet – electrostrictor heterostructure." *Ferroelectrics*, 561:1, 90-99
202. Zarren, G., Nisar, B., and Sher, F. (2019). "Synthesis of anthraquinone based electroactive polymers: A critical review." *Materials Today Sustainability*, 100019. doi:10.1016/j.mtsust.2019.100019
203. Manjón-Sanz, A. M., and Dolgos, M. R. (2018), "Applications of Piezoelectrics: Old and New". vol. 30, pp.8718–8726 *Chemistry of Materials*. doi:10.1021/acs.chemmater.8b03296
204. Wei, H., Wang, H., Xia, Y., Cui, D., Shi, Y., Dong, M., Liu, C., Ding, T., Zhang, J., Ma, Y., Wang, N. Wang, Z., Sun, Y. Wei, R. and Guo, Z. (2018). "An Overview of Lead-Free Piezoelectric Materials and Devices." *Journal of Materials Chemistry C*. vol. 6, pp.12446-12467 doi:10.1039/c8tc04515a
205. Naresh, C., Bose, P. S. C., and Rao, C. S. P. (2016). "Shape memory alloys: a state of art review." *IOP Conference Series: Materials Science and Engineering*, 149, 012054. doi:10.1088/1757-899x/149/1/012054
206. Chowdhury, P., and Sehitoglu, H. (2017). "Deformation physics of shape memory alloys - Fundamentals at atomistic frontier." *Progress in Materials Science*, 88, 49–88. doi:10.1016/j.pmatsci.2017.03.003
207. Feser, J. P., and Ravichandran, J. (2018). "More power to pyroelectrics." *Nature Materials*, 17(5), 385–386. doi:10.1038/s41563-018-0065-x.
208. Al-Ashtari, W. (2016) “A Novel Analytical Model to Design Piezoelectric Patches Used to Repair Cracked Beams”, *Journal of Engineering*, 22(6), pp. 117-136. http://joe.uobaghdad.edu.iq/index.php/main/article/view/208
209. Tang, L., and Wang, J. (2017)."Size effect of tip mass on performance of cantilever beamed piezoelectric energy harvester with a dynamic magnifier". *Acta Mechanica*, 228(11), 3997–4015. doi:10.1007/s00707-017-1910-8
210. Kaluvan, S., Park, J., Lee, Y., Han, M., and Choi, S. (2016). “A new measurement method for operation mode dependent dynamic behavior of magnetorheological fluid". *Proceedings of the Institution of Mechanical Engineers, Part C: Journal of Mechanical Engineering Science*, vol. 231, Issue 18, pp. 3358–3369. doi:10.1177/0954406216646137
211. Marinică, O., Susan-Resiga, D., Bălănean, F., Vizman, D., Socoliuc, V., and Vékás, L. (2016). "Nano-micro composite magnetic fluids: Magnetic and magnetorheological evaluation for rotating seal and vibration damper

applications". *Journal of Magnetism and Magnetic Materials*, 406, 134–143. doi:10.1016/j.jmmm.2015.12.095

212. Abouobaia, E., Bhat, R., and Sedaghati, R. (2015). "Development of a new torsional vibration damper incorporating conventional centrifugal pendulum absorber and magnetorheological damper." *Journal of Intelligent Material Systems and Structures*, 27(7), 980–992. doi:10.1177/1045389x15590275

213. Christie, M. D., Sun, S., Deng, L., Ning, D. H., Du, H., Zhang, S. W., and Li, W. H. (2019). "A variable resonance magnetorheological-fluid-based pendulum tuned mass damper for seismic vibration suppression". *Mechanical Systems and Signal Processing*, vol.116, pp.530–544. doi:10.1016/j.ymssp.2018.07.007

214. Kalikate, S. M., Patil, S. R., and Sawant, S. M. (2018). "Simulation-based estimation of an automotive magnetorheological brake system performance". *Journal of Advanced Research*, vol. 14, pp. 43–51 doi:10.1016/j.jare.2018.05.011

215. Li X., Ming Z., Xiao M., Yang K., Ma Y. and Luo Y., (2019)," A wide-band piezoelectric harvester based on cantilever beam", *Ferroelectrics*, 540:1, 72-87, doi: 10.1080/00150193.2019.1611104

216. Mukhanov, A., Abdigaliyev, A., Jangeldinov, B., Zhussip, M., Zhapparov, R., Ruderman, A., and Adair, D. (2017). "Development of a Design Tool for Optimization of Voltage Generation from a Bimorph Piezoelectric Cantilever Beam". *Materials Today: Proceedings*, 4 (3), pp. 4477–4490. doi:10.1016/j.matpr.2017.04.020

217. Oliveira, F., Botto, M. A., Morais, P., and Suleman, A. (2017). "Semi-active structural vibration control of base-isolated buildings using magnetorheological dampers". *Journal of Low Frequency Noise, Vibration and Active Control*, vol. 37, Issue 3 . doi:10.1177/1461348417725959

218. Paknejad, A., Rahimi, G., Farrokhabadi, A., and Khatibi, M. M. (2016). "Analytical solution of piezoelectric energy harvester patch for various thin multilayer composite beams". *Composite Structures*, 154, 694–706. doi:10.1016/j.compstruct.2016.06.074

219. Wang, Z., Gao, H., Wang, H., & Chen, Z., (2018)."Development of stiffness-adjustable tuned mass dampers for frequency retuning". *Advances in Structural Engineering*, vol 22, Issue 2 doi:10.1177/1369433218791356

220. Kianpoor, A. and Jahani, K., (2018), "Modeling and Analyzing of Energy Harvesting from Trapezoidal Piezoelectric Beams" *Iran J Sci Technol Trans Mech Eng.*, 43, pp. 259–266 doi:/10.1007/s40997-018-0154-0

221. Rezaee, M., and Sharafkhani, N. (2017). "Electrostatically frequency tunable micro-beam-based piezoelectric fluid flow energy harvester". *Smart Materials and Structures*, 26(7), 075008. doi:10.1088/1361-665x/aa74f

222. Kim, J. E. (2017). "New efficiency measures of energy conversion and their characterization for piezoelectric vibration energy harvesters". *Journal of Intelligent Material Systems and Structures*, 28(20), 2908–2919. doi:10.1177/1045389x17704070

223. Neodymium Data Sheet, e-Magnets UK, Email: sales@e-magnetsuk.com www.e-magnetsuk.com

224. Eshaghi M, Sedaghati R and Rakheja S., (2015). "The effect of magneto-rheological fluid on vibration suppression capability of adaptive sandwich plates: Experimental and finite element analysis" *Journal of Intelligent Material Systems and Structures*, vol. 26(14) 1920–1935. doi: 10.1177/1045389X15586449
225. Kaluvan S., Park J. H, Choi S-H, Kim P. and Choi S-B, (2015) "Dynamic viscous behavior of magnetorheological fluid in coupled mode operation", *Smart Mater. Struct* 24 117001 doi:10.1088/0964-1726/24/11/117001
226. Kaluvan S., Park J. H, Lee Y.S, Han M.S and Choi S-B, (2016), " A new measurement method for operation mode dependent dynamic behavior of magnetorheological fluid" *J Mechanical Engineering Science* 0(0) 1–12, doi: 10.1177/0954406216646137
227. Zhou M., Gao W. and Yang Z. (2012). "Stiffness analysis of electromechanical transducer for nozzle flapper piezoelectric servo valve Stiffness analysis of electromechanical transducer for nozzle flapper piezoelectric servo valve" *Prazeglad Elektrotechniczny*, ISSN 0033-2097, R. 88 NR 9b/2012
228. Bansevicius R., Mazeika D., Kulvietis G., Tumasoniene I., Drukteiniene A., Jurenas V., and Bakanauskas V., (2017) ‘‘Investigation of sphere trajectories of a rotational type piezoelectric deflector’’ *Mech. Syst. Signal Process*., doi:10.1016/j.ymssp.2017.05.038
229. Hopkins, J. B., Panas, R. M., Song, Y., and White, C. D. (2017). "A High-Speed Large-Range Tip-Tilt-Piston Micromirror Array". Journal of Microelectromechanical Systems, 26(1), 196–205. doi:10.1109/jmems.2016.2628723
230. Mazeika D., Bansevicius R., Jurenas V., Bakanauskas V. and Kulvietis G. (2016), "Piezoelectric mirror with an active kinematic pair", *Journal of Vibroengineering*, vol. 18, Issue 4. ISSN 1392-8716
231. Kleiva A., and Dauksevicius R., (2019) " Experimental Study of Multi-Magnet Excitation for Enhancing Micro-Power Generation in Piezoelectric Vibration Energy Harvester" *Mechanika*. vol. 25 issue. 3, pp. 219-224, doi:10.5755/j01.mech.25.3.22968
232. Senthilkumar M., Vasundhara M. G., Kalavathi G. K., (2018), " Electromechanical analytical model of shape memory alloy based tunable cantilever beamed piezoelectric energy harvester", *Int J Mech Mater* 15: 611. doi:10.1007/s10999-018-9413-x
233. Rizzo. R, Musolino. A, Bucchi F, Forte P and Frendo F., (2015) "A multi-gap magnetorheological clutch with permanent magnet", *J. Smart Mater. Struct*. 075012 (9pp), doi:10.1088/0964-1726/24/7/075012
234. Zhiyuan W., Shouhu X., Wanquan J. and Xinglong G. (2017) " The normal stress of an electrorheological fluid in compression mode" : *RSC Adv.*, 7, 25855, doi: 10.1039/c7ra04236a
235. Brennan M. J, Day M. J and Randall R. J. (1995) “An electrorheological fluid vibration damper”, *Journal of Smart Mater. Struct*. 83 -92.

236. Kaluvan S., Shah K. and Choi S-B, (2014) "A new resonant based measurement method for squeeze mode yield stress of magnetorheological fluids" *Smart Mater. Struct*. 23 1150172014
237. Parameswaran A.P., Pai A.B., Tripathi P.K., and Gangadharan K.V., (2013) "Active Vibration Control of a Smart Cantilever Beam on General Purpose Operating System.", *Defence Science Journal*, vol. 63, nr. 4, pp. 413-417 ,

## LIST OF SCIENTIFIC PUBLICATIONS ON THE TOPIC OF THE DISSERTATION

**Publications listed in Web of Science database:**

1. Azangbebil, Hayford; Djokoto, Sylvester S. & Agelin-Chaab, Martin. (2020) Experimental and numerical studies of a soft impact piezoelectric energy harvesting using an MR fluid // IEEE Sensors Journal. eISSN 1558-1748. 2020, vol.20, issue 19 , pp**.** 11204 – 11211. doi: 10.1109/JSEN.2020.2997022 [IF: 3,076].
2. Djokoto, S.S.; Azangbebil, H.; Agelin-Chaab, M.; Dragašius, E. & Jūrėnas, V. (2020) Modeling and study of magnetorheological fluid impact base frequency enhancement for a micro-piezoelectric energy generator // International Journal of Green Energy. ISSN 1543-5075. eISSN 1543-5083. 2020, vol. 17, issue. 9, pp. 529-539. doi: 10.1080/15435075.2020.1763356 [IF: 1,302].
3. Djokoto, Sylvester S.; Dragašius, Egidijus; Jūrėnas, Vytautas & Agelin-Chaab, Martin. Controlling of vibrations in micro-cantilever beam using a layer of active electrorheological fluid damping medium // IEEE Sensors Journal. ISSN 1530-437X. eISSN 1558-1748. 2020, vol. 20, issue. 8, pp. 4072-4079. doi: 10.1109/JSEN.2019.2961380. [IF: 3,076].
4. Augustaitis, Aistis; Djokoto, Sylvester Sedem; Jūrėnas, Vytautas; & Kulvietis, Genadijus. Control features of 3D deflector under different braking conditions // MECHANIKA ISSN: 1070-9622, 24(5): pp. 746–750. doi: 10.5755/j01.mech.24.5.20316 . [IF: 0,500].

**Publications listed in conferences:**

1. S. S Djokoto; E. Dragašius ; V. Jūrėnas & A. Mystkowski. Controlling the Positioning 3D Rotational Piezoelectric Deflector using ERF: an Experimental Study //15th International Conference Mechatronic Systems and Materials 1-3 July 2020, Bialystok, Poland
2. Djokoto, S.S.; Dragašius, E.; Jūrėnas, V. & Agelin-Chaab, M. Micro-piezoelectric actuator vibration control using electrorheological fluid active damping medium: experimental study //13th IFAC workshop on intelligent manufacturing systems IMS 2019, Oshawa, Canada, 12–14 August 2019 Elsevier. ISSN 2405-8963. 2019, vol. 52, issue. 10, p. 388-393.
3. Azangbebil, Hayford; Djokoto, Sylvester Sedem; Agelin-Chaab, Martin & Dragašius, Egidijus. A study of nonlinear piezoelectric energy harvester with variable damping using thin film MR fluid // 13th IFAC workshop on intelligent manufacturing systems IMS 2019, Oshawa, Canada, 12–14 August 2019 Elsevier. ISSN 2405-8963. 2019, vol. 52, issue. 10, p. 394-399.
4. Djokoto, Sylvester Sedem; Azangbebil, Hayford; Agelin-Chaab, Martin; Dragašius, Egidijus & Jūrėnas, Vytautas. Design and modeling of MRF impact base frequency enhancement for a piezoelectric energy generator //

Joint congress of the Canadian Society for Mechanical Engineering and CFD Society of Canada: proceedings, June 2-5, 2019, Western University, London, Ontario, Canada. p. [139-146].
5. Djokoto, Sylvester Sedem; Agelin-Chaab, Martin; Jūrėnas, Vytautas & Dragašius, Egidijus. Experimental investigation of squeezed MRF film stopper and Its effect on vibrating bimorph for frequency tuning of an energy generator // 2019 IEEE SoutheastCon, Huntsville, AL, USA, 11-14 April 2019. ISBN 9781728101385. eISBN 9781728101378. p. 1-7.
6. Augustaitis, Aistis; Kulvietis, Genadijus; Jurėnas, Vytautas; Djokoto, Sylvester Sedem. Kinematic characteristics of hollow ball under different braking conditions // Vibroengineering procedia : [29th International conference on vibroengineering, Vilnius, Lithuania, December 1st 2017]. Kaunas: ISSN 2345-0533. 2017, vol. 15, p. 7-12.
7. Djokoto, Sylvester Sedem; Jūrėnas, Vytautas; Bansevičius, Ramutis Petras, & Dragašius, Egidijus. Investigation of piezoelectric cantilever dynamics with ERF non-linear contact // Mechanika : proceedings of the 22nd international scientific conference, 19 May 2017, p. 97-101.
8. Krishnamoorthy, Shanker Ganesh; Skiedraitė, Inga; Djokoto, Sylvester Sedem, & Dragašius, Egidijus; Skvireckas, Ramūnas. Study of change in resonance characteristics for a passive bimorph damper // WSEAS Transactions on Applied and Theoretical mechanics. ISSN 1991-8747. eISSN 2224-3429. 2017, Vol. 12, p. 51-56.

## ANNEXES

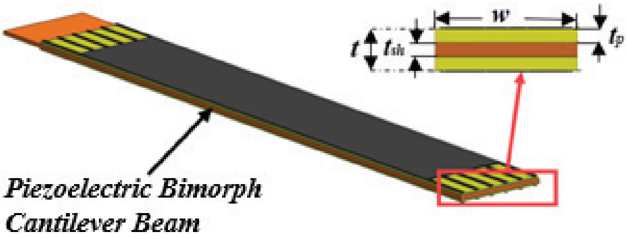


**Annexe 1.** Schematic of the piezoelectric bimorph cantilever beam

**Annexe 2.** Characteristic values of piezoelectric bimorph cantilever beam

| Symbol | Description | Value | Units |
|---|---|---|---|
| $L$ | The total length of the beam | 50 | **mm** |
| $w$ | The width of the beam | 7.2 | **mm** |
| $t$ | Total beam thickness | 0.78 | **mm** |
| $t_p$ | The thickness of piezoelectric layer | 0.26 | **mm** |
| $t_{sh}$ | Shim layer thickness | 0.28 | **mm** |
| $\rho_p$ | Piezoelectric layer density | 8100 | $\mathbf{Kg/m^3}$ |
| $\rho_{sh}$ | Shim layer density | 8960 | $\mathbf{Kg/m^3}$ |
| $\varepsilon_{33}$ | Permittivity | 39825e-12 | $\mathbf{nF/m}$ |
| $E_{sh}$ | Shim layer modulus of elasticity | 120e9 | $\mathbf{N/m^2}$ |
| $E_p$ | Piezoelectric layer modulus of elasticity | 6.7e10 | $\mathbf{N/m^2}$ |
| $e_{31}$ | Piezoelectric constant | 250 | |
| $C_p$ | Capacitance | 45 | **nF** |
| $Q_m$ | Mechanical quality factor | 50 | |
| $k_{33}$ | Piezoelectric coupling coefficient | 0.71 | |
| $S_{11}^E$ | **Piezoelectric compliance** | **14.90e-12** | $\mathbf{m^2/N}$ |

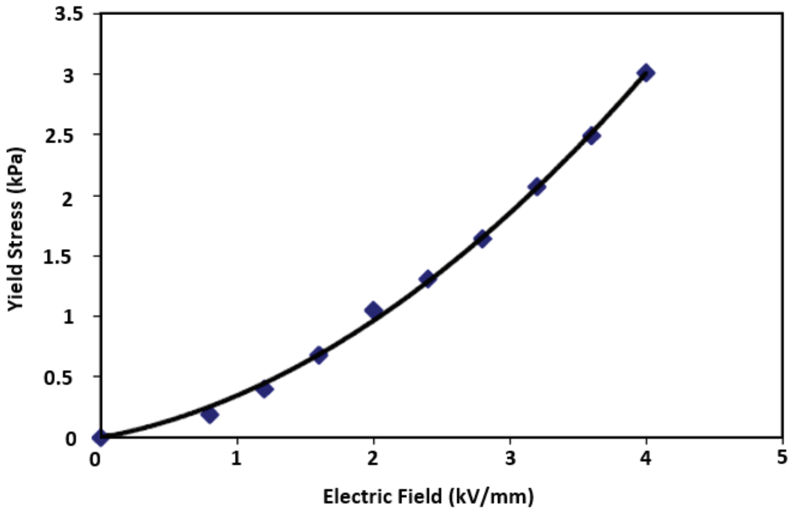


**Annexe 3.** Relationship between the yield stress and the electric field of applied ERF [193]

**Annexe 4.** Specifications of ERF [193]

| Property | Value |
|---|---|
| **Base Fluid** | silicone-based |
| **Density ($\rho_{ERF}$)** | 1.3e3 (kg/m$^3$) |
| **Viscosity ($\mu$) at 30 °C** | 0.11 Pa. s |
| **Flashpoint** | >150 (°C) |
| **Boiling Point** | > 200 (°C) |
| **Freezing Point** | < -20 (°C) |

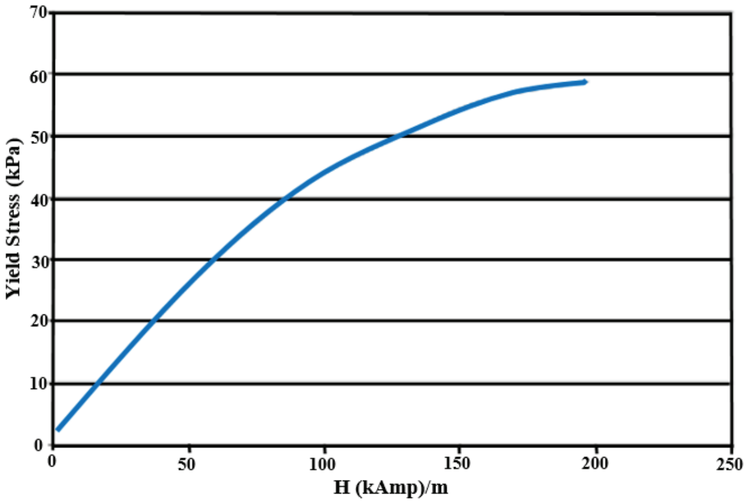


**Annexe 5.** Yield stress-magnet field relationship of MRF-140CG [201]

**Annexe 6.** Physical properties of fluid MRF 140CG Lord Corporation [201]

| **Property** | **Value** |
|---|---|
| Base Fluid | Oil hydrocarbon |
| Working temperature | -40 to 130 (°C) |
| Density | 3540 $(\mathrm{Kg/m^3})$ |
| Colour | Dark grey |
| Viscosity (slope between 800 and 500 Hz at 40 °C) | 0.280 (± 0.070) $(\mathrm{Pa.s})$ |
| Flashpoint | >150 (°C) |
| Weight percentage of particles | 85.44 % |
| Thermal conductivity at 25 (°C) | 0.25–1.06 $(\mathrm{W.m^{-1}.K^{-1}})$ |

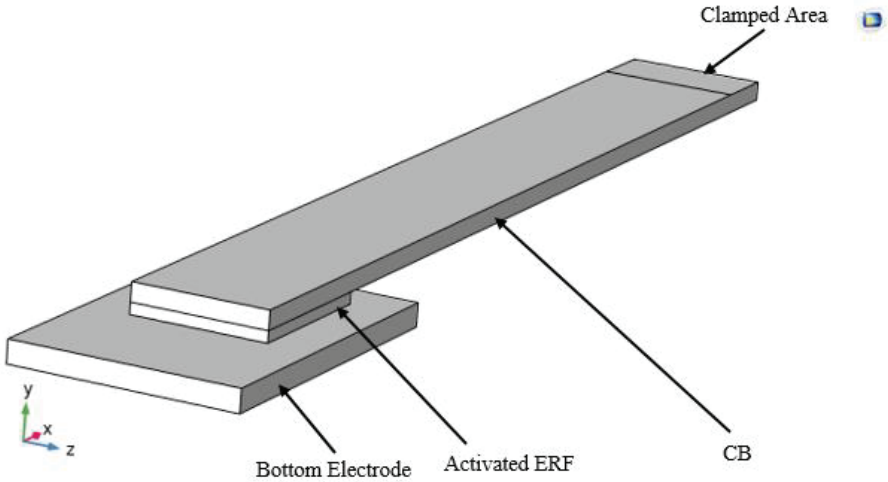


**Annexe 7.** 3D model of CB-ERF damping medium in COMSOL

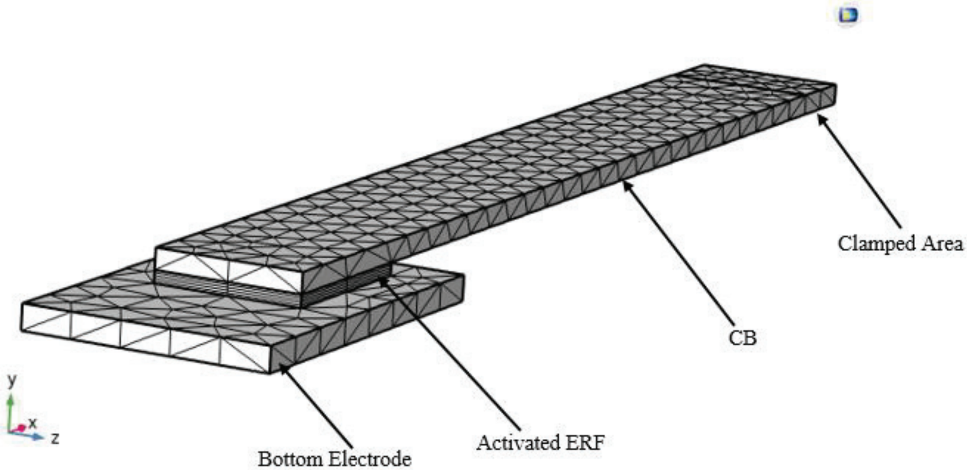


**Annexe 8.** Meshing of CB and ERF damping medium in COMSOL

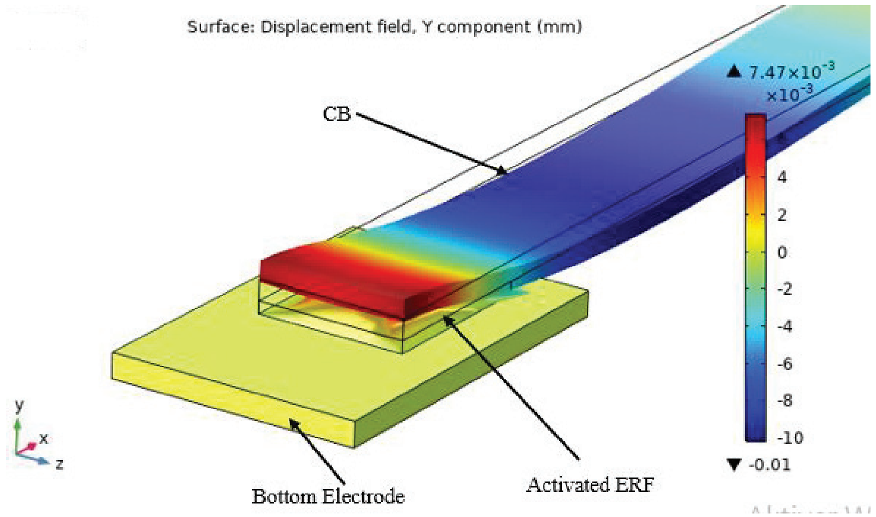


**Annexe 9.** Simulation of upward displacement field CB with ERF damping medium

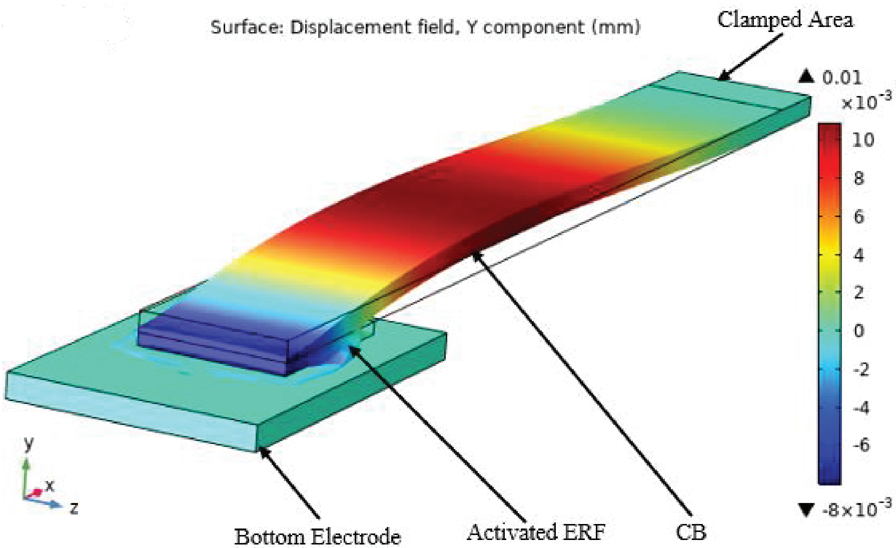


**Annexe 10.** Simulation of downward displacement field CB with ERF damping medium

**Annexe 11.** Matlab coding for energy generator

```
%% Thesis-Design of MRF Piezoelectric Energy Generator
% Sylvester Djokoto

function nonlinear function
%global R
Fs=200000;
Ns=1024;
```

```
Ts=1/Fs;
Tmax=0.1;
tspan=0:Ts:0.2;

kk=length(tspan);
k=0:kk-1;
T=kk/Fs;
R=200000;

v0=[0 0.3];
zz=length(v0);
delta = [ 0 1];
nn=length(delta);
V1=zeros(length(tspan),nn);
displacement1=zeros(kk,nn);
velocity1=zeros(kk,nn);
state_values1=zeros(kk,3,nn);
V2=zeros(length(tspan),nn);
displacement2=zeros(kk,nn);
velocity2=zeros(kk,nn);
state_values2=zeros(kk,3,nn);
time1=zeros(2000,1);
time2=zeros(2000,1);

delta=[0 1];
 IC1=[0 0.18 -3.5];
%for ii=1:nn
%  y0=0;
%  v0=1;
%  V0=0;
 %  %v0=1;

 tspan1=0:Ts:0.006;
 options = odeset('Events',@eventfunct2);
%     IC=[y0 v0 V0];     %% initial condition
%call ode45loolo
 [time1,state_values1]=ode45(@(t,x)nonlinear_func2(t,x,delta(1),R),tspan1,IC1);
 %yy1=interp1(time1,state_values1(:,3),tspan);
 IC2=[0 0.18 0];
 tspan2=0.006:Ts:0.03;
 %call ode45
 [time2,state_values2]=ode45(@(t,x)nonlinear_func2(t,x,delta(2),R),tspan2,IC2);
 %yy2=interp1(time2,state_values2(:,3),tspan);
```

```
%    t1=time1;
%    t2=time2;
displacement1=state_values1(:,1);                                % displacement
vector
 velocity1=state_values1(:,2);                                   %velocity vector
 V1=state_values1(:,3);                                        %% generated voltage vector
%Vcat=[V1;yy1'];
%aa=length(V);

displacement2=state_values2(:,1);                          % displacement vector
velocity2=state_values2(:,2);                              %velocity vector
V2=state_values2(:,3);                                     %% generated voltage vector
%Vcat=[V1;yy1'];
%aa=length(V);
%Tcat=[time;time];
%bb=length(yy);
%[xx,fval]=fminsearch(@nonlinear_func2(V))
%freq=(sqrt((((4*pi*Tau1*rm^3)/(3*(h+max(displacement))^2))+k1)/m))/(2*pi)
%Power=10^3*(V.^2/(2*R));
%P=max(Power);
%Write data to text file
% Z=[t displacement Power V];
% fileid=fopen('test2012T.txt','w');
% %fprintf(fileid,'%s %s %s %s\n','time','displacement','Power','voltage');
% fprintf(fileid,'%f %f %f %f\n',Z');
% fclose(fileid);
%%fft
% N=length(V);                                              %length of signal
% nfft2=2^nextpow2(N);                                     %next power of two
% ff=fft(V,nfft2);
% Vy=2*ff(1:nfft2/2);
% Vy=Vy/max(Vy);
% VV=abs(Vy);
% Vx=Fs*(0:nfft2/2-1)/nfft2;                               %frequency of signal in Hz
% vv=Vx';
% vvv=VV;
Displacement=[displacement1;displacement2];
V=[V1;V2];
length(V);
Vcat1=V(1:3001,:);
Vcat2=V(2140:end,:);
 vvcat=sort(Vcat1);
VV=smooth([Vcat1;Vcat1],200);
xnorm=findchangepts(VV)
```

```
vg=[VV(1:1861,:); VV(3193:end,:)];
Tg=linspace(0,0.03,4671);
length(vg);
Vg=smooth(vg,100);
Time=[time1;time2];
 s=max(displacement1);
 s1=max(V1);
 Vp2p=max(Vg)-min(Vg)
 Pp=(Vp2p)^2/(4*R)
 Displacement=detrend(Displacement);
 [Y,freq]=positiveFFT(Displacement,Fs);
 Y_abs=abs(Y);
 F_freq=freq;
 Ac=sqrt(Y_abs.*F_freq);
 ZZ=[Vg];
 fileiD=fopen('volt012T.txt','w');
 fprintf(fileiD,' %s\n','voltage');
 fprintf(fileiD,' %f\n',ZZ');
 fclose(fileiD);

%plot(R,Power)
%Power=((s1^2)/(2*R))                                    %power in one sided
spectrum
% X1=(fft(y,Ns))/Ns;
% Displacement=2*abs(X1(1:Ns/2+1));
%  figure (1);
% plot(f,Displacement)
%  xlabel('Frequency [Hz]')
%  ylabel('Displacement [meters]')
% % legend('Displacement Response at field density of 0.3T')
% grid on

%%Plotting
%
%       clf;
%       figure (1)
%       plot(Time,V,'r','linewidth',4);
%       xlabel('Time [s]')
%       ylabel('Voltage [V]')
%       %title('Generated Voltage Vs Time')
%       set(gca,'fontsize',32)
%       legend('@0.12T')
%       ax = gca;
%       ax.GridColor = [0 .35 .35];
```

```
%       ax.GridLineStyle = '-';
%       ax.GridAlpha = 0.30;
%
%       ax.MinorGridColor = [0 .30 .30];
%       ax.MinorGridLineStyle = '-';
%       ax.MinorGridAlpha = 0.25;
%       grid(gca,'minor')
%       grid on
    %set(gcf,'Colour','k')
    %set(gca,'Box','off')
    %    figure (2)
    %    plot(freq,2*Y_abs,'linewidth',2)
    %    %axis([0 500 0 0.25])
    %    xlabel('Frequency (Hz)')
    %    ylabel('Amplitude (a.u)')
%       figure (3)
%       clf
%       plot(Time,10^6*Displacement,'k','linewidth',4);
%       xlabel('Time [s]')
%       ylabel('Displacement [\mum]')
%       %title('Displacement Vs Time')
%       set(gca,'fontsize',32)
%       ax = gca;
%       ax.GridColor = [0 .35 .35];
%       ax.GridLineStyle = '-';
%       ax.GridAlpha = 0.30;
%
%       ax.MinorGridColor = [0 .30 .30];
%       ax.MinorGridLineStyle = '-';
%       ax.MinorGridAlpha = 0.25;
%       grid(gca,'minor')
%       grid on
%       legend('@0.12T')
%       figure (4)
%       plot(F_freq,Y_abs)
    %    figure (3)
    %    clf;
    %    plot(time,velocity,'b','linewidth',2)
    %    xlabel('Time [s]')
    %    ylabel('Velocity [m/s]')
    %    title('Velocity-time plot')
    %    set(gca,'fontsize',12)
    %   figure (4)
    %    clf;
```

```
    %    plot(time,Power,'g','linewidth',2)
    %    xlabel('time [s]')
    %    ylabel('Power [w]')
    %    title('Power-time plot')
    %    set(gca,'fontsize',12)
    %    figure (5)
    %    plot(f,V_abs)
    %    figure (5)
    %    clf
    %    plot(time,yy,'linewidth',2)
    %    xlabel('Displacement (m)')
    %    ylabel('Velocity (m/s)')
    %    title('Phase Portrait plot')
    %    set(gca,'fontsize',12)
      figure (6)
      plot(Tg,Vg,'r','linewidth',4)
      xlabel('Time [s]')
    ylabel('Voltage [V]')
    %title('Generated Voltage Vs Time')
    set(gca,'fontsize',32)
    legend('@0.04T')
    ax = gca;
    ax.GridColor = [0 .35 .35];
    ax.GridLineStyle = '-';
    ax.GridAlpha = 0.30;

    ax.MinorGridColor = [0 .30 .30];
    ax.MinorGridLineStyle = '-';
    ax.MinorGridAlpha = 0.25;
    grid(gca,'minor')
    grid on

    figure (7)
    plot(F_freq,Y_abs)

%          figure (7)
%
%          plot(Time,VV)
%        data=table(Time, Displacement, V);
%        writetable(data,'paperdata.txt')
  end
```

```
function xdot=nonlinear_func2(t,x,delta,R)
%for  R=10000:1000:20000;


%delta=[0 1];
xdot=zeros(1,3);
w=20;
pm=7500;
r=2e-3;
rm=2e-3;        %Radius of magnet [m]
hc=6e-3;       %height of magnet
%for R=20000:10:500000
xdot(1)=x(2);       %
mt=0*pi*r^2*hc*pm;
tp=0.26e-3;
lb=38e-3;
b=7.2e-3;
mc=0.0018;          %calculated mass of the cantilever beam
m=mt+33/140*mc;  %effective masss of the beam

Tau1=67246;           %yield stress of the fluid in N/m^2 1244@0.03T 1668@0.4T
@0.12=5265 6679@0.15T 2531@0.06T 3415@0.08T 4320@0.1T,14671@0.3T,
27806@0.5T
h=0.5e-3;          %Initial gap between cantilever beam and magnet in meters
eta=0.288;            %viscosity of the fluiding Pa.s
k1=1132;            %calculated stiffness of the beam
zeta=0.02;       %damping ratio of the cantilever beam
%alpha=0.00440;      %electromnechanical coupling coefficient [N/V]         %
Load resistance in ohms
%C=37*10^-9;      % Capacitance of the piezo ceramic in Farad
k2=(4*pi*rm^3*Tau1)/(3*(h+max(x(1)))^2)
c2=(3*pi*eta*rm^4)/(2*(h+min(x(1)))^3);
d31=-315e-12;     %d31 coefficient
%d33=640e-12;     %d33 coefficient
s11=14.2e-12;    %% Piezoelectric compliance
phi=0.42;                                          %%d33 coupling coefficient
%s11D=s11*(1-phi^2);
z33t=4500;                          %%relative permittivity constant at constant
stress
zeta33=z33t*8.85*10^-12;
z33s=zeta33-(d31^2)/s11;                    %%permittivity constant at constant
strain
Cp=(z33s*lb*b)/tp;
```

```
alpha=sqrt(0.5*(phi^2*Cp*(k1+k2)));
c1=2*zeta*sqrt(m*k1);
wr=sqrt((k1+k2)/m);
ww=max(wr);
%           Fr=ww./(2*pi);
%           Rs=1/(wr*2*Cp);
%           Ropt=(2*zeta)/(ww*Cp*(sqrt(4*zeta^2+phi^4)));
zeta_e=(ww*phi^2)/(sqrt(ww^2+1/(2*R*Cp)^2));
C_const=c1+c2;
z_ratio=C_const/(2*m*ww);
ZETA=zeta_e+z_ratio;
g=9.81;
gg=2e-5;
A=g;
%           if t<=0.03
%              delta=0;
%           else
% delta=1;
%% prescribed displacement amplitude m
%    xdot(2)=sin(2*pi*w*t)-(2*alpha*x(3))/m-((c1+c2)*x(2))/m-
((k1+k2)*x(1))/m;
%    xdot(3)=(alpha*x(2)-x(3)/(2*R))*1/(C);
%    xdot=xdot';
%x(1)=h;
xdot(2)=(0.45*g*sin(2*w*pi*t))-(2*alpha*x(3))/m-delta*(c1*x(2))/m-
(c2*x(2))/m-(k1*x(1))/m-delta*(k2*x(1))/m;
xdot(3)=(alpha*x(2)-x(3)/(2*R))*1/(Cp);
xdot=xdot';
heaviside(x(1)-h);
%% iteration


end
%heaviside(x(1)-h);

% function y = delta3(x)
%
% if x >= 5e-4
%    y  =1;
% else
%    y =0;
%
% end
```

SL344. 2021-08-17, 17,25 leidyb. apsk. l. Tiražas 10 egz. Užsakymas 219.
Išleido Kauno technologijos universitetas, K. Donelaičio g. 73, 44249 Kaunas
Spausdino leidyklos „Technologija“ spaustuvė, Studentų g. 54, 51424 Kaunas